NEW FRONTIERS IN CHEMISTRY
New Front. Chem.

(*former Annals of West University of Timişoara – Series of Chemistry*)

(2014) Volume 23, Number (Issue) 1, pp. 1-77

Ordinary Issue

TABLE OF CONTENTS

PUBLISHER:
Universitatea de Vest din Timişoara

NEW FRONTIERS IN CHEMISTRY: METADATA

New Frontiers in Chemistry (New Front. Chem.) is an open-access fee-free peer-review international academic journal addressing the modern trends and frontiers in fundamental, applicative and multidisciplinary chemistry, paralleling the ever-expanding chemical data, methods, and compounds available and continuously produced, towards cross fertilizing the multidisciplinary ideas as coming from Chemistry combined with Mathematics, the Natural and Applied sciences (Physics, Biology, Medicine, Agriculture, Environmental, Engineering), and beyond.

NEW FRONTIERS IN CHEMISTRY
(NEW FRONT. CHEM.)
is published biannually by

West University of Timișoara
Blvd. V. Parvan 4
Timisoara 300223, ROMANIA
E-mail: newfrontchem@iqstorm.ro
Web: www.newfrontchem.iqstorm.ro

ISSN 2393 – 2171
ISSN-L 2393 – 2171

Subscription Price per Volume
Electronic: open access Print: on demand by above email address

Additional color graphics is available in the e-version of this Journal

NEW FRONTIERS IN CHEMISTRY: EDITORS

Editorial Board:

NEW FRONT. CHEM. (**2014**)
Volume 23, Number 1, pp. 1-9
ISSN 2393-2171; ISSN-L 2393-2171

Former: Ann. West Univ. Timisoara – Series Chem.
ISSN: 1224-9513

Article

TREATMENT OF DYES CONTAINING WASTE WATER WITH NANOCRYSTALLINE ZINC FERRITE

Raluca Voda, Adina Negrea(♣), Lavinia Lupa, Mihaela Ciopec, Petru Negrea, Corneliu Mircea Davidescu
University Politehnica Timisoara, Faculty for Industrial Chemistry and Environmental Engineering, Bv. Parvan no. 6, Timisoara, RO-300223, Romania

ABSTRACT

Treatment of colored water before discharged is an important issue in order to avoid certain hazards and environmental problems. In contrast with the conventional methods of dyes removal the adsorption techniques is the most versatile and widely used, in special when the adsorbent could easily be removed through magnetic separation. Therefore in order to accomplish these conditions in the present paper was obtained zinc ferrite to be used as adsorbent in the treatment process of waste waters containing dyes. The nanocrystalline zinc ferrite was obtained after a heating treatment of the zinc ferrioxalate coordination compound, as precursor, at 500^{o}C. The obtained zinc ferrite was investigated by IR spectroscopy, X-ray diffraction and SEM microscopy.

Keywords: zinc ferrite, dye, adsorption.

1. INTRODUCTION

The release of colored water in the effluents, besides the pollution with heavy metals, poses certain hazards and environmental problems. Dyes have long been used in dyeing, paper and pulp, textiles, plastics, leather, cosmetics and food industries.

These colored compounds are not only aesthetically displeasing but also persist for long distances in flowing water, retards photosynthesis, inhibit growth of aquatic bi ota by blocking out sunlight and utilizing dissolved oxygen [1-6].

There are various conventional methods of removing dyes including coagulation and flocculation, oxidation or ozonation and membrane separation [7-15]. However, these methods are not widely used due to their high cost and economic disadvantage. Chemical and

♣ Correspondent author: Tel:0256-404192, Fax:0256-403063, E-mail: adina.negrea@upt.ro

electrochemical oxidations, coagulation are generally not feasible on large scale industries. In contrast, an adsorption technique is by far the most versatile and widely used. [1, 7, 9, 15-18] Several adsorbents have been investigated by the previous researchers such as: activated carbon, alumina, silica, natural materials and synthetic resin [15, 19-23]. The most adequate adsorbent has to accomplish the following requirements: to be a low cost adsorbent to be easy regenerated and disposed. Furthermore in the last years an important accent was out on the separation and regeneration of the adsorbent from heterogeneous systems. In this way a lot of separation technique such as free settling, centrifugation, and membrane filtration has been studied. Unfortunately, these separation techniques suffer from prolong usage of equipment operation, complicated technical requirements as well as high operational costs and thus severely restrict water treatment applications. Being an efficient and economical method, magnetic separation would be an ideal alternative than centrifugation or filtration methods [1]. Therefore the use of various types of magnetic nanoparticles has been reported for the removal of different pollutants from environmental samples [1, 9, 16, 17, 24-26]. In this paper the nanocrystalline zinc ferrite was used as adsorbent material for the treatment of waste waters resulted from the remanufacturing of the empty ink cartridges. The zinc ferrite was obtained by thermal decomposition of zinc ferrioxalate coordination compound, as precursor, this method had been widely used for synthesis of nanoferrites [27, 28].

2. MATERIALS AND METHODS

All the reagents used for the synthesis of ferrite were analytical grade, including ferric (III) nitrate ($Fe(NO_3)_3 \cdot 9H_2O$, Mw = 403.95 $gmol^{-1}$, Merk), zinc nitrate ($Zn(NO_3)_2 \cdot 6H_2O$, Mw = 297.49 $gmol^{-1}$, Merk), 1,2-ethanediol ($C_2H_4(OH)_2$, Mw = 62.07 $gmol^{-1}$, Merk) and 2M nitric acid solution (Merk). An aqueous solution containing ethanediol, iron nitrate, zinc nitrate and nitric acid (2M) in a molar ratio x : 2 : 1 : y where $x \geq 3$ and $y \geq 2$ is heated in a water bath. The reaction is completed when no more gas evolving is observed. The obtained solid reaction product, purified by refluxing with an adequate acetone-water mixture, is filtered, washed with acetone and maintained in air until constant mass. The coordination compound $[Fe_2Zn(C_2O_4)_4(OH_2)_6]$ precursor is synthesized using 2M nitric acid solution. The oxide $ZnFe_2O_4$ is obtained after heating treatment of the precursor at 500^oC for one hour, with a heating rate of 5^oC/min.

The FTIR spectrum (KBr pellets) of the ferrite was recorded on a Vertex 70 BRUKER-FTIR spectrophotometer in the range 400-4000 cm^{-1}. The oxide was characterized by X-Ray diffraction (XRD) analysis. The powder X-Ray diffraction patterns of the obtained oxides was recorded at room temperature with a XRD using a Rigaku Ultima IV diffractometer, using Cu K_α radiation (λ = 1.5418 Å). SEM image was recorded using a Quanta FEG 250 microscope, equipped with an EDAX ZAF quantifier.

The obtained zinc ferrite was used as adsorbent material in the treatment of waste waters resulted from ink jet manufacturing. The residual solution containing dyes was obtained from a local manufactory were the empty ink-jet cartridges are refilled. The analyze of the dye concentration from the solution before and after adorption process was realized spectrophotometricaly using a Varian Cary 50 spectrophotometer. The spectra were recorded in the range of 300-800 nm. In the first step the influence of the adsorbent quantity upon the degree of adsorption was determined. In this way 25 mL of residual waters was treated with various quantities of adsorbent materials (0.02, 0.03, 0.04, 0.05, 0.06 and 0.07 g). The samples were shacked from 1 hour using a Julabo SW23 shaker, and after were filtrated and

the resulted solutions were again analyzed through UV-VIS spectrophotometry. After establishing the optimum S: L ratio the influence of the shaking time (15, 30, 45, 60, 90 and 120 min) upon the adsorption capacity was determined. The degree of adsorption was determined based on the following equation:

$$\eta = \frac{(Ads_{init} - Ads_{fin})}{Ads_{init}} 100 \quad (1)$$

where:

η represents the removal degree of dye, %;

Ads_{init} represents the initial absorbance of the dye present in the waste water;

Ads_{fin} represents the absorbance of the dye present in the waste water after treatment with the zinc ferrite.

3. Results and Discussions

The synthesis reaction of the zinc ferrioxalate is based on the redox reaction between 1,2-ethanediol and nitrate ion [27]:

$$12C_2H_4(OH)_2 + 6([Fe(OH_2)_6]^{3+} + 3NO_3^-) + 3([Zn(OH_2)_6]^{2+} + 2NO_3^-) + 8(H^+ + NO_3^-) \xrightarrow{\Delta t^\circ}$$

$$\xrightarrow{\Delta t^\circ} 3Fe_2Zn(C_2O_4)_4 \cdot 6H_2O_{(s)} + 32NO_{(g)} + 76H_2O_{(g)}$$

The FTIR spectrum (Figure 1) of the conversion product obtained after the calcination at 500 °C for 1h of the coordination compound shows only the bands characteristic for $ZnFe_2O_4$ ferrite (550cm-1 and 418 cm-1) being in agreement with the literature data [29, 30].

Figure 1: FTIR spectrum of zinc ferrite

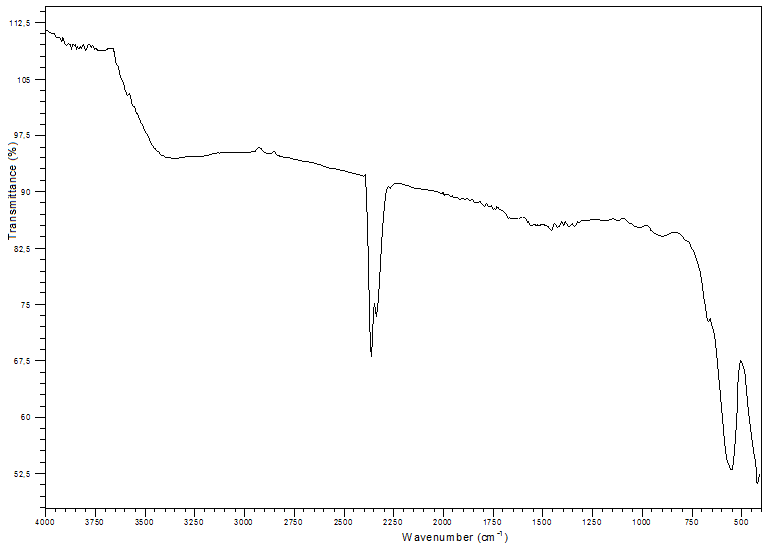

In Figure 2 is presented the XRD pattern of $ZnFe_2O_4$ ferrite. The XRD pattern shows the presence of well crystallized pure zinc ferrite was identified in using JCPDS 04-006-8036 (8.460Å). The average crystallites size was evaluated using Scherrer's formula [31]:

$$d_{XRD} = [0.91\lambda/(\beta\cos\theta)] \times 57.32 \quad (2)$$

where d_{XRD} is the crystallite size, λ the wave length (Cu K_α), β the corrected half-width obtained using α quartz as reference and the Waren formula and θ is the diffraction angle of the most intense diffraction peak.

Figure 2: The XRD of $ZnFe_2O_4$ derived from $[Fe_2Zn(C_2O_4)_4(OH_2)_6]$ compound obtained by an independent pyrolysis at 500°C

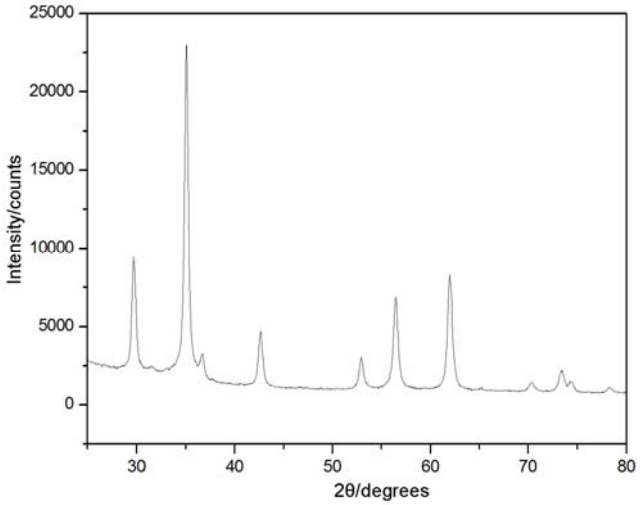

The mean crystallite size evaluated using Scherrer's formula is 22 nm and the lattice parameter from XRD analysis is 8.453Å.

The SEM image (Figure. 3) shows that the ferrite consists of agglomerated spherical particles with 20-40nm average particle size and microporous structure.

Figure 3: SEM image of $ZnFe_2O_4$ powder prepared from $Fe_2Zn(C_2O_4)_4(OH_2)_6$ compound thermally treated at 500°C

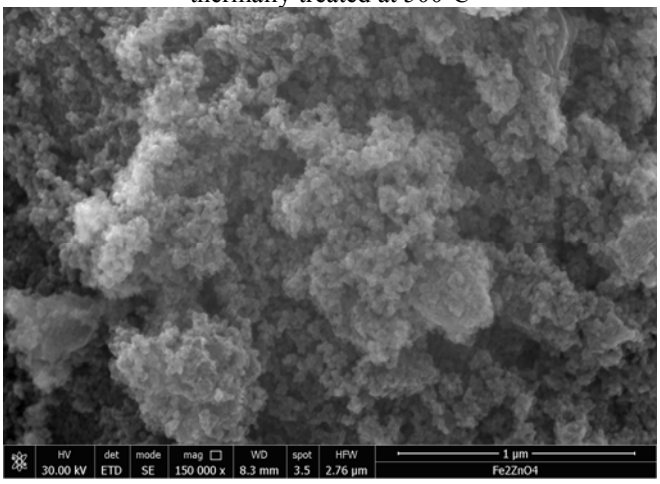

The EDX spectrum of $ZnFe_2O_4$ is presented in Figure 4. Qualitative and quantitative EDX analyzes showed a high purity and corresponding stoichiometry of the zinc ferrite analyzed.

Figure 4: EDX spectrum of $ZnFe_2O_4$ powder prepared from $Fe_2Zn(C_2O_4)_4(OH_2)_6$ compound thermally treated at 500°C

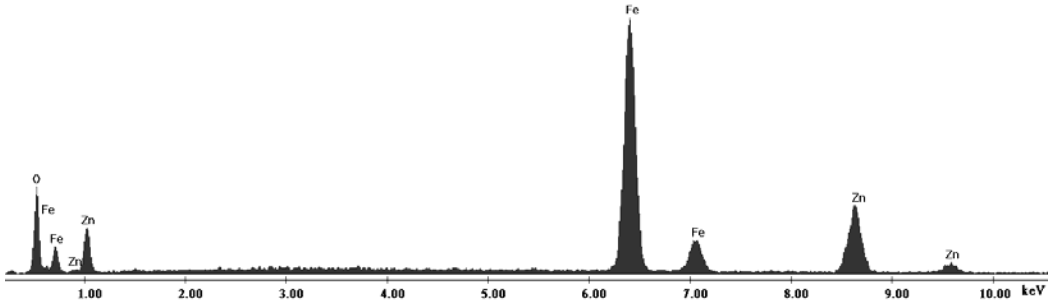

The UV-VIS spectrum of 300-800 nm of the waste waters treated with the studied adsorbent is presented in Figure 5.

Figure 5: UV-VIS spectrum of the used waste water

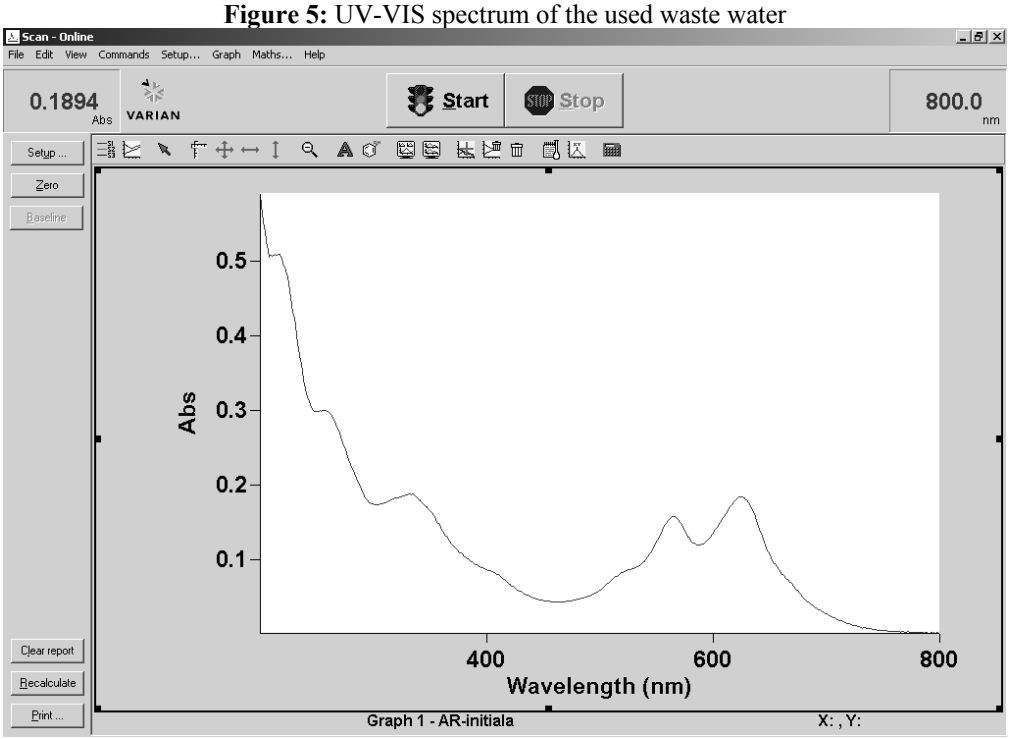

In the spectrum presented in Figure 5 can be observed three peaks at three wavelength (625, 564 and 333 nm) specific for the three colors present in the waste waters.

The influence of the S:L ratio upon the efficiency of the adsorption process of the three colors present in the waste waters onto the studied zinc ferrite is presented in Figure 6.

Figure 6: The influence of the S:L ration upon the adsorption process efficiency

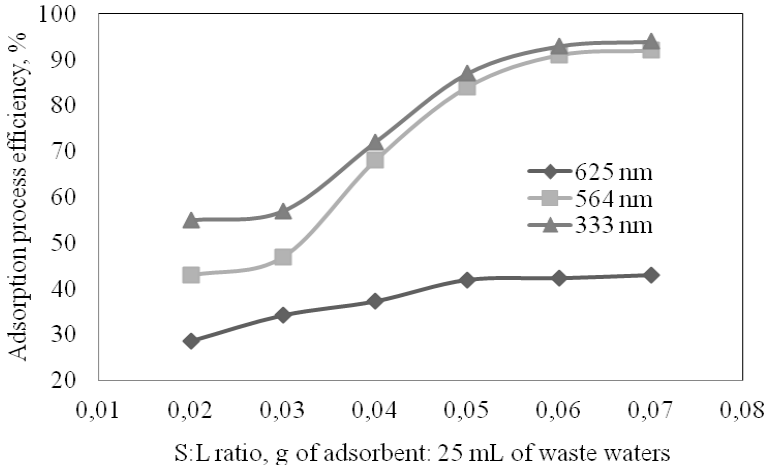

From the experimental data can be observed that for the all colors present in the studied waste waters the use of a higher quantity of zinc ferrite lead to a higher degree of separation of dyes from aqueous solution. This influence is not significant for a S:L ratio higher than 0.05 g of zinc ferrite in 25 mL of waste waters. Therefore the further studies will be conducted at this S:L ratio

The influence of the stirring time upon the efficiency of the adsorption process of dyes onto the studied zinc ferrite is presented in Figure 7.

Figure 7: The influence of the stirring time upon the adsorption process efficiency

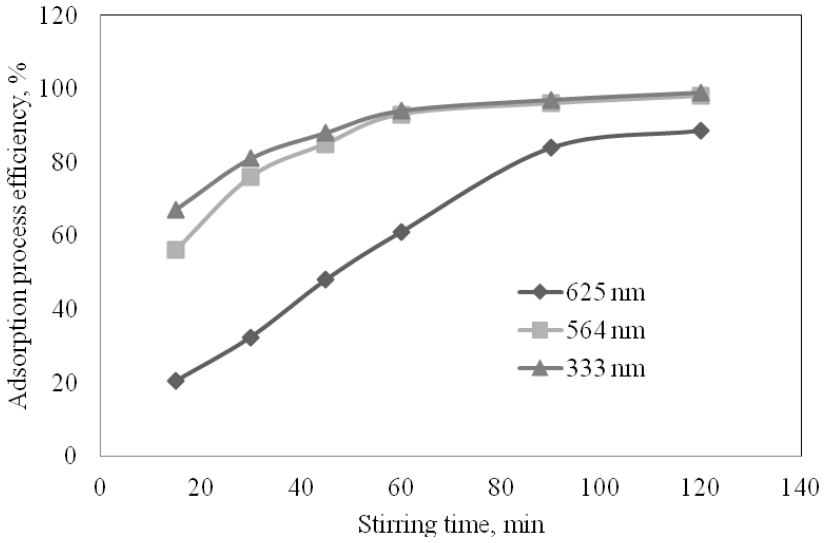

It can be observed that for the removal of dyes which absorb at 564 nm and 333 nm a stirring time of 60 minutes is sufficient for obtaining an adsorption degree higher than 90%. But to remove all the colors present in the waste waters and realize 100% treatment efficiency is necessary to treat the waste waters with the studied adsorbent for 120 minutes.

4. CONCLUSION

Nanocrystalline zinc ferrite, with pure spinelic phase $ZnFe_2O_4$, was obtained after the calcination zinc ferrioxalate coordination compound at 500˚C. The FT-IR spectrum showed two characteristic metal oxygen vibrational bands. The average particle size of ferrite was in the range of 20-40 nm, as revealed by XRD and SEM techniques.

The obtained nanocrystalline zinc ferrite presented good efficiency in the removal process of dyes from a real waste water. The highest degree of separation of the dyes from the waste water resulted from the ink-jet cartridges remanufacturing is obtained when is used a S:L ratio of 0.05 adsorbent in 25 mL of waters for 2 hour of shaking.

ACKNOWLEDGEMENT

„This work was partially supported by the strategic grant POSDRU/159/1.5/S/137070 (2014) of the Ministry of National Education, Romania, co-financed by the European Social Fund – Investing in People, within the Sectoral Operational Programme Human Resources Development 2007-2013."

REFERENCES

1. Wang L., Li J., Wang Y., Zhao L., Jiang Q., Adsorption capability for Congo red on nanocrystalline MFe_2O_4 (M = Mn, Fe, Co, Ni) spinel ferrites, *Chem. Eng. J.,* **2012**, 181-182, 72-79.
2. Louhichi B., Bensalah N., Comparative study of the treatment of printing ink wastewater by conductive-diamond electrochemical oxidation, Fenton process, and ozonation, *Sustain. Environ. Res.*, **2014**, 24(1), 49-58.
3. Zhang G.J., Liu Z.Z., Song L.F., Hu J.Y., Ong S.L., Ng W.J., Post-treatment of banknote printing works wastewater ultrafiltration concentrate, *Water. Res.*, **2004**, 38(16), 3587-3595.
4. Saint Amand F.J., Hydrodynamics of deinking flotation, *Int. J. Miner. Process.*, **1999**, 56(1-4), 277-316.
5. Viesturs U., Leite M., Eisimonte M., Eremeeva T., Treimanis A., Biological deinking technology for the recycling of office waste papers, *Bioresource Technol.*, **1999**, 67(3), 255-265.
6. Ma X.J., H.L. Xia, Treatment of water-based printing ink wastewater by Fenton process combined with coagulation, *J. Hazard. Mater.*, **2009**, 162(1), 386-390.

7. Iram M., Guo C., Guan Y., Ishfaq A., Liu H., Adsorption and magnetic removal of neutral red dye from aqueous solution using Fe_3O_4 hollow nanospheres, *J. Hazard. Mater.*, **2010**, 181, 1039-1050.
8. Wu J. S., Liu C. H., Chu K.H., Suen S.Y., Removal of cationic dye methyl violet 2B from water by cation exchange membranes, *J. Membr. Sci.* 2008, 309, 239-245.
9. Vîrlan C., Ciocârlan R.G., Roman T., Gherca D., Cornei N., Pui A., Studies on adsorption capacity of cationic dyes on several magnetic nanoparticles, *Acta Chemica Iasi*, **2013**, 21 19-30.
10. Ersu C.B., Braida W., Chao K.P., Ong S.K., Ultrafiltration of ink and latex wastewaters using cellulose membranes, *Desalination*, **2004**, 164(1), 63-70.
11. Metes A., Koprivanac N., Glasnovic A., Flocculation as a treatment method for printing ink wastewater, *Water. Environ. Res.*, **2002**, 72(6) 680-688.
12. Nandy T., Shastry S., Pathe P.P., Kaul S.N., Pre-treatment of currency printing ink wastewater through coagulation-flocculation process, *Water Air Soil Pollut.*, **2003**, 148(1-4), 15-30.
13. Roussy J., Chastellan P., van Vooren M., Guibal E., Treatment of ink-containing wastewater by coagulation/flocculation using biopolymers, *Water SA*, **2005**, 31(3), 369-376.
14. Fernandez J., Kiwi J., Lizama C., Freer J., Baeza J., Mansilla H.D., Factorial experimental design of orange II photocatalytic discoloration process, *J. Photochem. Photobiol. A*, **2002**, 151, 213-219.
15. Purkait M.K., Maiti A., Das Gupta S., De S., Removal of Congo red using activated carbon and its regeneration, *J. Hazard. Mater.*, **2007**, 145, 287-295.
16. Hou X.-yu, Feng J., Liu X.-han, Zhang M.-lin, Comparable Studies of Adsorption and Magnetic Properties of Ferrite $MnFe_2O_4$ Nanoparticles, Porous Bulks and Nanowires, *Chem. Res. Chinese Universities*, **2011**, 27(4), 543-546;
17. Mayo J.T., Yavuz C., Yean S., Cong L., Shipley H., Yu W., Falkner J., Kan A., Tomson M., Colvin V.L., The effect of nanocrystalline magnetite size on arsenic removal, *Sci. Technol. Adv. Mater.*, **2007**, 8, 71-75.
18. Liu Q., Wang L., Xiao A., Gao J., Ding W., Yu H., Huo J., Ericson M., Templated preparation of porous magnetic microspheres and their application in removal of cationic dyes from wastewater, *J. Hazard. Mater.* **2010**, 181, 586-592.
19. Arami M., Limaee N.Y., Mahmoodi N.M., Tabrizi N.S., Removal of dyes from colored textile wastewater by orange peel adsorbent: equilibrium and kinetic studies, *J. Colloid Interface Sci.*, **2005**, 288, 371-376.
20. Jain R., Sikarwar S., Removal of hazardous dye Congo red from waste material, *J. Hazard. Mater.*, **2008**, 152, 942-948.
21. Yermiyahu Z., Lapides I., Yariv S., Visible absorption spectroscopy study of the adsorption of Congo Red by montmorillonite, *Clay Miner.*, **2003**, 38, 483-500.
22. Wang X.S., Chen J.P., Biosorption of Congo Red from aqueous solution using Wheat Bran and Rice Bran: batch studies, *Sep. Sci. Technol.*, **2009**, 44, 1452-1466.
23. Yu Y., Zhuang Y.Y., Wang Z.H., Qiu M.Q., Adsorption of water-soluble dyes onto resin NKZ, *Ind. Eng. Chem. Res.*, **2003**, 42, 6898-6903.
24. Zhou L., Gao C., Xu W., Magnetic dendritic materials for highly efficient adsorption of dyes and drugs, *ACS Appl. Mater. Interface*, **2010**, 2, 1483-1491.
25. Zargar B., Parham H., Hatamie A., Fast removal and recovery of amaranth by modified iron oxide magnetic nanoparticles, *Chemosphere*, **2009**, 76 554-557.
26. Zhang S.X., Niu H.Y., Cai Y.Q., Zhao X., Shi Y.L., Arsenite and arsenate adsorption on coprecipitated bimetal oxide magnetic nanomaterials: $MnFe_2O_4$ and $CoFe_2O_4$, *Chem. Eng. J.*, **2010**,158, 599-607.

27. Dumitru R., Papa F., Balint I., Culita D., Munteanu C., Stanica N., Ianculescu A., Diamandescu L., Carp O., Mesoporous cobalt ferrite: A rival of platinum catalyst in methane combustion reaction, *Appl. Catal. A: Gen.,* **2013**, 467, 178-186.
28. Paulus M., *Preparation methods of ferrites*, Academic Press, Eds. P. Hagenmüller, 1972, pp. 487.
29. Prithviraj Swamy P.M., Basavaraja S., Lagashetty A., Srinivas Rao N.V., Nijagunappa R., Venkataraman A., Synthesis and characterization of zinc ferrite nanoparticles obtained by self-propagating low-temperature combustion method, *Bull. Mater. Sci.*, **2011**, 34(7), 1325-1330.
30. Nejati K., Zabihi R., Preparation and magnetic properties of nano size nickel ferrite particles using hydrothermal method, *Chemistry Central Journal*, **2012**, 23, 1-6.
31. Suryanarayana C., Norton M.G., *X-Ray Diffraction A Practical Approach*, Plenum Press, New York, 2008, pp. 207.

NEW FRONT. CHEM. (**2014**)
Volume 23, Number 1, pp. 11-20
ISSN 2393-2171; ISSN-L 2393-2171

Former: Ann. West Univ. Timisoara – Series Chem.
ISSN: 1224-9513

Review

AIDS DESTROYS IMMUNE DEFENSES: HYPOTHESIS

***Francisco Torrens*[1,♣] *and Gloria Castellano*[2]**

[1]Francisco Torrens, Institut Universitari de Ciència Molecular, Universitat de València, Edifici d'Instituts de Paterna, P. O. Box 22085, E-46071 València, Spain
[2]Departamento de Ciencias Experimentales y Matemáticas, Facultad de Veterinaria y Ciencias Experimentales, Universidad Católica de Valencia *San Vicente Mártir*, Guillem de Castro-94, E-46001 València, Spain

ABSTRACT

In a hypothesis, the immune-system devastation that performs acquired immunodeficiency syndrome (AIDS) arises from the permanent evolution of human immunodeficiency virus (HIV) in humans. After the initial rapid proliferation of HIV in humans the infection remains controlled for a certain period by a strong immune response, in which affected people do not show AIDS symptoms. However, after some years HIV ends to defeat the defence system and AIDS is manifested. In order to explain the progression an evolutionary hypothesis was proposed: HIV experiences mutations, which cause variants. After a certain number of variants the immune system collapses.

Keywords: human immunodeficiency virus type 1, acquired immunodeficiency syndrome, evolutionary hypothesis, mathematical model, human immune response.

1. INTRODUCTION

Escultura reviewed qualitative mathematics and modelling [1]. Barillot *et al*. examined the computational systems biology of cancer [2]. Wang analyzed complex diseases with a mathematical perspective [3]. Simonyi revised the cultural history of physics [4]. Although viruses be not metabolizing cells and considered forced cell parasites, they played an important role in life evolution since its emergence. The human diseases of human immunodeficiency virus type 1 (HIV-1) and hepatitis C virus cannot be understood without the evolutionary framework. Developments in theory, technology, medicine and study of human disease with respect to virus evolution occurred. Reverse transcription broke the

♣ Correspondent author: torrens@uv.es

molecular genetics central hypothesis (*The Central Dogma*), *i.e.*, deoxyribonucleic acid (DNA) makes ribonucleic acid (RNA) makes protein, was established *via* retroviruses.

The HIV presents a health, social and economic impact. Current therapies control infection but neither healer treatment nor effective vaccine. In order to achieve the objectives, one should take into account HIV genetic variability and rapid evolution associated (*e.g.*, with the appearance of drug-resistance variants, antigenic changes). The HIV-1 represents a real-time bioevent in human evolution that confirms the importance of quasispecies and retroviruses to human biology. Human and primate evolution was significantly affected by earlier, prevalent primate retroviruses. From the earliest events in evolution of prebiotic replicators to recent ones in human evolution, *e.g.*, emergence in human-specific HIV, viral evolution is expected to show profound effects on the evolution of life. A question follows. How do HIV variation and adaptation lead to a collapse of the human immune system?

In an earlier publication the phylogeny of anthropoid apes was reported [5]. Fractal [6] and hybrid-orbital [7,8] analyses of protein tertiary structure were informed. Complex multicellular systems and tumour–immune cells competition were modelled [9]. Structural classification of complex molecules by information entropy and equipartition conjecture was published [10-12]. Molecular classification, diversity, complexity and emergence were informed [13-15]. The periodic classification of HIV inhibitors was reported [16]. The molecular classifications of thiocarbamates with cytoprotection activity *vs*. HIV [17], styrylquinolines as HIV integrase inhibitors [18] and *N*-aryloxazolidinone-5-carboxamides as HIV protease inhibitors [19] were informed. Current study of molecular evolution benefits from structural data [20]. Mucoadhesive polymer hyaluronan was published as drug delivery vehicle [21]. Reflections on the nature of the periodic table of the elements were informed [22]. In the present report, the basic model of virus dynamics and HIV–evolution relationship are reviewed with the aim to provide a broad sketch of the fundamental human–HIV biophysical forces that enable and constrain HIV evolution and disease. Despite the importance of biomacromolecule's structures and conformational dynamics to their functions and fitnesses, phylogenetic methods embody their minimal biophysical knowledge. The following section presents the computational model. In the next section, some themes are reviewed and discussed. Finally, the last section summarizes our remarks.

2. MODEL

Basic model of virus dynamics considers uninfected target cells T, productively infected cells I and virus particles V [23]. Uninfected cells are produced at a constant rate σ and die at rate $\delta_T T$. Virus particles infect uninfected cells at a rate proportional to the product of their abundances βTV, and infected cells die at rate δI. Virus is produced from infected cells at rate pI and is cleared at rate cV, which causes system of ordinary differential equations (ODEs):

$$dT/dt = \sigma - \delta_T T - \beta TV \quad (1)$$

$$dI/dt = \beta TV - \delta I \quad (2)$$

$$dV/dt = pI - cV \quad (3)$$

The model (*cf*. Fig. 1) was used as a starting point for explaining HIV dynamics. It describes quantities in the whole body or in a given volume of blood plasma/tissue depending on scaling. The ODEs define change rate of every quantity and every term corresponds to a

production/decay process. Decay-rate reciprocal defines the average lifespan, which results $1/\delta_T$, $1/\delta$ and $1/c$ for uninfected and infected cells, and virus particles, respectively. The model captures the dynamics of a single mixed compartment with large homogeneous populations of cells and viruses that undergo asynchronous infection and cell cycles. Full HIV complexity is not captured by the model. However, the model is used as a consensus starting point and extended to more complexity. Building a single *full model* of HIV dynamics that describe all biosystem details is not feasible. A complex model becomes intractable making it impossible to dissect individual-processes roles in the system. Complexity implementation needs to be guided by the particular research question and kept at the minimum possible level. The model is nonlinear and a general solution for the time course of its variables cannot be derived. Its analysis provides insight. In the absence of virus the model attains an uninfected equilibrium with $\hat{T}_U = \sigma/\delta_T$, $I = 0$, $V = 0$. If virus is added to the system the infection takes hold or peters out depending on the parameters. The conditions for successful infection are summarized in the basic reproductive ratio R_0, which describes the number of cells infected by a single infected cell that is added to an uninfected equilibrium. If $R_0 < 1$, infected cells cannot replace themselves during their lifetime and their numbers dwindle steadily towards zero. If $R_0 > 1$, the number of infected cells rises to a transient peak and the system settles to an infected equilibrium. In the model it results: $R_0 = \beta\sigma p/\delta\delta_T c$. The infected equilibrium is at $\hat{T} = \delta c/\beta p$, $\hat{I} = \sigma/\delta - \delta_T c/\beta p$, $\hat{V} = p\hat{I}/c$. An established infection indicates $R_0 > 1$. Lack of infection may indicate viral-invasion failure but also lack of real exposure. Highly exposed uninfected individuals present $R_0 < 1$, which would indicate HIV systemic resistance. Alternatively, an efficient innate immune response or a lack of appropriate target cells at the entry site may block virus access to the main target cell population in the individuals. Homozygous carriers of C-C chemokine receptor type 5 (CCR5)Δ32 deletion mutant lack susceptible target cells at the entry sites important in sexual transmission and are apparently resistant to infection by the route. However, the infection resistance is breached if viruses able to infect target cells that reside in the systemic circulation are transmitted directly into blood.

Figure 1: The scheme of the basic model of human immunodeficiency virus infection

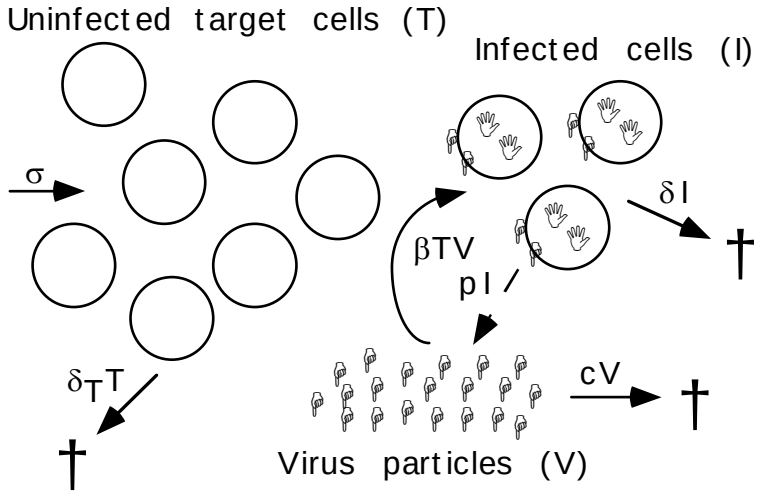

3. APPLICATION

3.1. Results

Longitudinal studies of patients, infected with HIV-1, revealed a long and variable incubation period between infection and development of acquired immunodeficiency syndrome (AIDS). Data from a small number of infected patients showed temporal changes in number of genetically distinct strains of HIV throughout incubation period, with a slow but steady rise in diversity. A dynamic-interaction model between HIV diversity and human immune system showed an antigen diversity threshold, below which the immune system regulates HIV population, but above which HIV inhabitants induce collapse of cluster of differentiation of T_4-receptor subtype (CD_4^+) of thymus (T)-dependent lymphocyte populace [24]. It showed that antigenic diversity is AIDS cause, not consequence. Its comparison with data assessed how timing of chemo/immunotherapy application influences AIDS progress.

In a longitudinal study of HIV patients, fluctuations in specificity of cytotoxic T-lymphocytes (CTLs) were matched by variability in proviral group-specific antigen (*gag*) DNA epitope sequences [25]. Variants of HIV are unrecognized by autologous T-cells. Mutations accumulation in T-cell antigenic targets provides an immune-escape mechanism.

Theories of HIV pathogenesis explain the long and variable infection–AIDS delay. McLean reviewed the theories in the context of a simple model of HIV–immune system interactions from which a theoretical progression index was derived [26].

Figure 2: Lymph node (LN) germinal centres during HIV. FDC: follicular dendritic cell; PB: peripheral blood

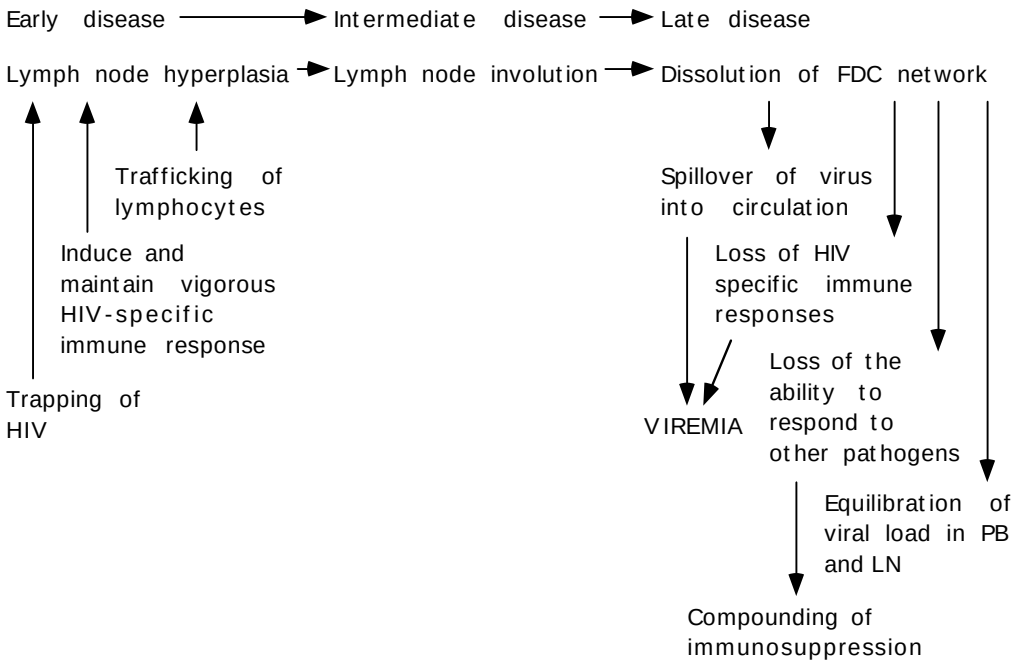

Is HIV necessary and sufficient to cause AIDS? Is AIDS an autoimmune disease triggering apoptosis? Is HIV infection cause of T-helper lymphocyte depletion? What are HIV-tropism significance and macrophages/dendritic cells role in AIDS? Is there HIV latency? Why is there a long infection–AIDS period? Is HIV variation an aspect of pathogenesis? Do virulent strains emerge? Although Weiss provided answers he focussed on salient points [27]. Tropism and burden of HIV infection correlate with AIDS manifestations.

Immunopathogenic mechanisms underlying HIV AIDS are complex; AIDS is multifactorial with multiple overlapping phases (*cf*. Fig. 2) [28]. Viral burden is substantial and HIV replication occurs throughout entire infection. Inappropriate immune activation and elevated secretion of certain cytokines compose pathogenesis. Immunosuppression occurs together with a disruption of immune-system microenvironment, which is unable to regenerate spontaneously. Therapeutic strategies in HIV AIDS should not be one-dimensional, but rather linked to complex pathogenic components of AIDS and should address every recognized pathogenic process for therapeutic intervention possibility.

A protein antigen contains epitopes, which is recognized by CTLs, but in a characteristic antiviral immune response *in vivo*, CTLs recognize a small number of potential epitopes (*immunodominance*). Antigenic variation in CTL epitopes was shown for HIV-1 and other viruses, and *antigenic escape* is responsible for persistence. Nowak group developed a model, which dealt with interaction between CTLs and multiple epitopes of a genetically variable pathogen, and showed that nonlinear competition among CTL responses *vs*. different epitopes explains immunodominance [29]. Their model showed that an antigenically homogeneous pathogen population induces a dominant response *vs*. a single epitope, whereas a heterogeneous pathogen population stimulates fluctuating responses *vs*. multiple epitopes. Antigenic variations in immunodominant epitope shift responses to weaker epitopes and reduce immunological control of pathogen population, which is consistent with longitudinal studies on CTL responses in HIV-1 infected patients. For vaccine design, their model showed that major response should be directed *vs*. conserved epitopes even subdominant.

Evolutionary theory stands by that random mutation in the genetic material of an organism results in a characteristic, which provides it an advantage; *i.e*., the mutated organism can surpass better than its equals the obstacles to survive and is improved, gifted for reproducing prolifically. In generations, the lineage that shares the same feature predominates among population components, showing preferred *vs*. other members. Environmental pressure determines which features are selected for its propagation in a population. When Nowak group faced HIV vital cycle, it was evident that HIV was especially equipped to evolve enjoying the protection of the characteristics of the pressure with which it was faced. Its genetic constitution changes continually. It is known that a high mutation rate increases the probability that some genetic change cause an advantage. Genetic variability of HIV is because of an own enzyme: reverse transcriptase (RT). In cell inside, HIV resorts to RT to copy its genome from RNA to double-stranded (ds)DNA, which is inserted in a host chromosome from where it directs the production of more HIV RNA/proteins which, in turn, are assembled to give HIV particles, which escape the cell. The HIV mutates because RT is prone to make errors. Every time RT copies RNA into DNA the new DNA differs from the preceding generation in one site. Such a behaviour converts HIV in the most variable virus. The high replicative rate of HIV redoubles the probability that arise a mutation useful for it. In order to esteem HIV multiplication, notice the findings of Shaw and Ho groups (1995). In an infected patient, every day $>10^9$ new HIV particles are produced. In immune-activity

absence, HIV population is doubled every two days. From original HIV to every HIV particle that be in the organism ten years after the infection, thousands of generations will come up.

From HIV evolutionary potential, Nowak group conceived a model to explain in which way HIV resists complete eradication and usually causes AIDS at the end of a long period. Their proposal assumed that the incessant mutation of HIV genes would lead to a continued production of HIV variants able to break, till certain point, the defences of the immune system operative at a given moment. Variants would arise when the genetic mutations would bear changes in the structure of HIV peptides (epitopes) recognized by the immune system. Frequently, the changes cause no effect on the immune activity but sometimes they make that a peptide become invisible to the organism defences. Involved HIV particles, carriers of a lesser number of recognizable epitopes, escape notice more easily from the immune system. The hypothesis proposed that a mutation, able to avoid that an epitope be recognized, lends HIV variant a survival advantage at least till the immune system discover it and react with the altered peptide, response which reduces HIV charge for some time but other *elusive mutants* arise and the cycle continues preventing total infection elimination. Checking a scheme of this nature is difficult resorting exclusively to clinical tests because detailed monitoring of nonlinear HIV–immune system interactions is impossible. They attended a computer simulation in which HIV population evolved in response to immune pressure. They argued that if the model produces the known patterns of HIV progression, evolutionary scene results interesting. Equations that constituted model kernel reflected characteristics that they considered important in HIV-infection progression: HIV alters immune function causing death of co-adjuvant T-cells. Greater HIV levels cause death of more T-cells. The HIV promotes production and release of *elusive mutants*, which avoid the normal attack of the immune system so that the mutants are propagated among HIV population. After a period, however, defences advert the elusive presence and their population decays. Their model distinguished between two types of immune responses: those that recognize epitopes that easily suffer mutations and the ones that know conserved epitopes. The simulation reproduced the characteristic delay between HIV infection and sudden rise of HIV levels that ends present in the organism. It provided an explanation of why the cycle constituted by new *elusive mutant* and repression does not continue in an undefined way but it culminates in an uncontrolled HIV replication: almost complete loss of co-adjuvant T-cell population and AIDS instauration. The model indicated that the immune system could frequently set up a simultaneous defence intense enough *vs.* different HIV variants. Despite that, a moment arrives usually at the end of many years in which multiple HIV alternatives coincide. When threshold is broken the immune system is incapable of controlling HIV. *Diversity threshold* (rupture point) differs from one person to another; *e.g.*, if the immune system is weak from the beginning a relatively low number of variants ruin organism defences.

Why does the presence of multiple HIV variants weaken the immune system yield? Every member of HIV army is a generalist able to attack any enemy cell that it find. Every immune soldier is a specialist able to recognize an HIV soldier only if this carries a flag of a determined colour. Let one accept that both armies present equal power, if every specialist of the immune army recognizes the same flag and every soldier of HIV faction bears such standard. Let one assume that HIV army is constituted by three groups, every one with a different flag, and that in response the immune specialists are split into three groups, every one able to know a different flag, in which conditions the immune army is in disadvantage.

An immune specialist recognizes and attacks only one out of three enemy soldiers that it find. Soldiers of HIV continue attacking any specialist that waylays and end winning the war.

3.2. Discussion

Life emergence on Earth is a unique historical process. Like in a trial, one investigates to establish main facts. Tools should be science and history. Molecular genetics central hypothesis states that DNA is transcribed to RNA, which is then translated into proteins. However, reverse transcription allows RNA to be transcribed back into DNA. *Molecularity* in biology took scientists to recognize RNA role in bioprocesses and that it preceded DNA as genetic material. The success of these approaches shows a deep synergy between biophysics and evolution. As Darwin noted how natural selection enabled simple life to evolve into complex one, Pross evolution theory hinted how simple but fragile replicators complexified into intricate life chemical systems. A reorientation of research in translational (marketable) science is necessary. In chemistry and physics the reorientation can be carried out by bench-guided reverse engineering. Ideas in biology should be valued by the number of questions that they generate. On one hand, in biology (science) the reorientation can be performed by clinic-guided reverse engineering. The same applies to medicine (the technology of biology). A scheme of the reorientation of research in translational science is in Fig. 3.

Figure 3: Scheme of the reorientation of research in translational science

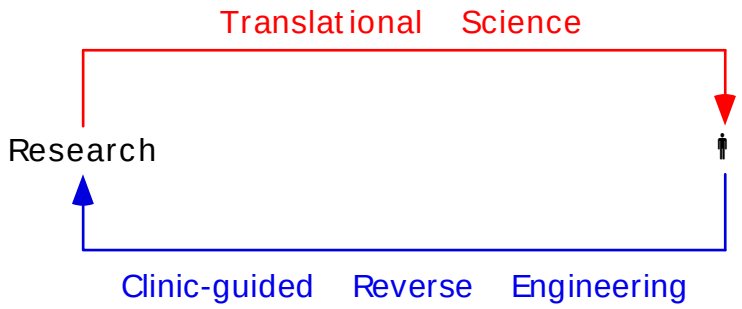

Figure 4: Scheme of the reorientation of research in translational science in a society

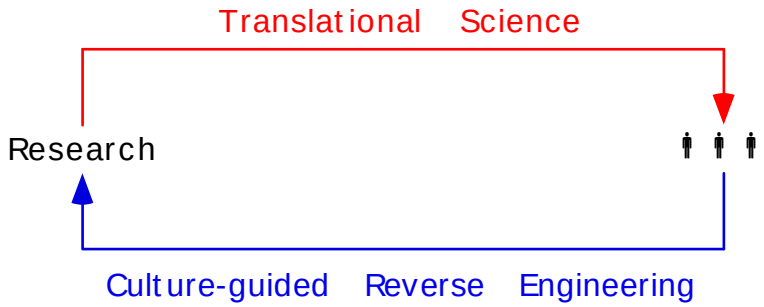

On the other hand, in a society the reorientation of research in translational science can be done by culture-guided reverse engineering. A scheme of this reorientation is in Fig. 4.

4. CONCLUDING REMARKS

From the present review and discussion the following remarks can be drawn.

1. It was provided a sketch of the fundamental man–human immunodeficiency virus (HIV) biophysical forces that enable and constrain its evolution and disease. The evolutionary theory turns out to be essential to understand human–HIV relationship and place it in the whole of human diseases. The objective of developing effective antiviral drugs *vs*. HIV was achieved but obtaining a vaccine is distant. Variability of HIV, because of the elevated mutation rate and recombination, together with the latency that characterizes infection, makes it difficult to combat. Knowledge and understanding of the evolutionary mechanisms that govern HIV evolution are key to know not only how it emerged but also how it develops, to treat it, it changes in the future and to eradicate it. An evolutionary scene explained *via* a long way why HIV infection progress slowly and ends destroying the immune system. Advances made *via* computational models were highlighted (basic model of virus dynamics, *etc*.) because discoveries in HIV dynamics, evolution and disease were pioneered *via* simple modelling of biophysical processes that are too complex to be studied in full details.

2. Neglected by modellers, recombination effect in HIV witnessed a rapid interest. The models show that recombination does not facilitate drug-resistance evolution as was frequently assumed. It presents an effect on the expected frequency of combinations of drug resistance mutations, in therapy absence, and rate of fixation of the combinations in the presence of drugs. Whether recombination facilitates or impedes drug-resistance evolution depends on either stochastic effects are the primary force generating statistical associations or epistatic-interactions sign. Recombination-effect understanding in HIV will not only shed light on drug-resistance evolution but also provide insights into other questions of evolutionary biology: what is the benefit of sexual reproduction, *etc*.

3. A current picture of HIV population and evolutionary dynamics was outlined within an infected individual. Progress was made in the area since 2000: clearly no other virus infection exists for which a comparable effort was undertaken to quantify its dynamical behaviour. The quantitative approach led to HIV-infection understanding. However, uncertainty still surrounds many central aspects of viral population dynamics and evolutionary response to changing selection pressures. Quantitative HIV virology was born in 1995 and is still in its childhood. The evolutionary theory turns out to be essential to understand human nature and place it in the whole of living beings. Looking into the future, we expect to witness rising collaboration between the fields of biophysics, biochemistry, cell chemistry, evolution, virology and medicine, as well as between theory/computation and experiment to decipher many aspects of the evolutionary forces that shaped the biological roles of viruses. Further work will be devoted to the reorientation of research in translational science.

ACKNOWLEDGEMENT

One of us, F. T., thanks support from the Spanish Ministerio de Economía y Competitividad (Project No. BFU2013-41648-P) and EU ERDF.

REFERENCES

1. Escultura, E. *Qualitative Mathematics and Modeling: Theoretical and Practical Applications of QMAM*; Lap Lambert: Saarbrücken, Germany, 2013.
2. Barillot, E.; Calzone, L.; Hupe, P.; Vert, J.P.; Zinovyev, A. *Computational Systems Biology of Cancer*; CRC: Boca Raton, FL, 2013.
3. Wang, G. *Analysis of Complex Diseases: A Mathematical Perspective*; CRC: Boca Raton, FL, 2014.
4. Simonyi, K. *A Cultural History of Physics*; CRC: Boca Raton, FL, 2012.
5. Torrens, F. Filogénesis de los simios antropoides. *Encuentros en la Biología* **2000**, *8*(60), 3–5.
6. Torrens, F. Análisis fractal de la estructura terciaria de las proteínas. *Encuentros en la Biología* **2000**, *8*(64), 4–6.
7. Torrens, F. Fractals for hybrid orbitals in protein models. *Complexity International* **2001**, *8*, torren01-1–13.
8. Torrens, F. Fractal hybrid-orbital analysis of the protein tertiary structure. *Complexity International*, submitted for publication.
9. Torrens, F.; Castellano, G. Modelling of complex multicellular systems: Tumour–immune cells competition. *Chemistry Central Journal* **2009**, *3*(Suppl. I), 75-1–1.
10. Torrens, F.; Castellano, G. Classification of complex molecules. In *Foundations of Computational Intelligence*; Hassanien, A.E., Abraham, A. Eds.; Stud. Comput. Intelligence No. 205; Springer: Berlin, Germany, 2009; Volume 5, pp. 243–315.
11. Torrens, F.; Castellano, G. Structural classification of complex molecules by artificial intelligence techniques. In *Advanced Methods and Applications in Chemoinformatics: Research Progress and New Applications*; Castro, E.A., Haghi, A.K., Eds.; IGI Global: Hershey, PA, 2012; pp. 25–91.
12. Torrens, F.; Castellano, G. Structural classification of complex molecules by information entropy and equipartition conjecture. In *Chemical Information and Computational Challenges in 21st Century*; Putz, M.V., Ed.; Nova: New York, NY, 2012; pp. 101–139.
13. Torrens, F.; Castellano, G. Molecular diversity classification via information theory: A review. *ICST Transactions on Complex Systems* **2012**, *12*(10-12), e4-1–8.
14. Torrens, F.; Castellano, G. Complexity, emergence and molecular diversity *via* information theory. In *Complexity Science, Living Systems, and Reflexing Interfaces: New Models and Perspectives*; Orsucci, F., Sala, N., Eds.; IGI Global: Hershey, PA, 2013; pp. 196–208.
15. Torrens, F.; Castellano, G. Molecular classification, diversity and complexity via information entropy. In: *Chaos and Complex Systems*; Stavrinides, S.G., Banerjee, S., Caglar, H., Ozer. M., Eds.; Springer: Berlin, Germany, 2013; Volume 4, pp. 1–19.

16. Torrens, F.; Castellano, G. Table of periodic properties of human immunodeficiency virus inhibitors. *International Journal of Computational Intelligence in Bioinformatics and Systems Biology* **2010**, *1*, 246–273.
17. Torrens, F.; Castellano, G. Molecular classification of thiocarbamates with cytoprotection activity against human immunodeficiency virus. *International Journal of Chemical Modeling* **2011**, *3*, 269–296.
18. Torrens, F.; Castellano, G. Molecular classification of styrylquinolines as human immunodeficiency virus integrase inhibitors. *International Journal of Chemical Modeling*, in press.
19. Torrens, F.; Castellano, G. Molecular classification of *N*-aryloxazolidinone-5-carboxamides as human immunodeficiency virus protease inhibitors. In *Emerging Trends in Computational Biology, Bioinformatics, and Systems Biology*; Tran, Q.N., Arabnia, H.R., Eds.; Elsevier: Amsterdam, The Netherlands, in press.
20. Torrens, F.; Castellano, G. A tool for interrogation of macromolecular structure. *Journal of Materials Science and Engineering B* **2014**, *4*(2), 55–63.
21. Torrens, F.; Castellano, G. Mucoadhesive polymer hyaluronan as biodegradable cationic/zwitterionic-drug delivery vehicle. *ADMET & DMPK* **2014**, *2*, 235–247.
22. Torrens, F.; Castellano, G. Reflections on the nature of the periodic table of the elements: Implications in chemical education. In *Synthetic Organic Chemistry*; Seijas, J.A., Vázquez Tato, M.P., Lin, S.K., Eds.; MDPI: Basel, Switzerland, 2015; Volume 18, pp. 1–15.
23. Müller, V.; Bonhoeffer, S. Intra-host dynamics and evolution of HIV infection. In *Origin and Evolution of Viruses*; Domingo, E., Parrish, C.R., Holland, J.J., Eds.; Academic: London, UK; 2008; pp. 279–301.
24. Nowak, M.A.; Anderson, R.M.; McLean, A.R.; Wolfs, T.F.W.; Goudsmit, J.; May, R.M. Antigenic diversity thresholds and the development of AIDS. *Science* **1991**, *254*, 963–963.
25. Phillips, R.E.; Rowland-Jones, S.; Nixon, D.F.; Gotch, F.M.; Edwards, J.P.; Ogunlesi, A.O.; Elvin, J.G.; Rothbard, J.A.; Bangham, C.R.M.; Rizza, C.R.; McMichael, A.J. Human immunodeficiency virus genetic variation that can escape cytotoxic T cell recognition. *Nature (London)* **1991**, *354*, 453–459.
26. McLean, A.R. The balance of power between HIV and the immune system. *Trends in Microbiology* **1993**, *1*, 9–13.
27. Weiss, R.A. How does HIV cause AIDS? *Science* **1993**, *260*, 1273–1279.
28. Fauci, A.S. Multifactorial nature of human immunodeficiency virus disease: Implications for therapy. *Science* **1993**, *262*, 1011–1018.
29. Nowak, M.A.; May, R.M.; Phillips, R.E.; Rowland-Jones, S.; Lalloo, D.G.; McAdam, S.; Klenerman, P.; Köppe, B.; Sigmund, K.; Bangham, C.R.M.; McMichael, A.J. Antigenic oscillations and shifting immunodominance in HIV-1 infections. *Nature (London)* **1995**, *375*, 606–611.

NEW FRONT. CHEM. (**2014**)
Volume 23, Number 1, pp. 21-38
ISSN 2393-2171; ISSN-L 2393-2171

Former: Ann. West Univ. Timisoara – Series Chem.
ISSN: 1224-9513

Review

CHEMICAL MODELING USING GRAPHS: FROM ADJACENCY MATRIX TO RANDIĆ CODING OF DNA

Alexandru V. Botez, Mihai V. Putz ♣
Laboratory of Computational and Structural Physical-Chemistry for Nanosciences and QSAR, Department of Biology – Chemistry, Faculty of Chemistry, Biology, Geography, West University of Timisoara, 16 Street Pestalozzi, Timisoara 300115, Romania

ABSTRACT

Graph Theory offers tools for a wide area of fields: mathematics, physics, chemistry, biology, biochemistry, bioinformatics and computer science. Graphical representations have been used not only for comparative studies of genetic material, but also to visualize real or fictional relationships and interactions between vertices. This review aims to highlight some of the most frequently used transdisciplinary applications of graph theory and to present the steps necessary to build such graphs. The development of graphical representations enabled the comparisons of similarities and differences between long DNA sequences.

Keywords: graph theory, graphical modeling, transdisciplinary applications, virtual genetic code, brain connectivity

1. INTRODUCTION

The history of Graph theory begins in 1735 with Leonhard Euler and the Seven Bridges of Königsberg puzzle, in which one must cross each bridge only once to arrive at the starting point. Euler demonstrated that the puzzle has no solution [1].

A graph (Figure 1) is an ordered pair G = (V, E) comprising of V vertices or nodes together with E edges or lines. A simple graph is undirected [2].

♣ Correspondent author: Tel: 004(0)-256-592-638, Fax: 004(0)-256-592-620, E-mail: mv_putz@yahoo.com

Figure 1: A basic graph

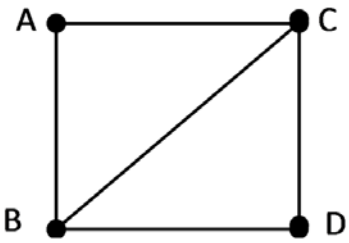

Graph Theory [2] started 35 years ago as a branch of mathematics that studies geometry [3], function-spaces theory [4], geomorphology [5] and combinatorial matrix theory [6]. Graph Theory facilitated the development of Chemical Graph Theory, which enriched QSAR studies and drug modeling [7].

Although Hamori was the one who initiated graphical representations of DNA over two decades ago [8], the first graphical representation of a protein emerged only in the last decade [9].

2. CHEMICAL GRAPH MODELING BASIS

2.1. Types of Chemical Graphs

Types of Graphs are widely presented in literature in the following forms [10, 11]:

- Undirected graph - the edges of an undirected graph have no orientation;
- Directed graph - or digraph is an ordered pair G = (V, E) with V as a set of vertices or nodes and E as a set of ordered pairs of edges or arrows;
- Mixed graph - a graph G which have both directed and undirected edges;
- Multigraph - a graph containing multiple edges and/or loops;
- Quiver - or "multiDigraph" is a directed multigraph which can have more than one arrow from a given source to a given target;
- Simple graph - an undirected graph that has no loops (edges connected at both ends to the same vertex) and no more than one edge between any two different vertices;
- Weighted graph - a graph in which a number (weight) is assigned to each edge. Such weights might represent: costs, lengths or capacities, depending on the specific issue;
- Regular graph - a graph where each vertex has the same number of neighbors;
- Complete graph - connects each vertex to each edge;
- Finite and infinite graphs - a graph G = (V, E) such that V and E are finite sets. An infinite graph is one with an infinite set of vertices or edges or both;
- Subgraph - a subgraph G_0 of G is a graph whose vertices and edges are contained in the graph G;
- Möbius graph - a special kind of simple graph predicted by Heilbronner [12] in the form of a ladder or belt, with the ends connected in a half twist. An important property of the Möbius belt is that it has only one side in 3D space [13] (Figure 2). It was first synthesized in 2003 [14].

Figure 2: Möbius type cyclacene zigzag belt

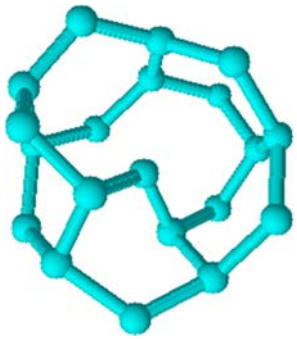

2.2. Types of Graph Matrices

Among the most popular matrices used, we mention [15]:

- Adjacency matrix: A=A(G), with N vertices, yields a NxN symmetric matrix]:

$$[A]_{ij} = \begin{cases} 1 & if \quad i \neq j \quad and \quad e_{ij} \in E(G) \\ 0 & if \quad i = j \quad or \quad e_{ij} \notin E(G) \end{cases} \tag{1}$$

- Adjacency count matrix: DEG=DEG(G), is the number of edges attached to each vertex:

$$[DEG]_{ij} = \begin{cases} \deg(v_i) & if \quad i = j \\ 0 & if \quad i \neq j \end{cases} \tag{2}$$

- Distance matrix: D=D(G), which can be used to calculate the Wiener index (W) and each vertices' contribution to the Wiener index (W):

$$[D]_{ij} = \begin{cases} d_{ij} & if \quad i \neq j \\ 0 & if \quad i = j \end{cases} \tag{3}$$

- Laplacian matrix:

$$[L]_{ij} = [DEG]_{ij} - [A]_{ij} \tag{4}$$

- X matrix:

$$[X]_{ij} = \begin{cases} \left(\deg_{ij}\right)^{1/2} & if \quad e_{ij} \in E(G) \\ 0 & if \quad e_{ij} \notin E(G) \end{cases} \tag{5}$$

- Reciprocal distance matrix [15]:

R=R(G)

$$[RD]_{ij} = [1/D]_{ij} \tag{6}$$

- Detour matrix: the longest path between 2 vertices:

$$[\Delta]_{ij} = \begin{cases} \max\left(p_{ij}\right) & if \quad i \neq j \\ 0 & if \quad i = j \end{cases} \tag{7}$$

- Wiener matrices: W_e, W_p and $W_\Delta = W_p - W_e$ for acyclic graph:
  - Wiener-edge matrix: the product of fragment vertices resulted from the cutting one edge;

$$[W_e]_{ij} = N_{i,e} \times N_{j,e} \quad (8)$$

- Wiener-path matrix: obtained by populating the zero values of the W_e matrix with the number of edges of eider side of a considered path ($V_{i,p}V_{j,p}$), including the path ($V_{i,p}V_{j,p}$);
- Wiener matrix: $W_\Delta = W_p - W_e$, giving the edge-graph contribution to the Wiener index (different from the distance contribution to Wiener);

- Combinatorial matrices: D_p, D_Δ:
  - D_p: the distance-path matrix is based on the distance matrix, but counts all possible path formed inside of the shortest path between two vertices and allows direct calculation of the hyper-Wiener index;
  - $D_\Delta = D_p - D$: gives the non-Wiener values of the hyper-Wiener index;
- Hosoya path matrix: a NxN matrix for acyclic graphs built by cutting an edge *ij* of the graph and calculating the Hosoya index of the resulting subgraphs [16];
- Hosoya index: also known as the Z index, is the total number of groups (k=order of the group, if k=0, Z is always 1) of non adjacent edges; was proposed to predict the order of boiling points for alkane isomers [17]. The sum of this matrix represents the path-Hosoya-Wiener index. Other such matrices are Hosoya edge matrix and Hosoya vertex matrix:

$$Z = \sum_{k=0}^{[V/2]} p(G;k) \quad (9)$$

3. DISCUSSIONS

Graphs are an intrinsic part of understanding connectivity of networks and pathways, be it social, migration, information, biochemical or neurological. Here we survey some of them.

3.1. Computer Science

Applications of graphs in computer science have led to the development of algorithms for solving problems [11, 18], such as:

- Shortest path algorithm in a network;
- Finding a minimum spanning tree;
- Finding graph planarity;
- Algorithms to find adjacency matrices;
- Algorithms to find the connectivity matrices;
- Algorithms to find the cycles in a graph;
- Algorithms for building search engines;
- Ordering of timed events and timed table scheduling;
- Algorithms for computer network security;
- Algorithms for fingerprint technology;
- Algorithms for decision making;

The most popular application of graph theory in computer science is the creation of the World Wide Web, which is nothing else than a large directed graph [19].

3.2. Physics

The crystal structure of compounds can be represented by graphs for the configuration of the face centered lattice [20]. Graphs can also be used for the characterization of molecular dynamics by clustering and geometrical rearrangements during crystallization [21]. Among the newest trends is NMR crystallography of zeolites in which the graph is built atom-by-atom [22]. This method is capable of characterizing crystals even with a low degree of periodicity, unlike diffraction techniques [23].

3.3. Chemistry

The most popular application of graph theory in chemistry is the Hückel molecular orbital theory [24].

Graph theory has been widely used in chemistry to make predictions on the compounds behavior of which we mention some:

- predicting diamagnetic properties of inorganic compounds for QSAR studies [25];
- predicting boiling points of alkanes [26] and their isomers [17];
- predicting branching of alkanes [27] and their thermodynamic stability [28];
- canonical naming of large clusters of isomers [29, 30];
- chemical reaction networks of simple and metabolic pathways [31];
- representation of three-dimensional molecular structures as basic graphs [32];
- predicting molecular similarity [33, 34];
- predicting topological energies and chemical stability of carbon structures [35, 36];

3.4. Biology

On the macro-scale, graph theory is key for the construction of migration routes of populations, models for human urbanization [37] and genealogical trees [38].

On the nano-scale, graph theory enhances QSAR studies and drug design by predicting drug availability interactions [39], toxicological [26] and carcinogenetic properties [40, 41].

3.5. Brain Topography

Graph theoretical modeling of brain connectivity has enhanced the knowledge of the brain's structure and functional systems as its complex networks are characterized by small-world topology [42], modularity [43] and highly connected hubs [44].

Human brain connectivity has been studied using functional MRI [45], diffusion tensor imaging tractography [46], magneto- and electroencephalography [47].

From the construction of the neural graph, the following observations have been made [43, 48-50]:

- the extent of a node (vertex) depends on the number of links to the rest of the network;
- the distance between nodes (edges) that has to be traversed is called a path;
- high node connectivity and short paths translates to high efficiency of parallel information transfer and fast processing;
- long paths offer fast transfer of information between distant dense nodes;
- dense populations of nodes follow hierarchical clustering and they are called hubs or clusters;
- hubs take on different roles in information processing and they are classified in modules;

Analyses of structural networks offer valuable information about the brain architecture, nevertheless, neurophysiological dynamics are hard to elucidate for a healthy individual [51]. When a normal brain is used as a control sample and compared to those with many neurological and psychiatric disorders such as autism, ADHD [52] and schizophrenia [53], it has been studied and observed that they are caused by node dysconnectivity [54].

Great differences have been observed in the brain networks of the sick, still, a certain degree of dissimilarity can also be observed between healthy individuals. Additionaly, complex brain networks are shared between individuals of different species [55].

3.6. Proteomics: The Randić Virtual Genetic Coding

The Virtual Genetic Code is a hypothetical string of nucleic acid bases (A, C, U, G) used to compile an existing protein, by assigning each amino acid (aa) an unique codon. It is possible to reconstruct this hypothetical DNA, while the actual genetic sequence that produces the protein remains unknown [56]. This permits the comparison of similarities and differences of sequences though 2D mathematical objects. These 2D graphical representations do not need to be unique or even to permit the reconstruction of the initial DNA sequence.

Such 2D graphical representations of DNA are the random-walk plot that have the advantage of visualizing certain periodic patterns, but they also hides any repeating patterns [57, 58], as seen in Figure 3.

Figure 3: Graphical representation of the hypothetical RNA of the first 97 amino acids of the human ND6 protein, adapted from Randić [59]; see text for details

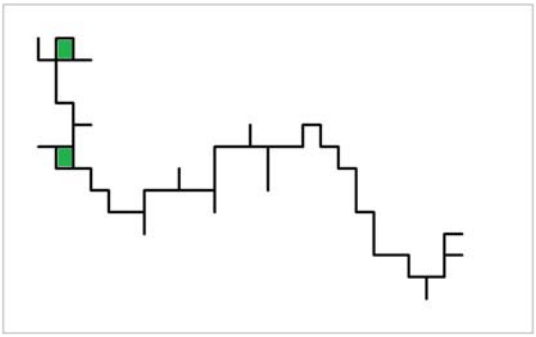

Numerical characterizations can accompany graphical representations of DNA sequences to allow both qualitative and quantitative representations of DNA [60].

This approach is used for characterization of bending and folding of molecular chain, through the use of eigenvalues from the distance/distance (D/D) matrix, where (*i*, *j*) are two Euclidean distances between atoms, respectively through space and which are measured along the chain. Such eigenvalues of increasingly bent structures can be seen in the following graphical representation, as the Euclidean distances get smaller and the theoretical distances remain the same (Figure 4) [61].

Figure 4: Illustration of planar rotational isomers of eight-carbon polyene chains. While being discriminated upon the eigen-values of the extremes-connecting Euclidian distances, after [62]

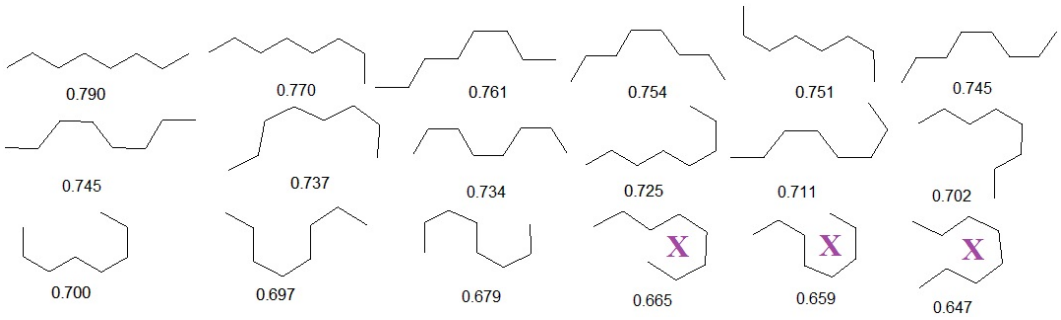

The D/D matrix for proteins takes the shape of a compressed constant size 20X20 matrix, which measures the sum of all distances for the selected amino acid, as seen in Table 1.

Beside the D/D matrix or the adjacency, in a similar manner, the construction of the adjacency-count (*i*,*j*) matrix is possible [64]. One proceeds by building a matrix of appropriate size and counting how many times *i* is the neighbor of *j*. These matrices are especially useful for the comparison of genetic material [62].

The comparisons of similarities and differences between long DNA sequences were otherwise almost impossible without the development of graphical representations. The basic methods in comparative studies of DNA use the three letter codons as its building blocks. While the correspondence between codons and amino acids is not unique, the differences in the coding of an amino acid can be assigned a squared weight value [62].

The metric comparison of DNA is achieved by assigning a number to each amino acid (Figure 5) and by aligning the 2 sequences. This approach coupled with codon weighing gives satisfactory results by itself, but it can be improved by shifting the sequence with one or more codons to gives a superior alignment of DNA from different species [62].

For simplification of numeric sequence comparison, all similarities are assigned with 0-value while all differences with 1-value; this way, one can easily conclude the degree of similarity [62]. Similar to the alignment presented earlier, the spectrum alignment of DNA is both simple and effective. By assigning to each of the four bases, the numbers 1 to 4, one obtains an array of digits that can be processed in the same way already mentioned [65, 66], thus obtaining a DNA number sequence (Figure 6).

Table 1: Alphabetical order of the distance matrix for ND6 human protein, after [63]

	Ala	**Arg**	**Asn**	**Asp**	**Cys**	**Gin**	**Glu**	**Glv**	**His**	**lie**	**Leu**	**Lvs**	**Met**	**Phe**	**Pro**	**Ser**	**Thr**	**Tip**	**Tyr**	**Val**
A	0																			
R	113	0																		
N	35	78	0																	
D	70	45	36	0																
C	113	227	149	184	0															
Q	-	-	-	-	-	0														
E	72	47	38	6	184	-	-													
G	33	147	68	103	80	-	104	0												
H	-	-	-	-	-	-	-	-	0											
I	5	119	40	75	108	-	77	28	-	-										
L	68	182	103	138	46	-	CO	34	-	62	0									
K	50	162	84	118	67	-	169	17	-	44	22	0								
M	23	213	134	169	15	-	169	65	-	94	31	52	0							
F	44	172	93	128	55	-	128	24	-	53	9	13	41	0						
P	50	154	75	110	73	-	111	8	-	34	28	16	59	18	0					
S	68	182	103	138	46	-	138	34	-	63	2	21	31	10	29	0				
T	23	133	56	89	95	-	89	16	-	18	49	28	80	39	25	49	0			
W	80	40	47	12	193	-	8	112	-	85	147	126	178	137	120	147	97	0		
Y	43	157	78	113	71	-	113	10	-	38	25	8	56	15	8	25	24	122	0	
V	12	126	48	83	100	-	85	21	-	7	55	38	86	45	27	55	15	93	31	0

Figure 5: Spectrum representation of the *amino acids sequence* for the *human ND6* protein, adapted from Randić [59]; see text for details

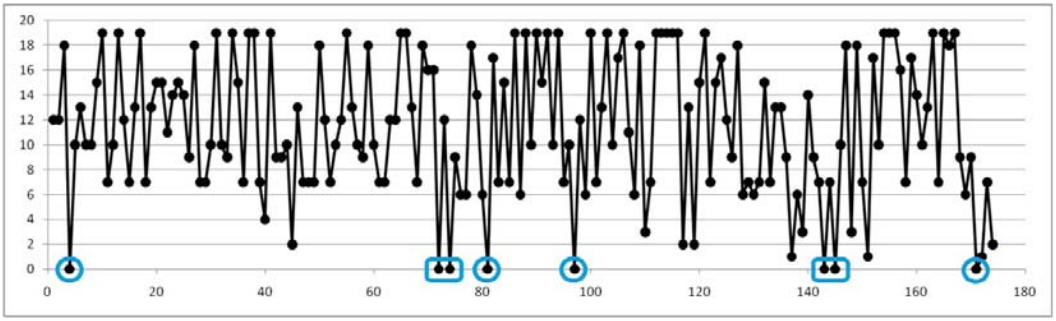

Figure 6: Spectral representation of the *hypothetical RNA* of the first 30 amino acids for the human ND6 protein, adapted from Randić [59]; see text for details

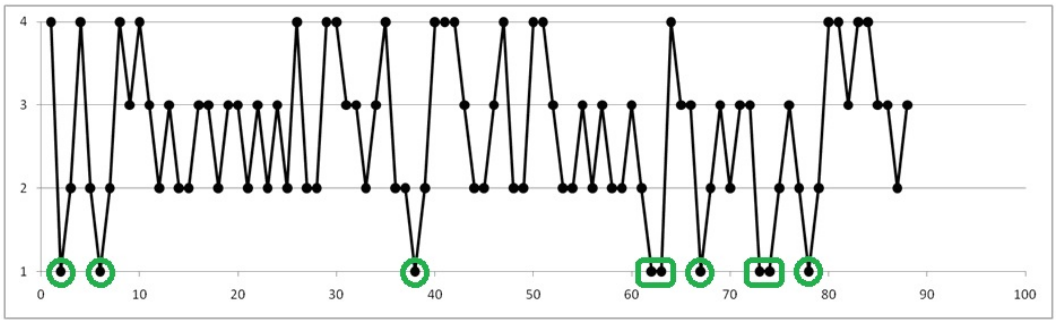

While DNA can be written as a long array of 4 letter (or numbers), after the transcription to RNA, this numbering can be maintained with a loss of information on its secondary structure [67], or the numbering can be increased to 8 or 12. The first set of 4 belongs to the unbound bases, the second belongs to the hydrogen bound bases, while the third belongs to the bases that are hydrogen bound to the second group. This smilingly large pool of numbers for only 4 letters faithfully translates the secondary structure of RNA from START to FINISH [62]. These number sequences allow writing and reading as well as a full reconstruction of the parent genetic material.

Figure 7: Graphical representation of Jeffrey's Magic Square for the hypothetical RNA of the first 30 amino acids for the human ND6 protein of Figure 6, adapted from Randić [59]; see text for details

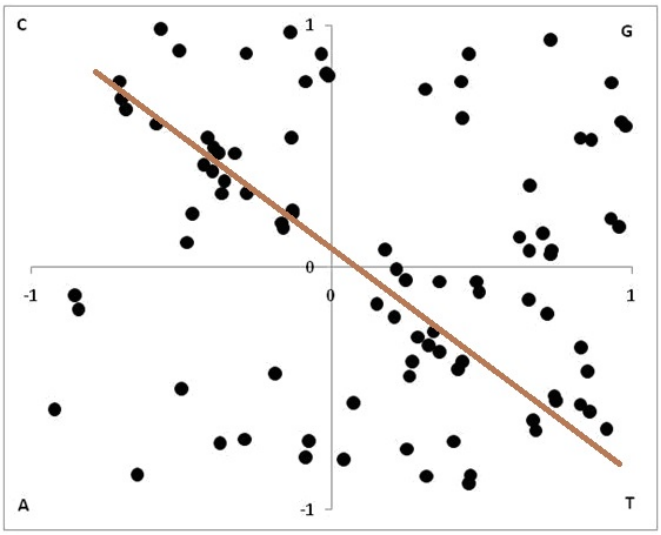

Jeffrey's Magic Square is a highly compact 2D map created by assigning the four bases A, C, G and T to each corner of a square [68]. The sequence starts in the center of the square and moves half the distance to the designated corner of the first letter, then half the distance to

the next sequenced base, leading to a collection of points that represents that unique strand of genetic material (Figure 7). This method of DNA comparison which looks similar to Michael Barnsley's "Chaos Game" [69], is useful only for comparing small DNA sequences.

For the application of Jeffrey's Magic Square to proteins the shape of the representation changes from a square to an Icosagon. A circle with 20 points is the optimized representation of Jeffrey's modified square for proteins, even though it creates a more chaotic pattern [62].

Before the graphical representations of DNA and proteins, their mathematical processing offers all the necessary information for their characterization and comparison.

When graphical representations of DNA and proteins become too complex because of 3+ dimensional vectors, informational reprocessing has to take a different form. Beside the distance matrices presented earlier, assigning a vector to each of the 20 natural amino acids in the 20D distance matrix it will give the possibility of 20 equivalent directions (Table 2) to be exploited in the forms of walks in space (Table 3) and to construct the protein profile's (Figure 8) [70]. The same method can also be applied for nucleotides.

Table 2: Vector coordinates for the 20 natural amino acids, after [70]

1	**Ala**	**A**	00000000000000000000 1
2	**Arg**	**R**	00000000000000000000 10
3	**Asn**	**N**	00000000000000000000 100
4	**Asp**	**D**	00000000000000000000 1000
5	**Cys**	**C**	00000000000000000000 10000
6	**Gin**	**Q**	00000000000000000000 100000
7	**Glu**	**E**	00000000000000000000 1000000
8	**Gly**	**G**	00000000000000000000 10000000
9	**His**	**H**	00000000000000000000 100000000
10	**lie**	**I**	00000000000000000000 1000000000
11	**Leu**	**L**	00000000000000000000 10000000000
12	**Lys**	**K**	00000000000000000000 100000000000
13	**Met**	**M**	00000000000000000000 1000000000000
14	**Phe**	**F**	00000000000000000000 10000000000000
15	**Pro**	**P**	00000000000000000000 100000000000000
16	**Ser**	**S**	00000000000000000000 1000000000000000
17	**Thr**	**T**	00000000000000000000 10000000000000000
18	**Trp**	**W**	00000000000000000000 100000000000000000
19	**Tyr**	**Y**	00000000000000000000 1000000000000000000
20	**Val**	**V**	00000000000000000000 10000000000000000000

These vectors form the 20D path which is populated by the amino acids in the protein sequence. The path or walk, as the author calls it [70], is a cumulating process of all steps taken along the protein.

For the sequence: MMYALFLLSVGLVMGFVGFSLS we calculate the end path: 31002033040030000001, but to obtain a clear array, all the points along its path have to be plotted. From the arrays' path other eigenvalues can be extracted, such as: the frequency (f_x), the increment number ($i=f_x+ f_{x-1}$), the sum (s) of "I" and the distance ($s^{1/2}$) of each amino acid (Table 3).

Table 3: The path in 20D space of the first 20 amino acids for the human ND6 protein, adapted from Randić [59]

n	AA	Coordinates	f	i	s	distance
1	**M**	0 0 0 0 0 0 0 0 1 0 0 0 0 0 0 0 0 0 0 0 0 0	1	1	1	1
2	**M**	0 0 0 0 0 0 0 0 2 0 0 0 0 0 0 0 0 0 0 0 0 0	2	3	4	2
3	**Y**	0 1 0 0 0 0 0 0 2 0 0 0 0 0 0 0 0 0 0 0 0 0	1	1	5	2.236068
4	**A**	0 1 0 0 0 0 0 0 2 0 0 0 0 0 0 0 0 0 0 0 0 1	1	1	6	2.44949
5	**L**	0 1 0 0 0 0 0 0 2 0 1 0 0 0 0 0 0 0 0 0 0 1	1	1	7	2.645751
6	**F**	0 1 0 0 0 0 0 1 2 0 1 0 0 0 0 0 0 0 0 0 0 1	1	1	8	2.828427
7	**L**	0 1 0 0 0 0 0 1 2 0 2 0 0 0 0 0 0 0 0 0 0 1	2	3	11	3.316625
8	**L**	0 1 0 0 0 0 0 1 2 0 3 0 0 0 0 0 0 0 0 0 0 1	3	5	16	4
9	**S**	0 1 0 0 1 0 1 2 0 3 0 0 0 0 0 0 0 0 0 0 0 1	1	1	17	4.123106
10	**V**	1 1 0 0 1 0 1 2 0 3 0 0 0 0 0 0 0 0 0 0 0 1	1	1	18	4.242641
11	**G**	1 1 0 0 1 0 1 2 0 3 0 0 1 0 0 0 0 0 0 0 0 1	1	1	19	4.358899
12	**L**	1 1 0 0 1 0 1 2 0 4 0 0 1 0 0 0 0 0 0 0 0 1	4	7	26	5.09902
13	**V**	2 1 0 0 1 0 1 2 0 4 0 0 1 0 0 0 0 0 0 0 0 1	2	3	29	5.385165
14	**M**	2 1 0 0 1 0 1 3 0 4 0 0 1 0 0 0 0 0 0 0 0 1	3	5	34	5.830952
15	**G**	2 1 0 0 1 0 1 3 0 4 0 0 2 0 0 0 0 0 0 0 0 1	2	3	37	6.082763
16	**F**	2 1 0 0 1 0 2 3 0 4 0 0 2 0 0 0 0 0 0 0 0 1	2	3	40	6.324555
17	**V**	3 1 0 0 1 0 2 3 0 4 0 0 2 0 0 0 0 0 0 0 0 1	3	5	45	6.708204
18	**G**	3 1 0 0 1 0 2 3 0 4 0 0 3 0 0 0 0 0 0 0 0 1	3	5	50	7.071068
19	**F**	3 1 0 0 1 0 3 3 0 4 0 0 3 0 0 0 0 0 0 0 0 1	3	5	55	7.416198
20	**S**	3 1 0 0 2 0 3 3 0 4 0 0 3 0 0 0 0 0 0 0 0 1	2	3	58	7.615773

From these acquired eigenvalues, the increment number "i" can be used for obtaining the proteins profile [70] (Figure 8) according to Eq. (10).

$$\frac{\sum i^n}{n!} \tag{10}$$

The protein profile offers visual comparison yet comes with loss of information. By assigning integer coordinates to the four nucleotides, we obtain a path which is the lattice representation of the sequence (Figure 9) [71].

The sequence can be represented as a 2D or 3D figure by using 2 (A:+1, -2; T:+2, -1; G:+2, +1; C:+1, +2) or 3 coordinates, however the 2D lattice representation is suited for rapid and easy comparison of genetic material [72]. The transition from nucleotides to amino acids is easily done by increasing the range of x, y coordinates, and ordered by their natural abundance [63] (Figure 10 and Figure 11). The lattice is a highly reduced and simple representation compared to the D/D matrix, but contains sufficient visible information for a fast preliminary comparison of genetic material; this is also achieved without loss of information. For a faster preliminary analysis, one can reduce the lattice only by counting by a set number of steps and skipping the rest, thus obtaining reduced zigzag curves [62].

Figure 8: Protein profile the first 20 amino acids for the human ND6 protein, adapted from Randić [59]; see text for details

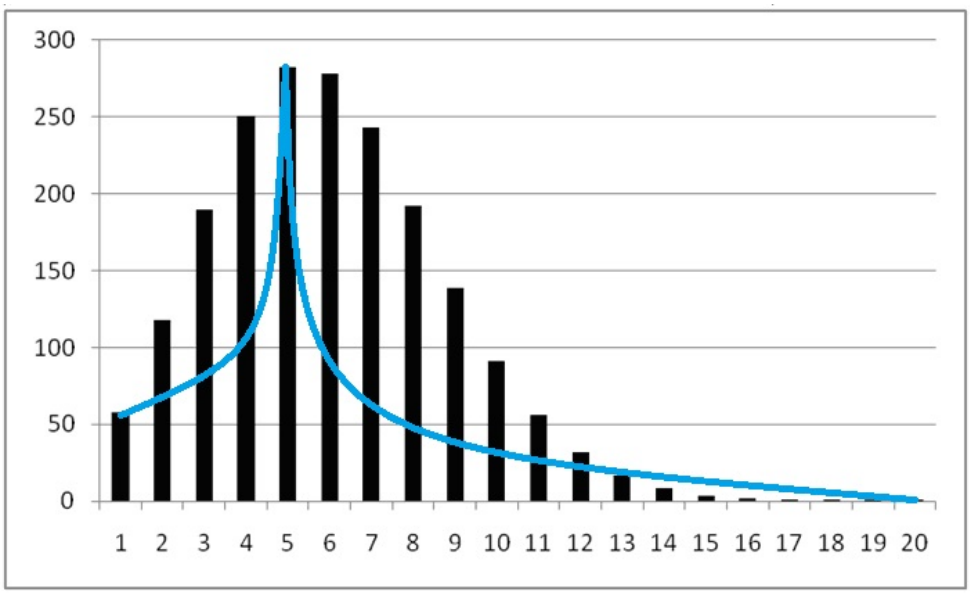

Figure 9: Lattice representation of the hypothetical RNA of the first 30 amino acids for the human ND6 protein, adapted from Randić [59]; see text for details

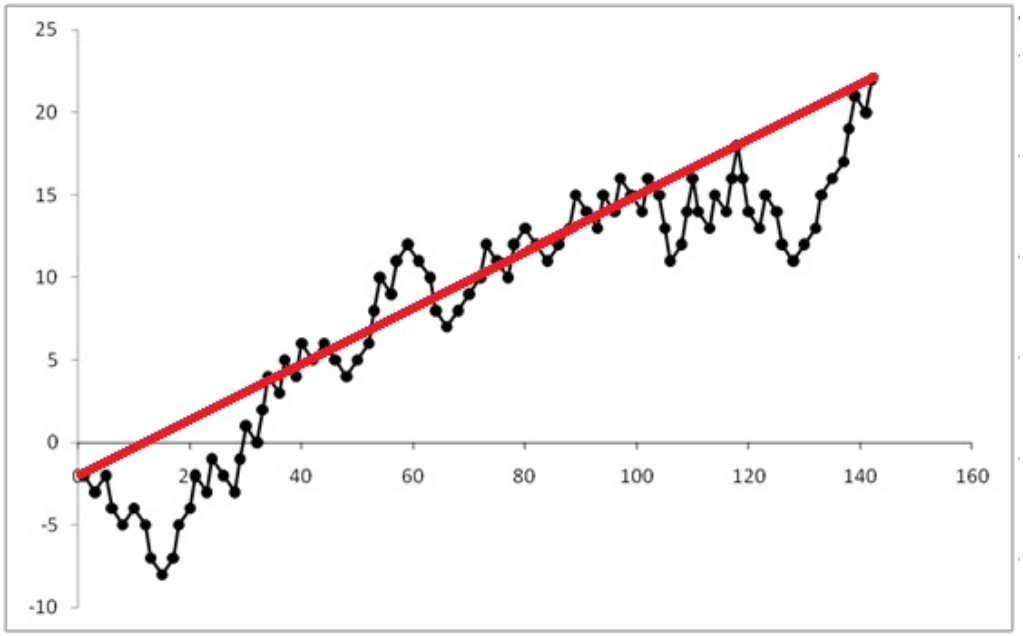

A different type of lattice representation involves constructing a 20X20 distance matrix from the average coordinates of each amino acid. Although this approach offers us a more

facile visual effect, it comes with the cost of information loss and requires supplementary processing [63].

Figure 10: Anticlockwise arrangement of the 20 amino acids in decreasing order of their abundance within proteins, adapted from Randić [63]; see text for details

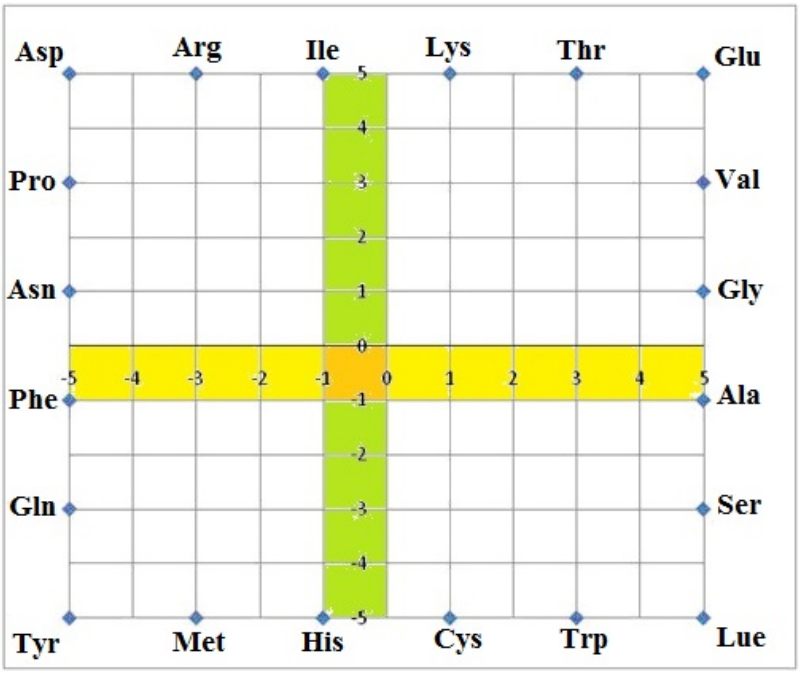

Figure 11: Lattice representation for the human ND6 protein, adapted from Randić [59]; see text for details

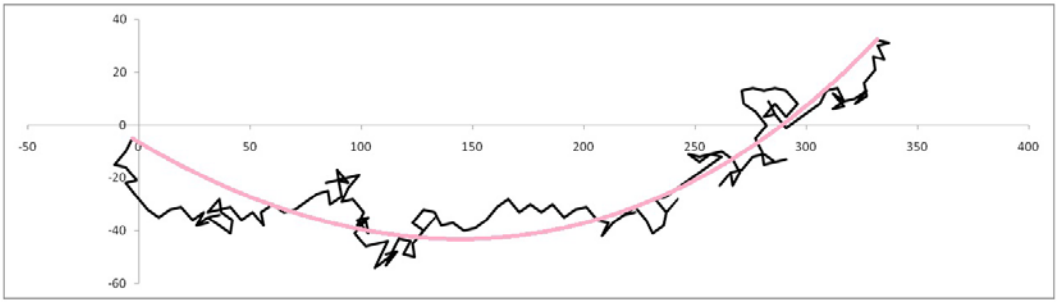

Finally, worth mentioning the *proteomic maps* offering the necessary information on pathological processes and drug pathways; they can be obtained by separating proteins depending on their isoelectric charge and molecular mass, using electrophoresis and gel chromatography of cellular proteins as constant x, y maps. The maps of the same organ cell differ only in the abundance of the proteins [73].

Proteomic maps are processed as bubble diagrams or as tables, for later reprocessing as:

- zigzag curves, by connecting proteins in order of their abundance [73];
- graph ordering, by constructing a mass to charge Cartesian system, in which all connections have a positive slope and there are no intermediate connections [74];
- graph clustering and assigning a third coordinate z as the size of the spot [75];
- nearest-neighbor adjacency graph in which each selected protein connects to its nearest *n* neighbors [76];
- Voronoi adjacency graph, which represents the area of points nearest to the protein [77].

4. CONCLUSION

The importance of topological modeling of proteins is distinguished, as it presents simplified visual characteristics for the rapid and efficient modeling and comparison of protein structures. Even though graphical representations of proteins do not faithfully reproduce reality, they are a valuable tool for quick comparison of similarities and differences of genetic material.

As one would expect, in order to correctly identify the similarities of two biological sequences, a single representation or alignment is not enough and that is why it is necessary to compare and supplement one graphical representation or numerical characterization with another.

Current literature offers many possibilities for the graphical representation of genetic material, but it has not succeeded to provide an answer for the construction of DNA so far. That is why the aim of the authors is to pursue this query in future research.

REFERENCES

1. Alexanderson G.L. Euler and Konigsberg's bridges: A historical view. *American Mathematical Society* **2006**, *43*, 567–573.
2. Harary F. *Graph Theory*; Addison-Wesley Publishing Company; 1969.
3. Bárány I. Applications of Graph and Hypergraph Theory in Geometry. *Combinatorial and Computational Geometry* **2005**, *52*, 31-50.
4. Erdös P.; Meir A.; Sós V.T.; Turán P. On some applications of graph theory, I. *Discrete Mathematics* **2006**, *306*, 853-866.
5. Heckmann T.; Schwanghart W.; Phillips J.D. Graph theory — recent developments of its application in geomorphology. *Geomorphology* **2014**.
6. Cvetković D. Applications of Graph Spectra: an Introduction to the Literature. *Zbornik Radova* **2009**, 7-32.
7. Balaban A.T. Applications of graph theory in chemistry. *Journal of Chemical Information and Computer Sciences* **1985**, *25*, 334-343.
8. Hamori E. Novel DNA sequence representations [7]. *Nature* **1985**, *314*, 585.
9. Randić M. Graphical representations of DNA as 2-D map. *Chemical Physics Letters* **2004**, *386*, 468-471.
10. Diestel R. *Graph theory*; Springer-Verlag; 2000.
11. Bender E.A.; Williamson S.G. *Lists, Decisions and Graphs*; University of California: San Diego; 2010.

12. Heilbronner E. Huckel molecular orbitals of Mobius-type conformations of annulenes. *Tetrahedron Letters* **1964**, 1923-1928.
13. Putz M.; De Corato M.; Benedek G.; Sedlar J.; Graovac A.; Ori O. Topological Invariants of Möbius-Like Graphenic Nanostructures. In *Topological Modelling of Nanostructures and Extended Systems*; Ashrafi A.R., Cataldo F., Iranmanesh A., Ori O., eds.; Springer Netherlands; 2013; 7 7, pp. 229-244.
14. Ajami D.; Oeckler O.; Simon A.; Herges R. Synthesis of a Mobius aromatic hydrocarbon. *Nature* **2003**, *426*, 819-821.
15. Ivanciuc O.; Balaban A.T. *Graph Theory in Chemistry*; John Wiley & Sons; 1998.
16. Janezic D.; Lucic B.; Milicevic A.; Nikolic S.; Trinajstic N.; Vukicevicd D. Hosoya Matrices as the Numerical Realization of Graphical Matrices and Derived Structural Descriptors. *Croatica Chemica Acta* **2007**, *80*, 271-276.
17. Hosoya H. The Topological Index Z Before and After 1971. *Internet Electronic Journal of Molecular Design* **2002**, *1*, 428–442.
18. Shirinivas S.G.; Vetrivel S.; Elango N.M. Applications of graph theory in computer science an overview. *International Journal of Engineering Science and Technology* **2010**, *2*, 4610-4621.
19. Broder A.; Kumar R.; Maghoul F.; Raghavan P.; Rajagopalan S.; Stata R.; Tomkins A.; Wiener J. Graph structure in the Web. *Computer Networks: The International Journal of Computer and Telecommunications Networking* **2000**, *33*, 309-320.
20. Sykes M.F.; Essam J.W.; Heap B.R.; Hiley B.J. Lattice constant systems and graph theory. *Journal of Mathematical Physics* **1966**, *7*, 1557-1572.
21. Chui Y.H.; Rees R.J.; Snook I.K.; O'Malley B.; Russo S.P. Topological characterization of crystallization of gold nanoclusters. *Journal of Chemical Physics* **2006**, *125*.
22. Brouwer D.H. Structure solution of network materials by solid-state NMR without knowledge of the crystallographic space group. *Solid State Nuclear Magnetic Resonance* **2013**, *51-52*, 37-45.
23. Martineau C.; Senker J.; Taulelle F. NMR Crystallography. *Annual Reports on NMR Spectroscopy* **2014**, *82*, 1-57.
24. Gutman I.; Trinajstić N. Graph theory and molecular orbitals. XV. The Hückel rule. *The Journal of Chemical Physics* **1976**, *64*, 4921-4925.
25. Mu L.; Feng C. Topological research on molar diamagnetic susceptibilities for inorganic compounds. *MATCH Communications in Mathematical and in Computer Chemistry* **2007**, *58*, 591-607.
26. Basak S.C.; Grumvald G.D.; Niemi G.J. Use of Graph-Theoretic and Geometrical Molecular Descriptors in Structure-Activity Relationships. In *From Chemical Topology to Three-Dimensional Geometry*; Balaban A.T., ed.; Kluwer Academic Publishers: Hingham, MA, USA; 1997, pp. 73-116.
27. Bonchev D.; Trinajstić N. Information theory, distance matrix, and molecular branching. *The Journal of Chemical Physics* **1977**, *67*, 4517-4533.
28. Estrada E. Atom–bond connectivity and the energetic of branched alkanes. *Chemical Physics Letters* **2008**, *463*, 422-425.
29. Elk S.B. Graph theoretical algorithm to canonically name the isomers of the regular polyhedranes. *Journal of Chemical Information and Computer Sciences* **1992**, *32*, 14-22.
30. Balasubramanian K. Combinatorics of cluster enumeration. *Journal of Chemical Information and Computer Sciences* **1992**, *32*, 47-54.

31. Rappoport D.; Galvin C.J.; Zubarev D.Y.; Aspuru-Guzik A. Complex Chemical Reaction Networks from Heuristics-Aided Quantum Chemistry. *Journal of Chemical Theory and Computation* **2014**, *10*, 897-907.
32. Randić M. Representation of molecular graphs by basic graphs. *Journal of Chemical Information and Computer Sciences* **1992**, *32*, 57-69.
33. Randic M.; Razineer M. On Characterization of 3D Molecular Structure. In *From Chemical Topology to Three-Dimensional Geometry*; Balaban A.T., ed.; Kluwer Academic Publishers: Hingham, MA, USA; 1997, pp. 157-236.
34. Skvortsova M.I.; Baskin I.I.; Stankevich I.V.; Palyulin V.A.; Zefirov N.S. Molecular Similarity. 1. Analytical Description of the Set of Graph Similarity Measures. *Journal of Chemical Information and Computer Sciences* **1998**, *38*, 785-790.
35. Ori O.; Cataldo F.; Graovac A. Topological Ranking of C28 Fullerenes Reactivity. *Fullerenes, Nanotubes and Carbon Nanostructures* **2009**, *17*, 308-323.
36. Iranmanesh A.; Ashrafi A.R.; Graovac A.; Cataldo F.; Ori5 O. Wiener Index Role in Topological Modeling of Hexagonal Systems – From Fullerenes to Graphene. In *Mathematical chemistry monographs*; Gutman I., Furtula B., eds.; University of Kragujevac and Faculty of Science Kragujevac: Kragujevac; 2012, pp. 135–155.
37. Vincent C.; Macleod B. An application of network theory to migration analysis. *Canadian Studies in Population* **1974**, *1*, 43.
38. McGuffin M.J.; Balakrishnan R. Interactive Visualization of Genealogical Graphs. Proceedings of *Proceedings of IEEE Symposium on Information Visualization (InfoVis 2005),* Minneapolis, Minnesota, USA, Andrews K. ed., 2005, 17-24.
39. Kier L.B.; Hall L.H. Intermolecular Accessibility: The Meaning of Molecular Connectivity. *Journal of Chemical Information and Computer Sciences* **2000**, *40*, 792-795.
40. Herndon W.; Chen H.-T.; Zhang Y.; Rum G. QSAR Study of PAH Carcinogenic Activities: Test of a General Model for Molecular Similarity Analysis. In *Molecular Modeling and Prediction of Bioactivity*; Gundertofte K., Jørgensen F., eds.; Springer US; 2000, pp. 47-52.
41. Putz M.V.; Ori O.; Cataldo F.; Putz A.-M. Parabolic Reactivity "Coloring" Molecular Topology: Application to Carcinogenic PAHs. *Current Organic Chemistry* **2013**, *17*, 2816-2830.
42. Buzsáki G. *Rhythms of the Brain*; Oxford University Press; 2009.
43. Girvan M.; Newman M.E.J. Community structure in social and biological networks. *Proceedings of the National Academy of Sciences of the United States of America* **2002**, *99*, 7821-7826.
44. Barthélemy M. Betweenness centrality in large complex networks. *European Physical Journal B* **2004**, *38*, 163-168.
45. Salvador R.; Suckling J.; Coleman M.R.; Pickard J.D.; Menon D.; Bullmore E. Neurophysiological architecture of functional magnetic resonance images of human brain. *Cerebral Cortex* **2005**, *15*, 1332-2342.
46. Gong G.; He Y.; Concha L.; Lebel C.; Gross D.W.; Evans A.C.; Beaulieu C. Mapping anatomical connectivity patterns of human cerebral cortex using in vivo diffusion tensor imaging tractography. *Cereb Cortex* **2009**, *19*, 524-536.
47. Stam C.J.; Van Dijk B.W. Synchronization likelihood: An unbiased measure of generalized synchronization in multivariate data sets. *Physica D: Nonlinear Phenomena* **2002**, *163*, 236-251.
48. Ravasz E.; Barabási A.L. Hierarchical organization in complex networks. *Physical Review E - Statistical, Nonlinear, and Soft Matter Physics* **2003**, *67*, 261121-261127.

49. Amaral L.A.N.; Scala A.; Barthélémy M.; Stanley H.E. Classes of small-world networks. *Proceedings of the National Academy of Sciences of the United States of America* **2000**, *97*, 11149-11152.
50. Freeman L. A Set of Measures of Centrality Based on Betweenness. *Sociometry* **1977**, *40*, 35-41.
51. Carrillo-Reid L.; Hernandez-Lopez S.; Tapia D.; Galarraga E.; Bargas J. Dopaminergic modulation of the striatal microcircuit: receptor-specific configuration of cell assemblies. *J Neurosci* **2011**, *31*, 14972-14983.
52. Ray S.; Miller M.; Karalunas S.; Robertson C.; Grayson D.S.; Cary R.P.; Hawkey E.; Painter J.G.; Kriz D.; Fombonne E.; Nigg J.T.; Fair D.A. Structural and functional connectivity of the human brain in autism spectrum disorders and attention-deficit/hyperactivity disorder: A rich club-organization study. *Hum Brain Mapp* **2014**, *35*, 6032-6048.
53. Bassett D.S.; Bullmore E.; Verchinski B.A.; Mattay V.S.; Weinberger D.R.; Meyer-Lindenberg A. Hierarchical organization of human cortical networks in health and Schizophrenia. *Journal of Neuroscience* **2008**, *28*, 9239-9248.
54. Catani M.; Ffytche D.H. The rises and falls of disconnection syndromes. *Brain* **2005**, *128*, 2224-2239.
55. Bullmore E.; Sporns O. Complex brain networks: graph theoretical analysis of structural and functional systems. *Nat Rev Neurosci* **2009**, *10*, 186-198.
56. Randić M. 2-D graphical representation of proteins based on virtual genetic code. *SAR QSAR Environ Res* **2004**, *15*, 147-157.
57. Guo X.; Nandy A. Numerical characterization of DNA sequences in a 2-D graphical representation scheme of low degeneracy. *Chemical Physics Letters* **2003**, *369*, 361-366.
58. Randić M. Graphical representations of DNA as 2-D map. *Chemical Physics Letters* **2004**, *386*, 468-471.
59. Randić M.; Vračko M.; Plavšić D. Novel Graphical Representation of Proteins Based on the Virtual Genetic Code. *International Journal of Chemical Modeling* **2009**, *1*, 305-324.
60. Randić M.; Vračko M.; Nandy A.; Basak S.C. On 3-D graphical representation of DNA primary sequences and their numerical characterization. *Journal of Chemical Information and Computer Sciences* **2000**, *40*, 1235-1244.
61. Randić M.; Kleiner A.F.; DeAlba L.M. Distance/distance matrices. *Journal of Chemical Information and Computer Sciences* **1994**, *34*, 277-286.
62. Randić M.; Zupan J.; Balaban A.T.; Vikic-Topic D.; Plavšić D. Graphical representation of proteins. *Chem Rev* **2011**, *111*, 790-862.
63. Randić M.; Vračko M.; Nović M.; Plavšić D. 20. On uniform representation of proteins by distance matrix. In *Quantum Frontiers of Atoms and Molecules*; Putz M.V., ed.; Nova Science Publishers: New York; 2011, pp. 673.
64. Randić M.; Novič M.; Vračko M. On novel representation of proteins based on amino acid adjacency matrix. *SAR QSAR Environ Res* **2008**, *19*, 339-349.
65. Randić M.; Vračko M.; Lerš N.; Plavšić D. Novel 2-D graphical representation of DNA sequences and their numerical characterization. *Chemical Physics Letters* **2003**, *368*, 1-6.
66. Randić M.; Vračko M.; Lerš N.; Plavšić D. Analysis of similarity/dissimilarity of DNA sequences based on novel 2-D graphical representation. *Chemical Physics Letters* **2003**, *371*, 202-207.

67. Liao B.; Chen W.; Sun X.; Zhu W. A binary coding method of RNA secondary structure and its application. *Journal of Computational Chemistry* **2009**, *30*, 2205-2212.
68. Jeffrey H.J. Chaos game representation of gene structure. *Nucleic Acids Research* **1990**, *18*, 2163-2170.
69. Barnsley M.F. Chapter IX Measures on Fractals In *Fractals Everywhere*, 2nd ed ed.; Academic Press: Boston, MA; 1988.
70. Nović M.; Randić M. Representation of proteins as walks in 20-D space. *SAR QSAR Environ Res* **2008**, *19*, 317-337.
71. Hamori E.; Ruskin J. H curves, a novel method of representation of nucleotide series especially suited for long DNA sequences. *Journal of Biological Chemistry* **1983**, *258*, 1318-1327.
72. Nandy A. A new graphical representation and analysis of DNA sequence structure: I. Methodology and application to globin genes. *Current Science* **1994**, *66*, 309.
73. Randić M. On Graphical and Numerical Characterization of Proteomics Maps. *Journal of Chemical Information and Computer Sciences* **2001**, *41*, 1330-1338.
74. Randić M.; Zupan J.; Novič M. On 3-D Graphical Representation of Proteomics Maps and Their Numerical Characterization. *Journal of Chemical Information and Computer Sciences* **2001**, *41*, 1339-1344.
75. Bajzer Ž.; Randić M.; Plavšić D.; Basak S.C. Novel map descriptors for characterization of toxic effects in proteomics maps. *Journal of Molecular Graphics and Modelling* **2003**, *22*, 1-9.
76. Randić M.; Lerš N.; Plavšić D.; Basak S.C. On invariants of a 2-D proteome map derived from neighborhood graphs. *Journal of Proteome Research* **2004**, *3*, 778-785.
77. Randić M.; Novič M.; Vračko M.; Plavšić D. Study of proteome maps using partial ordering. *Journal of Theoretical Biology* **2010**, *266*, 21-28.

NEW FRONT. CHEM. (**2014**)
Volume 23, Number 1, pp. 39-52
ISSN 2393-2171; ISSN-L 2393-2171

Former: Ann. West Univ. Timisoara – Series Chem.
ISSN: 1224-9513

Article

SYNTHESIS, STRUCTURE AND MAGNETIC PROPERTIES OF NEW HOMOPOLYNUCLEAR MANGANESE(II) CHAIN COMPLEX

Marilena Ferbinteanu [♣]
University of Bucharest, Faculty of Chemistry, Inorganic Chemistry Department, Dumbrava Rosie 23, Bucharest 020462, Romania

ABSTRACT

A 1D-manganese chain complex was synthesized by self-assembling strategy using a paramagnetic building block, [Mn(bpca)$_2$], based on the ditopic ligand, Hbpca=bis-(2-pyridilcarbonyl)-amine. The chain consists in the alternation of {MnN_6} chromophores, with axial compression oriented parallel to the chain direction, and {MnO_6}units, with axial elongation perpendicular to the 1-D line. The {MnO_6} species are containing aqua-Mn(II)-perchlorate polar axes imposing a dipole of the chain, perpendicular to its extending direction. Dipole-dipole, dipole-charge and hydrogen bonding are contributing to the supramolecular cohesion. A weak antiferromagnetism, due to superexchange via π-system of bpca bridges is fitted to the J=-0.293 cm^{-1} value of coupling strength.

Keywords: ditopic ligand, self-assembling synthesis, manganese chain complexes, magnetic coupling.

1. INTRODUCTION

Coordination chemistry [1] is a central realm in the nowadays world of sciences oriented toward the achievement of new materials and technologies. The bonding mechanism in complex compounds [2] and the relation structure-properties are quite similar to those existing in solid state systems with recognized applicability such as magnetic or superconductor oxides. However, since at the molecular scale the recognition of causal

♣ Correspondent author: E-mail: marilena.cimpoesu@g.unibuc.ro

factors producing a desired property is clearer than in the infinity of solid state, the coordination compounds offer various particularized case studies to get academic insight with possible ultimate relevance in property design. Besides, the size of coordination edifices can be tuned to progressive larger scale, e.g. from distinct molecules (0-D) to the 1-D, 2-D or bulk 3-D connection patterns of metal ions with the ligands [3]. Large molecular complexes, constituted by tens of metal ion centers, bridged by ligands (medium sized organic molecules, in the range of few tens of atoms) are approaching the nano-scale [4-5]. Extended coordination systems such as metal-organic frameworks are in the full focus possible applications in various areas, for instance in catalysis [6].

A central idea in the modern coordination sciences, in connection with the paradigms of supra-molecular chemistry [7-8], is that the specifics of each ligand, the topology of donors and propensity for non-covalent interactions, in conjuncture with the affinity or stereochemical match of the metal ions to the ligand active sites, can be handled to the purpose of rationally controlled complex structures. Although countless examples in the line of such desiderata are reported in the literature, the complete control of structure and properties is still at the learning curve. This makes the coordination paradigm a quite active and yet dynamic one. Particularly, the molecular magnetism [9-11] is a prominent domain of the coordination chemistry, with its speculative end in the yet elusive spintronics, but with a lot of significant solid conquests on academic ground, in the area of magneto-structural correlations, as pieces of knowledge paving the road to new high-tech devices and useful effects [12]. The vogue of the last years was devoted to special issue of magnetic anisotropy [13-16], a very essential ingredient for achieving a magnet at molecular scale, the so-called Single Molecule Magnets (SMMs) [17-18]. In this context, the coordination polymeric structures, designed - in principle- with specific properties as function of composition and topologies are interesting for achieving 1-D anisotropic systems with Single Chain Magnet (SCMs) behaviour [19].

We contributed with illuminating case studies to such issues, with one of the first small sized SMMs (d-f dinuclear) [22], one of the firsts SCMs [20], as well as several related advances [16, 22-26]. A part of these previously discussed magnetic systems were based on $[M^{q}(bpca)_2]^{q-2}$ coordinative donor building blocks, with the ditopic ligand Hbpca=bis-(2-pyridilcarbonyl)-amine, its ionized form ($bpca^-$) represented in Scheme 1. The ligand is planar, potentially pentadentate, acting as a divergent connector with three nitrogen donor atoms oriented in one direction and a two-oxygen chelate on opposite side.

The ligand is known since long time, but we pioneered its use in the d-f assembling strategies [22]. The Hbpca is obtained by reacting 1,3,5-tris(2-pyridyl)triazine with copper sulfate, the free organic ligand being isolated from the formed copper (II) complex by EDTA extraction [21]. The two coordination sites can select metal ions with different chemical affinities, for instance the nitrogen side for approaching d-transition metal ions, while the diketonato-type chelate moiety is suitable for oxofile lanthanide ions. Therefore, the anionic bpca− is particularly suited for assembling d−f systems and we exploited [22-26] its propensity to build oligomeric or chain d−f systems [27]. Aside to the new synthetic aspects, we complemented our magneto-structural insight with ab initio original approaches, designed for particularities of f systems, including Spin Orbit (SO), Ligand Field (LF) and exchange coupling terms [22]. Other synthesized d-f systems became study cases for another breakthrough of our group, the analysis of the magnetic anisotropy by polar map

representations which allow to identify the easy magnetization axes respect with the molecular frame [24, 26].

Scheme 1: Coordination modes of the bpca ligand illustrating divergent tridentate function through nitrogen atoms and bidentate function through the oxygen ones.

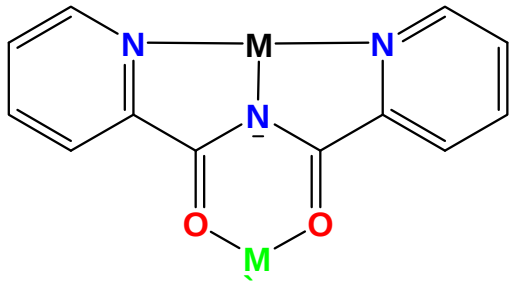

Mononuclear complex $[M^q(bpca)_2]^{q-2}$ (q=2, 3) units are known for several transition metal ions like Mn(II) [28], Fe(II, III) [29-33], Co(III) [34-36], Rh(II, III) [37-39], Ni(II) [30], Cu(II) [21], Zn(II) [21]. The $[M^q(bpca)_2]^{q-2}$ units are building blocks, acting as complex ligand, in producing d-d discrete structures [35, 40-42], homo- or heteropolynuclear systems with 1-D [31,35,43-46], 2-D [41,45] or extended structures with the same or different transition metal ions. Among these compounds an unique d-d SCM was reported to have a twisted arrangement of ions with alternate orientation easy-plane magnetic anisotropy [43] accompanied by valuable studies concerning the magnetic properties [46, 47].

A $[M^q(bpca)_2]^{q-2}$ buiding block not exploited until now in the polynuclear chain structures design is based on Mn(II). We report here the case of $[Mn(bpca)_2]$ acting as a complex ligand to form a homonuclear 1-D complex with the {Mn(μ-bpca)Mn(μ-bpca)Mn} sequence. We describe syntheses, structures, and magnetic properties of the new chain.

Implying only Mn(II) ions it has very weak anisotropy, being not directly relevant, in itself for SCM systems, but it is interesting as matter of synthesis and structure. Besides, the manganese ion from at least one of the two coordination spheres can, in principle, be oxidized to Mn(III) state which has strong anisotropic features. Then, the manganese chain complexe could be a possible precursor of a SCM system, if further electrochemical controlled oxidation will be applied, preliminaries in this sense being attempted. Therefore, the present study is a prerequisite for further advances, consolidating structure-property correlation knowledge in the conjuncture of its relatively simple scheme of bonding and spin coupling.

2. METHODS

2.1. Experimental

Synthesis. All chemicals were reagent grade and used as received. The Hbpca and $[Mn(bpca)_2]$ were prepared by the literature methods [28,30]. (*Caution!* Although no problems have been encountered in the present work, perchlorates are potentially explosive and should be treated in small quantities with care).

To a solution of $[Mn(bpca)_2]\cdot H_2O$ (31.75 mg, 0.06 mmol) in CH_3NO_2 (2 mL) was added $Mn(ClO_4)_2\cdot 6H_2O$ (21.71 mg, 0.06 mmol) in CH_3OH (3 mL). The orange reaction mixture was stirred for one hour at room temperature. Orange crystals of (**1**) were obtained in several days by slow evaporation at room temperature and then filtered and dried in the air. Yield: 42 mg (83%).

Elemental Analysis: Calculated for $C_{25}H_{25}Cl_2Mn_2N_7O_{15}$: C, 35.56; H, 2.98; N, 11.61. Found: C, 35.60; H, 3.10; N, 11.50. IR (KBr, cm^{-1}): ν(C=O) 1720, ν(ClO_4^-) 1087, 624.

X-ray Crystallography. The diffraction data were collected on Bruker AXS SMART-1000/CCDD area detector using the standard procedure (Mo Ka radiation). The data integration and reduction were undertaken with SAINT and XPREP [48]. The intensity data were empirically corrected for absorption using the program SADABS [49]. The structures were solved by direct methods and refined using least-squares methods on F^2 with SHELXL-97 [50]. Non-hydrogen atoms were modeled with anisotropic displacement parameters, and hydrogen atoms were placed by difference Fourier syntheses and refined isotropically.
λ(Mo Kα) = 0.71073Å, T = 200 K, orange blocks, formula $C_{25}H_{25}Cl_2Mn_2N_7O_{15}$, MW = 905.33, 0.80 x 0.65 x 0.60 mm, tetragonal, I-4, a = 15.3606(18) Å, b = 15.3606(18) Å, c = 30.433(6) Å, a = 90°, b =90°, c = 90°, Z = 8, V = 7180.7(19) $Å^3$,
R_1 = 0.0828, wR_2 = 0.2142, GOF = 1.036. Selected bond lengths and angles are presented in Table 1 and 2.

Spectral Measurements. Fourier transform infrared spectroscopy on KBr pellets was performed on a JASCO FT/IR-620 instrument.

Magnetic Measurements. Variable-temperature magnetic susceptibility measurements were made by using a SQUID magnetometer MPMS 5S (Quantum Design) at 1 T field. Diamagnetic correction for each sample was determined from Pascal's constants.

3. RESULTS AND DISCUSSIONS

By the reaction of *in situ* formed $[Mn(bpca)_2]$ with excess of Mn(II) ions (added from $Mn(ClO_4)_2\cdot 6H_2O$) a 1-D homopolynuclear $[Mn(\mu\text{-bpca})_2Mn(H_2O)(ClO_4)]ClO_4\cdot CH_3NO_2$ (**1**) compound is collected, as orange crystals. The neutral $[Mn(bpca)_2]$ act as buiding block, through the four outer oxygen atoms of the nitrogen – coordinated bpca- ligands. The formed chain is almost linear with a slight zig-zag tendency. It contains two Mn(II) species, one coordinated by six nitrogen atoms, pre-existent in $[Mn(bpca)_2]$ and a center entirely based on oxygen donors.

The Figure 1 shows the asymmetric unit while the Figure 2 a sequence of two parallel chains in the crystal structure of $[Mn(\mu\text{-bpca})_2Mn(H_2O)(ClO_4)]ClO_4\cdot CH_3NO_2$ (**1**).

Figure 1: Asymmetric units from molecule of Scheme (**1**) including the numbered atoms scheme. The solvent molecules and hydrogen atoms were omitted, for clarity.

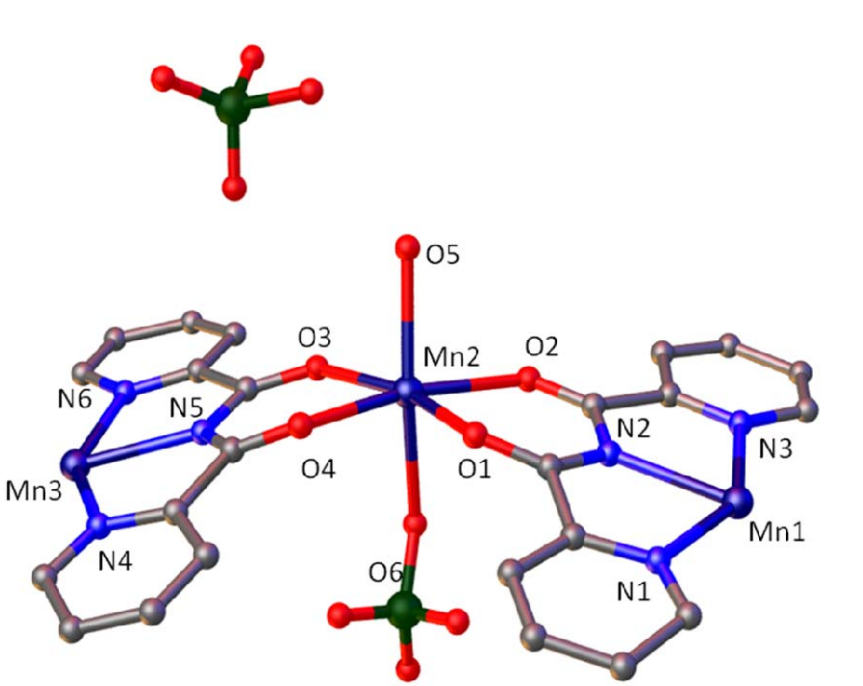

The Figure 2 shows the alternating profile of chain, where Mn2 sites are bridged by the bpca ligands with the Mn1 and Mn3 neighbours. The Mn1-Mn2-Mn3 sequences are slightly angular (with the 150.40^{o} central angle) imposing a zig-zag arrangement with separations of 5.616 Å for Mn1-Mn2 and 5.618 Å for Mn2-Mn3, respectively. The Mn-Mn remote distances are lower than in the linear trinuclear compound previously reported [42]. The Mn2-Mn1-Mn2' and Mn2-Mn3-Mn2' sequences are almost linear.

The nitrogen-based coordination spheres of Mn1 and Mn3 sites are closely similar, but yet slightly different, probably because of the dynamic disordering induced by the perchlorate (coordinated and free) ions. These [Mn(bpca)$_2$] units are possessing C_2 symmetry operations, with axes placed between the two ligands of each coordination fragment, perpendicularly to the main direction of the chain. The tridentate nitrogen side of the bpca ligands contains two pyridine functions and a central amide, imposing a meridial arrangement of the donors in octahedron. The geometries of Mn1 and Mn3 coordination units are compressed octahedra with the short bonds on the N_{amide}-Mn-N_{amide} direction. This is a characteristic of all the [M(bpca)$_2$] units, but in general rare for the manganese complexes. The four pyridine nitrogens can be taken as equatorial planes of the Mn1 and Mn3 units. For Mn1, the equatorial Mn1–N distances are 2.230(10) and 2.258(11) Å the short axial contacts with the two amide nitrogens (N2) with distances of 2.169(8) Å (see Table 2), each value repeated twice due to the two-fold axis.

Table 1: Selected bond distances (Å) and angles (°) for molecule of Scheme (**1**)

Mn-N		Mn-O		E-Mn-E	
Mn1-N1:	2.230(10)	Mn2-O1:	2.119(7)	N2-Mn1-N1:	74.4(3)
Mn1- N2:	2.169(8)	Mn2-O2:	2.130(7)	N2-Mn1-N3:	73.8(4)
Mn1- N3:	2.258(11)	Mn2-O3:	2.145(7)	N5-Mn3-N4:	74.1(3)
Mn3-N4:	2.227(10)	Mn2-O4:	2.122(7)	N5-Mn3-N6:	73.2(4)
Mn3- N5:	2.185(8)	Mn2-O5:	2.204(7)	O1-Mn2-O2:	81.7(3)
Mn3- N6:	2.261(11)	Mn2-O6:	2.245(9)	O1-Mn2-O5:	96.0(3)

The equivalent bonds, under the C_2 symmetry, are mutually placed in *cis* for the pyridine members of the mean equatorial plane and in *trans* in the case of the axial imides. The formal equatorial plane looks, in fact, like a flattened tetrahedron, the *trans* points making a 147.2 degrees with respect of the central metal ion. The octahedron frame is quite distorted, due to specific constrains of the bpca skeleton, having angles about the 74 degrees in the *cis* sequences between pyridine and amide donors of the same ligand. Similarly, Mn3 is surrounded by four pyridyl nitrogens (N4, N6) with 2.227(10)-2.261(11) Å bond lengths and two amide nitrogens (N5) with distances of 2.185(8) Å, the showing the same qualitative features described for the Mn1 unit. The pattern of Mn1 and Mn3 fragments is comparable with those in the parent monomeric $[Mn(bpca)_2]$ [28].

The ionized beta-diketonate moieties from two $[Mn(bpca)_2]$ units of Mn1 and Mn3 sites are forming the equatorial plane of the Mn(II) octahedral center labeled Mn2, while its axial positions are occupied by an aqua (H_2O) and one perchlorate (ClO_4^-) ligand. The FT-IR spectrum shows for the perchlorate group an intense and split band around 1087 cm^{-1}, accompanied by a weak band at 624 cm^{-1}, suggesting different perchlorate species, coordinated and free. Slightly higher frequency shift of C=O stretching (an intense band at 1720 cm^{-1} compared with 1700 cm^{-1} for the parent monomer [28]) suggest that the negative charge of the ligand is more localized on the central amide nitrogen atom, while the carbon-oxygen links tend to more double bond character. The oxygen-based coordination unit has the {O1-O2-Mn2-O3-O4 }equatorial plane with a slight pyramidal distortion, the planes of diketonate chelates having the appearance of a hinge opened at a dihedral plane of about 170 degrees. This feature determines the open angular placement of the Mn1-Mn2-Mn3 centers and the zig-zag aspect of the chain. Comparing the bond distances presented in Table 1, the geometry of the central atom appears as an octahedron elongated on the aqua-perchlorate O5-Mn1-O6 direction, with corresponding d(Mn2-O5)=2.204(7) Å and d(Mn2-O6)= 2.245(9) Å distances. This site has no symmetry. The carbon-oxygen bonds are slightly different, in the same ligand or comparing the two ligand species. Thus, for the ligand connecting the Mn2 and Mn1 ions the bond lengths are 1.210(11) and 1.247(12) Å, while 1.217(11) and 1.232(11)

Å for the bpca placed between Mn2 and Mn3 species. Aside the FT-IR data, the C-O distances are suggesting again that the negative charge of the bpca ligand is localized on the central N_{amide} atoms.

The *trans* O5-Mn2-O6 axis, made of aqua and perchlorate ligands, imposes a definite dipole moment to the $\{MnO_6\}$ oxygen based coordination sphere of the Mn2. In Figure 2 the sequence of the chain structure is represented, showing the coordination polyhedra. The chain is positively charged, being counter-balanced by a row of perchlorate anions placed in the neighborhood of the mentioned aqua ligands. Considering the above details, we observe the alternation of $\{MnN_6\}$ octahedra with axial compression parallel to the chain with $\{MnO_6\}$ units with axial elongation perpendicular to the 1-D line. Because of mutual rotation, by about 90 degrees, of the alternating bpca ligands, the H_2O-Mn-ClO_4 vectors from immediately repeated Mn2 units are also rotated in the same way. The next neighbouring units, at the count of Mn2 sites, show parallel orientation of the polar H_2O-Mn-ClO_4 moieties. Thus, if take the mean direction of the chain as *z*, and placing one aqua-Mn2-perchlorate axis on the positive direction of *x*, the vicinal Mn2 site will point its dipole towards *y*, the following one again on *x*, while the further one on *y*, and so on. Then, the whole chain carries a resultant dipole along the axis bisecting the *xy* plane, perpendicular to the *z* one-dimensional extension. The neighbor chain has the mirror image, with alternating H_2O-Mn-ClO_4 dipoles pointing reversely, with the $-x$ and $-y$ alternation. This relationship is visible comparing the parallel chains shown in Figure 2. One may infer the dipole-dipole interaction of the chain as an important mechanism of the supramolecular ordering. There is also a dipole-charge interaction, as well a hydrogen bonding, between the aqua edge of the H_2O-Mn-ClO_4 moiety and the non-coordinated perchlorate (shown in Figure 1, omitted in Figure 2, for a full clarity of the chain image).

Figure 2: Sequence of the zig-zag chain structure of compound of Scheme (**1**) with polyhedral representation for manganese ions coordination sites. Chains with opposite dipole resultants, due to ordered H_2O-Mn-ClO_4 polarized axes, are running parallel.

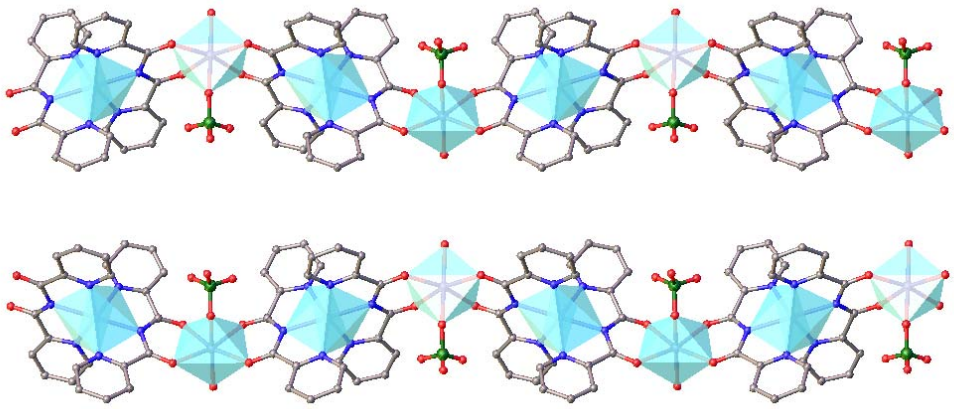

Table 2: Bond distances (Å) around manganese ion in the bridging buiding block in complex of Scheme (**1**) and other literature complex vs. mononuclear complexes $[Mn(bpca)_2]$

$Mn\text{-}N_{amide}$	$Mn\text{-}N_{py}$	$Mn\text{-}N_{amide}$ [a]	$Mn\text{-}N_{py}$ [a]	$Mn\text{-}N_{amide}$ [b]	$Mn\text{-}N_{py}$ [b]
2.185(8)	2.258(11)	2.196(2)	2.246(2)	2.179(7)	2.255(7)
2.169(8)	2.230(10)	2.203(2)	2.221(2)	2.169(7)	2.216(7)
	2.261(11)		2.262(2)		2.285(8)
	2.227(10)		2.242(2)		2.236(8)

[a]Reference [42]. [b] Reference [28].

Looking at larger scale, one observes that, in the crystal, the chains are grouped in layers. Each layer contains a parallel arrangement of different enantiomeric chains, as presented in the packing diagrams from Figure 3.

Figure 3: Packing diagram for the compound of Scheme (**1**) along *a* (a) and *c* (b) axis showing the parallel arrangement of the chains.

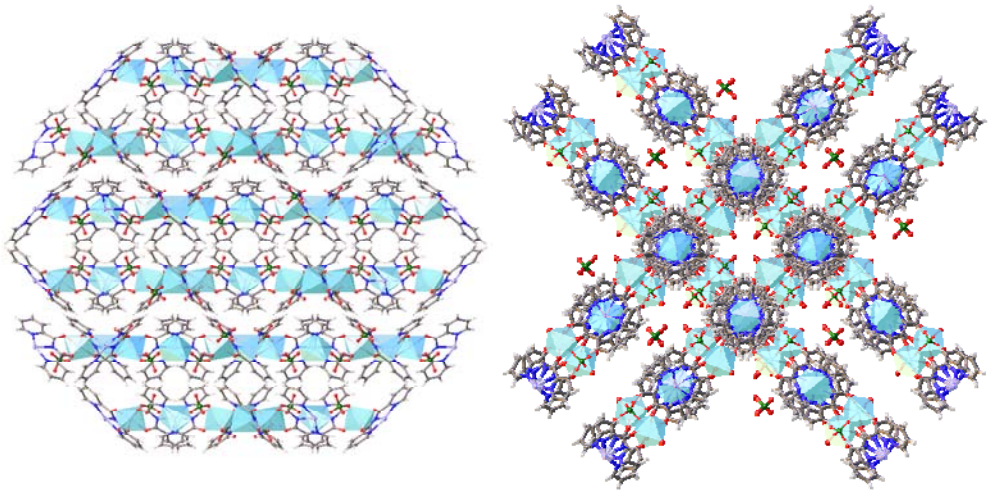

(a) (b)

The Figure 4 shows the temperature dependence of the magnetic susceptibility for (**1**) measured down to 2.0 K. The $\chi_M T$ value at room temperature, 3.5 cm^3 K mol^{-1}, is lower than the spin-only value of 4.4 cm^3 K mol^{-1} for a *S*=2 spin paramagnet with taking the gyromagnetic factor g =2.00, the level of the plateau estimating then g=1.8.

Figure 4: Plot of χT vs. *T* for molecule of Scheme (**1**). The circles correspond to the experimental points and the solid line corresponds to the theoretical curve for which parameters are given in the text.

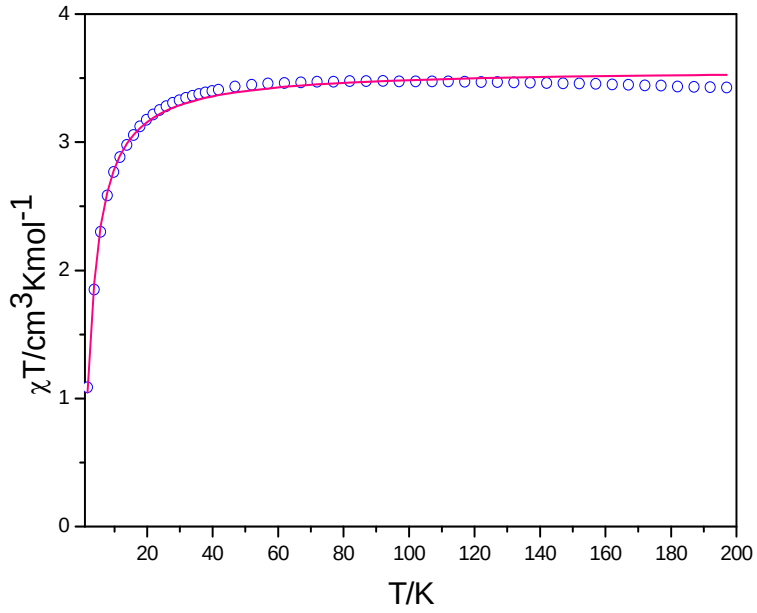

On lowering the temperature, the $\chi_M T$ vs. *T* curve value decreases suggesting antiferromagnetic interaction between adjoining Mn(II) ions through the delocalized π-system of the bridging bpca ligands. In principle, there are two exchange coupling constants, alternating along the chain, between the Mn1-Mn2 and Mn2-Mn3 centers, but given the close structural similarity of the Mn1 and Mn3 species, one may a unique coupling parameter, *J*. The susceptibility was modeled with the Fisher equation [51-52] for an infinite uniform chain:

$$\chi_M = \frac{N\beta^2 g^2 S(S+1)}{3kT} \cdot \frac{1+u}{1-u} \tag{1}$$

$$\text{Where } u = \coth\left[\frac{JS(S+1)}{kT}\right] - \left[\frac{kT}{JS(S+1)}\right] \tag{2}$$

The least squares calculation yielded the best fit parameters of g = 1.807 and J = -0.293 cm^{-1}. The gyromagnetic factor is practically the same with the above estimation from the level of high temperature $\chi_M T$ plateau. The small absolute value of the coupling parameter is reasonable, conceivable as resultant of compensating different positive and negative orbital exchange channels at the d^5-d^5 exchange interaction, with a slight predominance of antiferromagnetic paths, probably due to the bridge-delocalized π-type interactions.

4. CONCLUSION

In this work we treated the synthesis, molecular structure and supramolecular assembling details of the $[Mn(\mu\text{-bpca})_2Mn(H_2O)(ClO_4)]ClO_4 \cdot CH_3NO_2$ compound. The 1-D pattern is due to the bridging capabilities of the bpca ligand. The tridentate nitrogen moiety is a strong coordinating agent, capturing the metal ions (Mn(II) in our case) in the center of an axially compressed octahedron. At the same time, the ligand possesses outer oxygen donors, suited to coordinated hard Lewis acids, such as lanthanide ions, the Mn(II) ion being also fitted to interact with this function. In other words, the $[Mn(bpca)_2]$ units with nitrogen-based coordination sphere act as complex ligands toward another metal ion, the symmetric divergent topology favoring the formation of the chain. The Mn(II) ions connecting the preformed $[Mn(bpca)_2]$ moieties have coordination spheres entirely based on oxygen donors, with two pairs from diketonate functions of the bpca placed equatorially, while one aqua and one perchoarate ligand, placed axially, confer a net dipole to the unit. The coordination polar axes are ordered in such a way that the whole chain has a dipole moment, perpendicular to its growth direction. In the crystal, each chain has an enatiomeric companion (mirror image) with opposed polar structure. The supramolecular dipolar interactions between chains are part of the mechanism of the crystal packing. Besides, dipole-charge interactions are established between polymeric coordination structures (with net positive charge) and rows of interstitial perchlorate anions. The perchlorates are forming also supramolecular hydrogen bond networks with the coordinated aqua axial ligands. Both the nitrogen-based and oxygen-type coordination spheres are visibly distorted from regular octahedron. In the former, there is an axial compression imposed by the structure of the bpca ligand, with pyridine functions forming an equatorial mean plane, which looks like a flattened tetrahedron, while amide donors are forming the short axial bonds. In the other coordination species, the diketonate planes of from different $[Mn(bpca)_2]$ complex ligands are forming a hinge distortion, shaping the zig-zag pattern of the chain. The magnetic susceptibility shows a weak antiferromagnetic coupling along the chain, fitted with Fisher equation to the J = -0.293 cm^{-1} value. This interaction is mediated by the π-type delocalization along the bridge. Consisting in Mn(II) homo-metallic composition, the system has no magnetic anisotropy, but the nitrogen based sites can supposedly be oxidized to Mn(III) with potential single-chain-magnet features, further attempts being invested in this direction.

ACKNOWLEDGEMENT

This work is supported by University of Bucharest grant nr. 329/25.02.2014 and COST action CM1305 (ECOSTBIO).

REFERENCES

1. Lawrance, G. A. *Introduction to Coordination Chemistry*, John Wiley and Sons Ltd.: Newcastle, 2010.
2. Cimpoesu, F.; Zaharia, A.; Stamate, D.; Panait, P.; Oprea, C.I.; Gîrtu, M.A.; Ferbinteanu, M.; New Insights in the Bonding Regime and Ligand Field in Wernerian Complexes. A Density Functional Study. *Polyhedron* **2013**, *52*(22), 183-195.
3. Wöhrle, D.; Pomogailo, A. D. (Eds.) *Metal Complexes and Metals in Macromolecules: Synthesis, Structure and Properties*, Wiley-VCH Verlag GmbH & Co. KGaA: Weinheim, 2003.
4. Klabunde, K. J. (Ed) *Nanoscale Materials in Chemistry*. John Wiley & Sons, Inc.: New York, 2001.
5. Nabok, A. *Organic and Inorganic Nanostructures*, Artech House, Inc.: Norwood, 2005.
6. Ferbinteanu, M.; Cimpoesu, F.; Tanase, S. Metal-Organic Frameworks with d–f Cyanide Bridges: Structural Diversity, Bonding Regime, and Magnetism*, Structure and Bonding* **163**, 2015, pp 185-229.
7. Lehn, J.M. *Supramolecular Chemistry: Concepts and Perspectives*, Wiley-VCH: Weinheim, 1995.
8. Ariga, K.; Kunitake, T. *Supramolecular Chemistry – Fundamentals and Applications*, Springer-Verlag: Berlin, Heidelberg, 2006.
9. Kahn, O. *Molecular Magnetism*, Wiley-VCH: Weinheim, 1993.
10. Coronado, E.; Delhaès, P.; Gatteschi, D.; Miller, J. S. *Molecular Magnetism: From Molecular Assemblies to the Devices*, Springer: Heidelberg, 1996**.**
11. Miller, J. S.; Drillon, M. (eds), *Magnetism: Molecules to Materials*, Wiley-VCH: Weinheim, 2001.
12. Gatteschi, D.; Sessoli, R.; Villain, J. *Molecular Nanomagnets (Mesoscopic Physics and Nanotechnology)*, Oxford University Press: Oxford, 2006.
13. Sessoli, R.; Powell, A. K. Strategies towards single molecule magnets based on lanthanide ions. *Coord. Chem. Rev*. **2009**, 253, 2328– 2341.
14. Cucinotta, G.; Perfetti, M.; Luzon, J.; Etienne, M.; Car, P.-E.; Caneschi, A.; Calvez, G.; Bernot, K.; Sessoli, R. Magnetic Anisotropy in a Dysprosium/DOTA Single-Molecule Magnet: Beyond Simple Magneto-Structural Correlations. *Angew. Chem. Int. Ed.* **2012**, 51, 1606 –1610.
15. Ruamps, R.; Maurice, R.; Batchelor, L.; Boggio-Pasqua, M.; Guillot, R.; Barra, A.-L.; Liu, J.; Bendeif, E.-E.; Pillet, S.; Hill, S.; Mallah, T.; Guihéry, N. Giant Ising-

Type Magnetic Anisotropy in Trigonal Bipyramidal Ni(II) Complexes: Experiment and Theory. *J. Am. Chem. Soc.* **2013**, 135 (8), 3017–3026.

16. Cimpoesu, F.; Ferbinteanu, M., Magnetic Anisotropy in Case Studies. In *Quantum Nanosystems. Structure, Properties, and Interaction*s, Apple Academics, Ontario-New Jersey, Canada-USA, 2014, 524 pp.
17. Christou, G.; Gatteschi, D.; Hendrickson, D. N.; Sessoli, R. Single-molecule magnets. *MRS Bull.* **2000**, 66-71.
18. Gateschi, D.; Sessoli, R. Quantum tunneling of magnetization and related phenomena in molecular materials. *Angew. Chem. Int. Ed.* **2003**, 42(3), 268-297.
19. Gatteschi, D.; Vindigni, A. Single-Chain Magnets. In *Molecular Magnets*, Bartolomé, J.; Luis, F.; Fernández, J.F. Eds.; Publisher: Springer Berlin Heidelberg, Germany, 2014; NanoScience and Technology 2014, pp 191-220.
20. Ferbinteanu, M.; Miyasaka, H.; Wernsdorfer, W.; Nakata, K.; Sugiura, K.; Yamashita, M. Coulon, C.; Clerac, R. Single-Chain Magnet $(NEt_4)[Mn_2(5\text{-}MeOsalen)_2Fe(CN)_6]$ Made of MnIII-FeIII-MnIII Trinuclear Single-Molecule Magnet with an ST= 9/2 Spin Ground State. *J. Am. Chem. Soc.* **2005**, *127*, 3090-3099.
21. Marcos, D.; Martinez-Manez, R.; Folgado, J.-V.; Beltran-Porter, A.; Beltran-Porter, D.; Fuertes, A. Crystal-structure and spectroscopic studies of bis(n-2-pyridinylcarbonyl-2-pyridinecarboximidato)copper(II) monohydrate - local bonding effects. *Inorg. Chim. Acta* **1989**, *159*, 11.
22. Ferbinteanu, M.; Kajiwara, T.; Choi, K.-Y.; Nojiri, H.; Nakamoto, A.; Kojima, N.; Cimpoesu, F.; Fujimura, Y.; Takaishi, S.; Yamashita, M. A Binuclear Fe(III)Dy(III) Single Molecule Magnet. Quantum Effects and Models. *J. Am. Chem. Soc.* **2006**, *128*, 9008−90009.
23. Ferbinteanu, M.; Kajiwara, T.; Cimpoesu , F.; Katagiri, K.; Yamashita, M. The magnetic anisotropy and assembling of the lanthanide coordination units in $[Fe(bpca)_2][Er(NO_3)_3(H_2O)_4]NO_3$, *Polyhedron* **2007**, *26*, 2069-2073.
24. Ferbinteanu, M.; Cimpoesu, F.; Kajiwara, T.; Yamashita, M. Magnetic anisotropy and molecular assembling in complex cation- complex anion type d-f coordination compounds. *Solid State Sci.* **2009**, *11*, 760−765.
25. Ferbinteanu, M. ; Zaharia, A. ; Gîrţu, M. A. ; Cimpoesu, F., Noncovalent effects in the coordination and assembling of the $[Fe(bpca)_2][Er(NO_3)_3(H_2O)_4]\bullet NO_3$ system. *Cent. Eur. J. Chem.* **2010**, *8*(3), 519-529.
26. Ferbinteanu, M.; Cimpoesu, F.; Gîrţu, M.A.; Enachescu, C.; Tanase, S., Structure and Magnetism in Fe–Gd Based Dinuclear and Chain Systems. The Interplay of Weak Exchange Coupling and Zero Field Splitting Effects. *Inorg. Chem.* **2012**, *51*(1), 40–50.
27. Madalan, A.M.; Bernot, K.; Pointillart, F.; Andruh, M.; Caneschi, A. First Ni-II-Ln(III) coordination polymers constructed by using [Ni(bpca)(2)] as a building block [Hbpca = bis(2-pyridylcarbonyl)amine]: Synthesis, crystal structures and magnetic properties. *Eur. J. Inorg. Chem*. **2007**, *35*, 5533-5540.
28. Marcos, D.; Folgado, J.-V.; Beltran-Porter, D.; do Prado-Gambardella, M. T.; Pulcinelli, S. H.; de Almeida-Santos, R. H. Spectroscopic studies and crystal-structure of bis(n-2-pyridinylcarbonyl-2-pyridinecarboximidato) manganese(II) monohydrate - zero-field splitting parameters. *Polyhedron* **1990**, *9*(22), 2699-2704.

29. Wocadlo, S.; Massa, W.; Folgado, J.-V. Synthesis and structural, spectroscopic and magnetic characterization of iron(II) and iron(III) complexes of n-2-pyridinylcarbonyl-2-pyridinecarboximidate. *Inorg. Chim. Acta* **1993**, *207*, 199-206.
30. Kamiyama, A.; Noguchi, T.; Kajiwara, T.; Ito, T. Syntheses, structures, and properties of trinuclear complexes [M(bpca)(2){M '(hfac)(2)}(2)], constructed with the complexed bridging ligand [M(bpca)(2)] [M, M ' = Ni(II), Mn(II); Cu(II), Mn(II); Fe(II), Mn(II); Ni(II), Fe(II); and Fe(II), Fe(II); hbpca = bis(2-pyridylcarbonyl)amine, hhfac = hexafluoroacetylacetone]. *Inorg. Chem.* **2002**, *4*(3), 507-512.
31. Tanaka, H.; Kajiwara, T.; Kaneko, Y.; Takaishi, S.; Yamashita, M. Synthesis, structure, and magnetic property of a new Fe(II)-Fe(III) alternating single-chain magnet constructed with a methyl-substituted bpca(-) ligand. *Polyhedron* **2007**, *26*, 2105-2109.
32. Kooijman, H; Tanase, S.; Bouwman, E.; Reedijk, J.; Spek, A.L. Bis[bis(2-pyridylcarbonyl)aminato]-iron(III) perchlorate acetonitrile disolvate. *Acta Crystallogr., Sect.C: Cryst. Struct. Commun.* **2006**, *62*, m510-m512.
33. Wu D. Bis[N-(2-pyridylcarbonyl)pyridine-2-carboximidato]iron(III) perchlorate methanol solvate. *Acta Crystallogr., Sect. E: Struct. Rep. Online* **2009**, *65*, m1340-u898.
34. Rowland, J.M.; Olmstead, M.M.; Mascharak, P.K. Unusual reactivity of methylene group adjacent to pyridine-2-carboxamido moiety in iron(III) and cobalt(III) complexes. *Inorg.Chem.* **2002**, *41*, 2754-2760.
35. Kajiwara, T.; Sensui, R.; Noguchi, T.; Kamiyama, A.; Ito,T. Syntheses, structures, and magnetic properties of multinuclear complexes constructed with complexed ligands, [M(bpca)(2)](+) (M = Cr(III), Fe(III), Co(III); Hbpca = bis(2-pyridylcarbonyl)amine). *Inorg. Chim. Acta* **2002**, *337*, 299-307.
36. Pandey, R.; Gupta, R.K.; Li, Pei-Zhou; Xu, Qiang; Misra, A.; Pandey, D.S. Photoassisted "Gate-Lock" Fluorescence "Turn-on" in a New Schiff Base and Coordination Ability of E-Z Isomers.*Org. Lett.* **2012**, *14*(2), 592-595.
37. Paul, P.; Tyagi, B.; Bilakhiya, A. K.; Bhadbhade, M. M.; Suresh, E. Stable mononuclear rhodium(II) polypyridyl complexes: synthesis, spectroscopic and structural characterization. *J. Chem. Soc., Dalton Trans.* **1999**, 2009-2014.
38. Paul, P.; Tyagi, B.; Bilakhiya, A. K.; Bhadbhade, M. M.; Suresh, E.; Ramachandraiah, G. Synthesis and characterization of rhodium complexes containing 2,4,6-tris(2-pyridyl)-1,3,5-triazine and its metal-promoted hydrolytic products: Potential uses of the new complexes in electrocatalytic reduction of carbon dioxide. *Inorg. Chem.* **1998**, *37*, 5733-5742.
39. Paul, P.; Tyagi, B.; Bhadbhade, M. M.; Suresh, E. Predominance of electron-withdrawing effect over angular strain in the metal-promoted hydrolysis of 2,4,6-tris(2-pyridyl)-1,3,5-triazine. *J. Chem. Soc., Dalton Trans.* **1997**, 2273-2277.
40. Kajiwara, T.; Ito, T. Mixed-valent heptairon complex with a ground-state spin value of S=12/2 constructed from a triiron cluster ligand. *Angew. Chem., Int. Ed.* **2000**, *39*(1), 230-+.
41. Kamiyama, A.; Noguchi, T.; Kajiwara, T.; Ito, T. A graphite-like complex with large cavities constructed with the complex ligand [Ni-II(bpca)(2)]. *Angew. Chem., Int. Ed.* **2000**, *39*(17), 3130-3132.

42. Kajiwara, T.; Ito, T. Complexed bridging ligand, [M(bpca)(2)] (M = Mn(II) or Fe(II); Hbpca = bis(2-pyridylcarbonyl)amine), as a building block for linear trinuclear complexes. *J. Chem. Soc., Dalton Trans.* **1998**, 3351-3352.
43. Kajiwara, T.; Nakano, M.; Kaneko, Y.; Takaishi, S.; Ito, T.; Yamashita, M.; Igashira-Kamiyama, A.; Nojiri, H.; Ono, Y.; Kojima, N. A single-chain magnet formed by a twisted arrangement of ions with easy-plane magnetic anisotropy. *J. Am. Chem. Soc.* **2005**, *127*(29), 10150-10151.
44. Kaneko, Y.;Kajiwara, T.; Yamane, H.; Yamashita, M. Solvent induced reversible change of magnetic properties in a Fe(II)-Fe(III) single chain magnet. *Polyhedron* **2007**, *26*, 2074-2078.
45. Kamiyama, A.; Noguchi, T.; Kajiwara, T.; Ito, T. Controlling the construction of trinuclear, 1-D, and 2-D Ni(II)Fe(II)/Fe(II)Fe(II) complexes: selective syntheses, structures, and magnetic properties. *Cryst. Eng. Comm.* **2003**, *5*, 231-237.
46. Kajiwara, T.; Tanaka, H.; Nakano, M.; Takaishi, S.; Nakazawa, Y.;Yamashita, M. Single-Chain Magnets Constructed by Using the Strict Orthogonality of Easy-Planes: Use of Structural Flexibility to Control the Magnetic Properties. *Inorg. Chem.* **2010**, *49*(18), 8358-8370.
47. Kajiwara, T.; Watanabe, I.; Kaneko, Y.; Takaishi, S.; Enomoto, M.; Kojima, N.; Yamashita, M. Direct observation of the ground-spin alignment of Fe(II)-Fe(III) single-chain magnet by muon-spin relaxation. *J. Am. Chem. Soc.*, **2007**, *129*(41), 12360–12361.
48. SMART, SAINT and XPREP, Area detector control and data integration and reduction software, Bruker Analytical X-ray Instruments Inc., Madison, WI, 1995.
49. G.M. Sheldrick, SADABS: Program for Empirical Absorption Correction of Area Detector Data, University of Göttingen, Göttingen, Germany, 1996.
50. G.M. Sheldrick, SHELX-97: Programs for Crystal Structure Analysis, University of Göttingen, Göttingen, Germany, 1998.
51. Fisher, M. E. Magnetism in One-Dimensional Systems-The Heisenberg Model for Infinite Spin. *Am. J. Phys.* **1964**, *32*, 343-346.
52. Christian, P.; Rajaraman, G.; Harrison, A.; McDouall, J. J.W.; Raftery, J. T.; Winpenny R. E. P. Structural, magnetic and DFT studies of a hydroxide-bridged {Cr-8} wheel. *Dalton Trans*. **2004**, *10*, 1511-1512.

NEW FRONT. CHEM. (**2014**)
Volume 23, Number 1, pp. 53-60
ISSN 2393-2171; ISSN-L 2393-2171

Former: Ann. West Univ. Timisoara – Series Chem.
ISSN: 1224-9513

Article

HYBRID SILICA-PORPHYRIN NANOMATERIALS SENSITIVE TO GAS DETECTION

Anca Palade[(1)], Ionela Creanga[(1)], Anca Lascu[(1)], Catalin Ianasi[(1)], Birdeanu Mihaela[(1,2)], Eugenia Fagadar-Cosma[(1)(♣)]

[(1)] Institute of Chemistry –Timisoara of Romanian Academy, 24 M. Viteazul Ave., 300223-Timisoara, Romania.
[(2)] National Institute for Research and Development in Electrochemistry and Condensed Matter, 1 Plautius Andronescu Street, 300224 Timisoara, Romania.

Abstract

Meso-tetratolylporphyrin encapsulated in a silica matrix leads to a porous hybrid nanomaterial that was tested to CO_2 detection. For experimental purposes, the material was solved in THF and a continuous flow of CO_2 gas was introduced to the solution. The response of the material to gas adding was measured using UV-Vis spectra and colorimetric changes. The dependence of the absorption intensity of the Soret band and the CO_2 concentration is linear with a fair correlation coefficient of 0.92 but the establishment of equilibrium for the reversible CO_2 indicator has to be improved.

Keywords: *meso*-tetratolylporphyrin, hybrid silica materials, UV-Vis, AFM, CO_2 detection

1. INTRODUCTION

Due to the well-known amazing photosensitive properties of natural and synthetic porphyrins and because of their high reactivity, researchers have tried to enhance these exceptional qualities by combining different porphyrins with various metal colloids, polymers or silica precursors to obtain various nanomaterials [1,2].

The demand for safe environmental conditions led to the development in gas sensor approaches and technology. Metal-organic frameworks (MOFs) combined with porphyrin nanoassemblies have great potential in gas storage, gas separations, catalysis, and sensing [3].

♣ Correspondent author: efagadar@yahoo.com

Thus, immobilized complexes of Pd-porphyrin in clay minerals are exceptionally suitable and economically affordable to be used as efficient optical oxygen sensors [4].

A sensitive structure consisting of 5,10,15,20-tetrakis(3,4dimethoxy-phenyl)-porphyrin Fe(III) chloride and single walls carbon nanotubes (SWCN) included in a Ba stearate matrix was used for the development of a sensor by depositing the nanomaterial on a ceramic substrate with platinum interdigital electrodes. The sensor proved a strong sensibility to UV irradiation [5]. Tests performed upon this material also showed that the manufactured sensor presents good sensitivity toward O_2 ionization [6].

Other inorganic scaffolds used for this purpose were: SWCN in combination with iron(III) protoporphyrin IX, applied on a graphite electrode that was used as reduction agent for H_2O_2 [7].

Hybrid materials obtained from the encapsulation of 5,10,15,20-tetratolyl-21H,23H-porphyrin in silica matrices have been previously prepared [8] and their morphological properties were characterized. Beside the content of porphyrin dye, the use of this kind of mesoporous material as potential gas detector (CO_2 in this case) is justified by the high surface area and large pore volume. The material was obtained by in situ two steps acid–base catalyzed sol–gel method, starting from TEOS.

The present study is based on pH dye-based indicators, in which the gas carbon dioxide dissolves in aqueous solution to form carbonic acid; the acid can dissociate to generate protons, which react with the porphyrin indicator producing a color change due to the obtainment of mono- and di-protonated porphyrin species.

2. EXPERIMENTAL METHOD

Apparatus

The spectrometer used for recording UV spectra was a UV-vis JASCO V-650 apparatus. Cuvettes were 1 cm quarz glass. Measurements were done in the range of interest 350-750 nm.

Atomic force microscopic surface imaging was performed on Nanosurf[l] EasyScan 2 Advanced Research apparatus from samples deposited on silica plates. Measurement conditions were environmental, using contact or tapping mode. The investigated scan areas were maximum 9 µm x9 µm, with lateral resolution of 20 nm and vertical resolution of 2 nm.

QUANTACHROME Nova 1200 apparatus was used for the determination of pore size, by using nitrogen as adsorbate, at the temperature of liquid nitrogen 77.350K. The method for calculation was de Boer's (programme Quantachrome NovaWin2 - Data Acquisition and Reduction for NOVA instruments ©1994-2003, Quantachrome Instruments, version 2.1). Thermogravimetric analysis was performed with a Paulik & Erdey D type derivatograph. The measurements were conducted in air using a platinum crucible. The heating rates were 5K/min.

Hybrid synthesis

The hybrid material was obtained and has been fully characterized as previously reported [8] and the silica glass obtained by in two steps acid-base catalysis was used for the experiments, due to its corresponding pH characteristics.

Testing of CO_2 sensitivity

Porphyrin –silica hybrid material (1 g) solved in 30 mL THF and 5 mL H_2O was sealed in a 50 mL Erlenmeyer flask equipped with a magnetic stirrer. Through the cork a syringe needle was introduced to the bottom of the flask and CO_2 gas was bubbled (1mL/min) under intense stirring. The cork was envisioned with a supplementary needle through which the samples were extracted, without affecting the gas flow through the solution and the equilibrium reactions. Samples were extracted every 15 minutes or by exact time monitoring and were characterized by UV-vis spectra (Figure 3).

3. RESULTS AND DISCUSSIONS

Amorphous inorganic solids that contain immobilized porphyrins can be obtained by sol–gel processes at environmental temperatures. These hybrids usually retain the optical properties of the encapsulated organic compound. The structure and properties of the nanomaterials can be easily designed by controlling the preparation conditions.

In case of silica, using one step acid catalysis transparent gels of low porosity are obtained, whereas with basic catalysts gels of higher porosity are made [9].

Using tetraethyl-orthosilicate (TEOS) as precursor, silica gels were obtained by hydrolysis and condensation reactions in EtOH/water solutions at room temperature. For the first hydrolysis step hydrochloric acid was used as catalyst. In the second condensation step ammonia was used as catalyst. It is well-known that the molar ratio between water and tetraethylorthosilicate as well as the pH of the gelation point significantly influences the properties of the obtained material [8].

Hybrid materials obtained from the encapsulation of 5,10,15,20-tetratolyl-21H,23H-porphyrin (Figure 1) in TEOS-based silica matrices were tested for potential CO_2 gas detection. The calculation by de Boer method for the hybrid material used in the experiments reveals the cumulative pore volume of 0.14 cm^3/g and a large surface a surface area of 326.6 m^2/g. The pore size are in the range of 1.377-2.60 nm.

The UV-vis spectrum of the bare 5,10,15,20-tetratolyl-21H,23H-porphyrin in THF is *etio*-type. The Soret band, of the highest energy, is located at 417 nm and has been assigned to the $S_0 \rightarrow S_2$ transition while the four lower energy bands, namely Q-bands, have been assigned to the $S_0 \rightarrow S_1$ transition [8]. The spectrum of the hybrid material solved in the same solvent presents the same shape but the lower intensities of the Q bands because of the interactions of the porphyrin molecules with the silica matrix (Figure 3).

By increasing the CO2 concentration in the solution, the registered spectra of the hybrid samples show a constant increase of the Soret band intensity. The decrease in the number of Q bands is attributed to the increase of the acidity in the tested porphyrin-silica solution.

As can be seen in Figure 4, the dependence of the absorption intensity of the Soret band and the CO_2 increased volume is linear. The correlation coefficient of 0.919 represents a promising response of the material to the presence of the gas. We have to mention that the reversibility time takes too long and will be further improved.

Figure 1: The structure of the 5,10,15,20-tetratolyl-21H,23H-porphyrin used to obtain the hybrid silica material

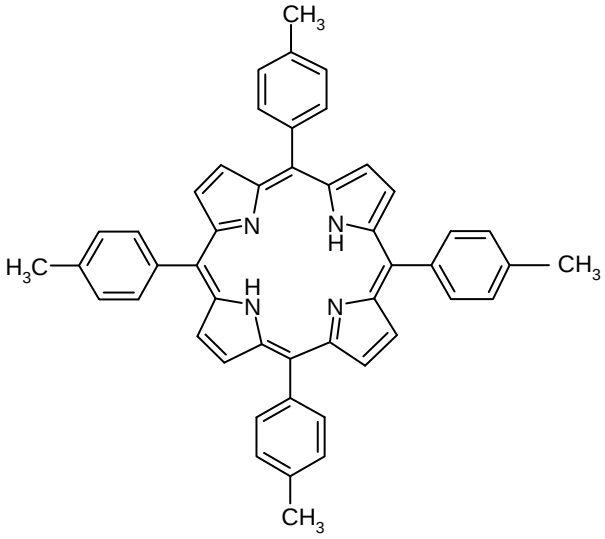

Figure 2: The UV-vis spectrum of the hybrid material solved in THF

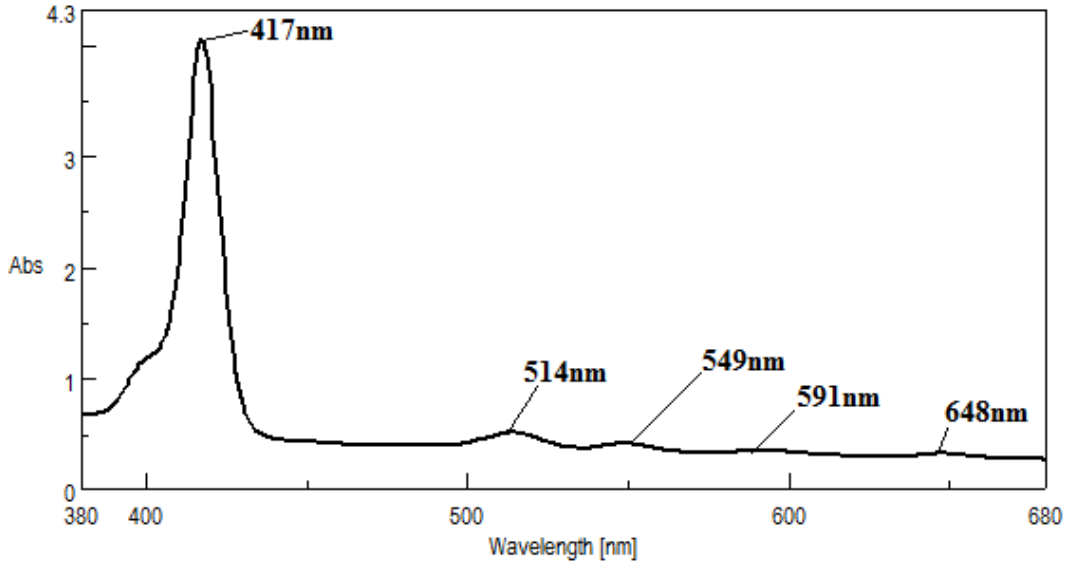

Figure 3: The superposed UV-vis spectra of the THF-water solution of the hybrid material at increasing CO_2 concentration

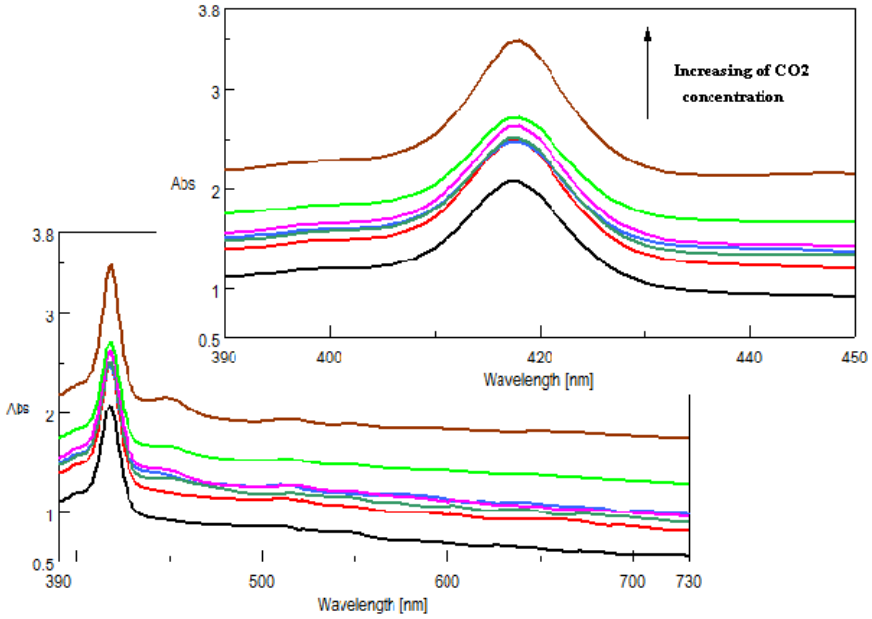

Figure 4: The correlation coefficient between the absorption intensity and the CO_2 gas volume

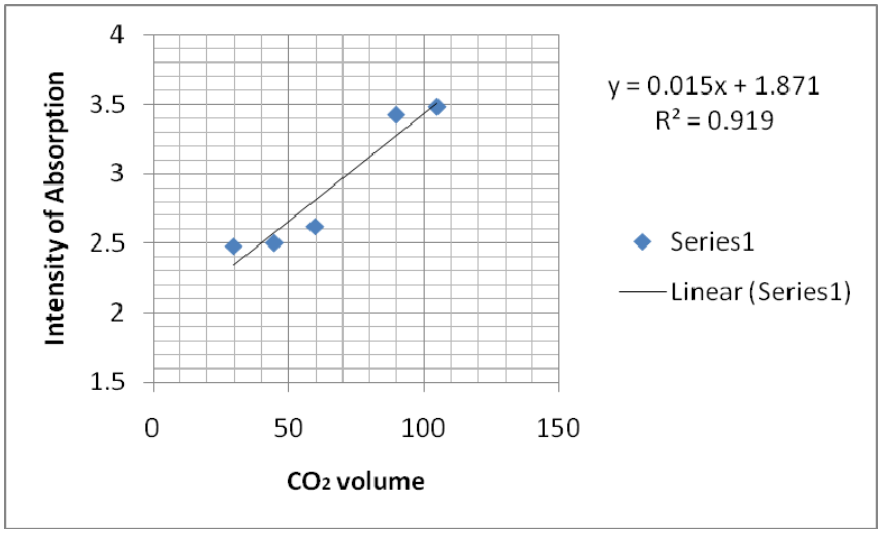

The color of porphyrins suffer changes during the experiments as response to different pH media and this is also a useful tool in detecting of carbonic acid in the solution. This change of color was evidenced by taking snapshots of the solution at the various stages of gas introduction (Figure 5).

Figure 5: The color changes during the gassing process **1**: the hybrid material before the introduction of CO_2 gas; **2-5**: the hybrid material at various stages of constant CO_2 flow

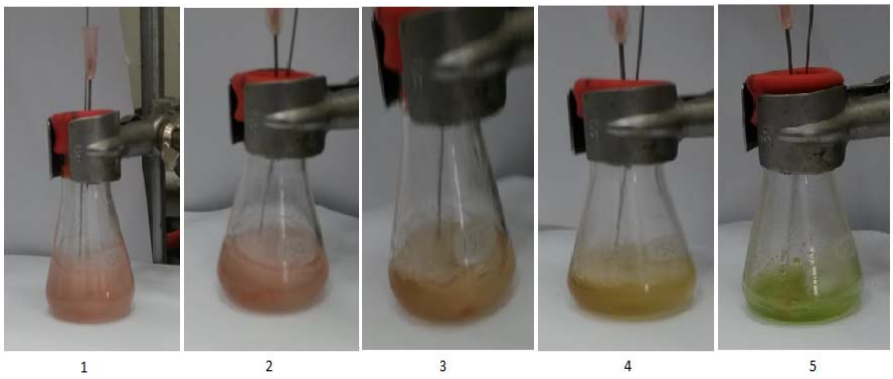

The AFM images performed on the hybrid material solved in THF and deposited by drop casting on silica plates are presented in Figure 6 a and b. It can be observed that the porphyrin molecules have a tendency to aggregate in triangular platelets, consistent with their already reported behaviour [8]. These aggregates are evenly oriented and of the same sizes.

Figure 6: 2D AFM images of the hybrid material solved in THF and deposited by drop casting

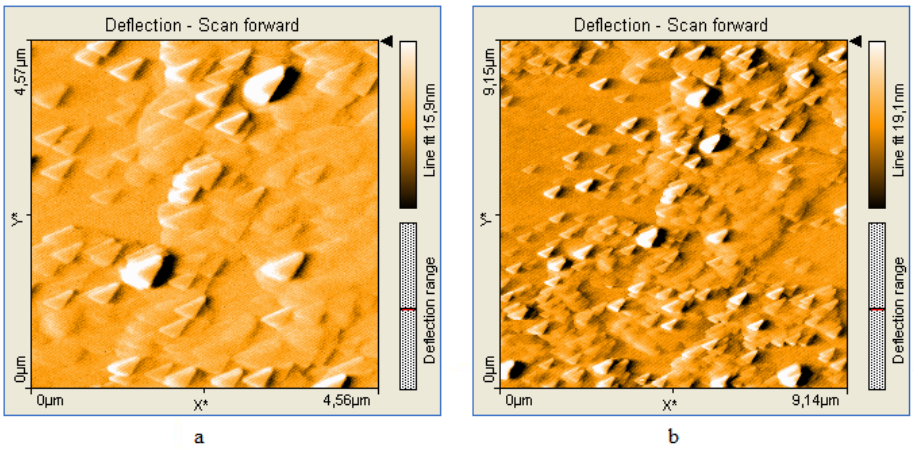

The 3D AFM image presented in Figure 7 outlines the formation of superposed triangular structures, corresponding to sandwich H-type aggregates, with dimensions ranging in the 370-480 nm domain.

Figure 7: 3D AFM image of the hybrid material

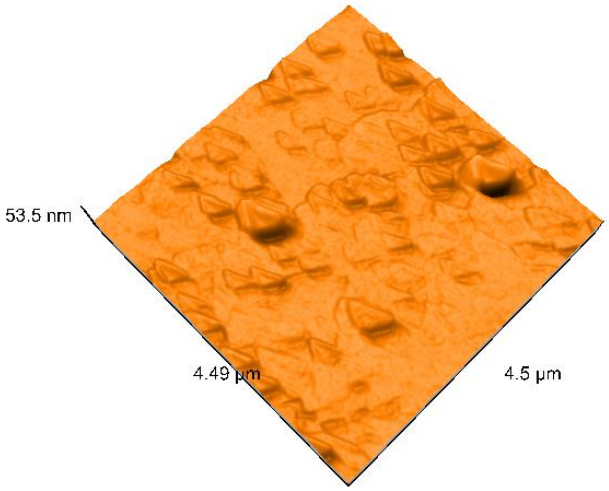

Particle analysis offer information about the mean surface of islands, that is 0.0206 μm^2. The particles have a mean height of 0.8 nm, but the highest peak is arround 40 nm. The mean rugosity is of 3.9 nm.

According to thermal analysis the hybrid is stable to thermal treatment at least up to 350 °C (Figure 8). High thermal stability is the main requirement in porous materials that can be used in the fabrication of potential gas sensor devices.

Figure 8: Thermal analysis of the hybrid material after intensivelly drying

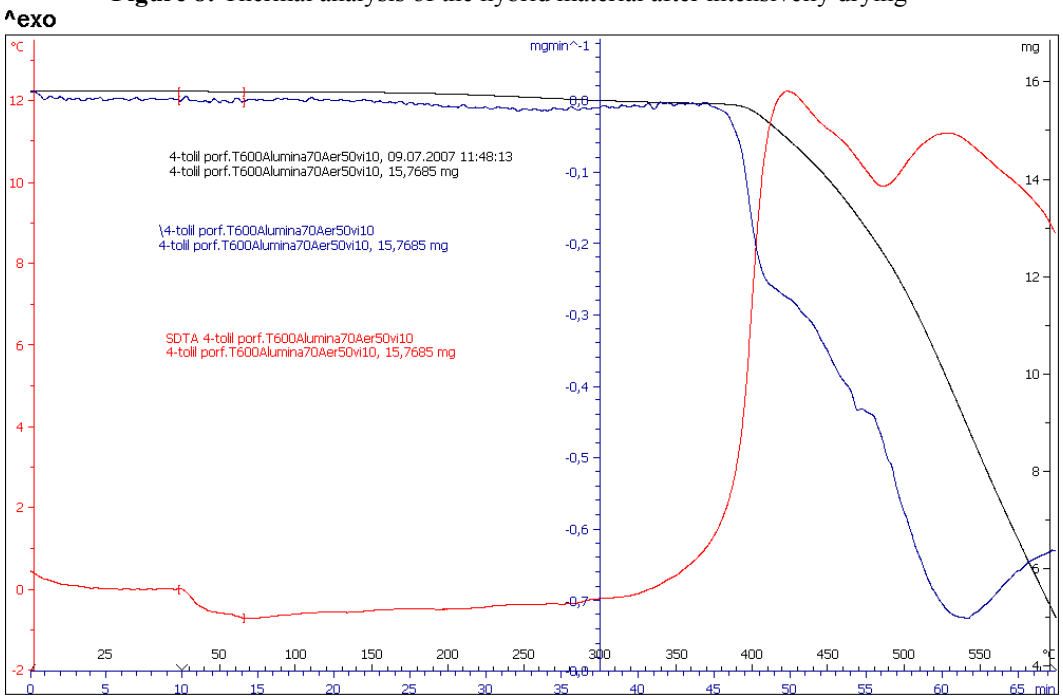

4. CONCLUSIONS

Hybrid silica-porphyrin materials, obtained from TEOS by in situ two steps acid–base catalyzed sol–gel method, show a great potential toward the sensing of gases due to large pore volume and surface area of the microporous material and also because its high thermal stability. The optical properties of such materials essentially maintain those of the organic dye chosen to be incorporated in the anorganic matrix. The 5,10,15,20-tetratolyl-21H,23H-porphyrin –silica hybrid is suited for optical/colorimetric formulation for CO_2 sensors if the time for reversible process will be improved. The dependence of the absorption intensity of the Soret band and the CO_2 concentration is linear with a fair correlation coefficient of 0.92.

ACKNOWLEDGEMENTS

The authors wish to thank the Chemistry Institute of Timisoara of the Romanian Academy, Programme 3 and to SAFEAIR Project No. 76/2013 for its material support.

REFERENCES

1. Fagadar-Cosma E.; Dudás Z.; Birdeanu M.; Almásy L.Hybrid organic – silica nanomaterials based on novel A_3B mixed substituted porphyrin. *Mat. Chem. Phys*, http://dx.doi.org/10.1016/j.matchemphys.2014.07.023
2. Taranu B.O.; Fagadar-Cosma E.; Popa I.; Plesu N.; Taranu I.Adsorbed functionalized porphyrins on polyaniline modified platinum electrodes. Comparative electrochemical properties. *Dig. J. Nanomat. Bios*. **2014,** *9(2*), 667 – 679.
3. John R. P.; *Metal-Organic Frameworks and Porphyrin Nanomaterials for Hydroge*n *Storage, Gas Separations, and Catalysis*, Northwestern University, 2011; 209 pages; 3469764
4. Ceklovsky A.; Takagi S. Hybrid Clay /Porphyrin Nanomaterials for Oxygen Sensing. Proceedings Of The International Conference Nanomaterials: Applications And Properties 2013; Vol. 2; No 1, 01PCSI16(2pp)
5. Baschir L.; Fagadar-Cosma E.; Creanga I.; Palade A.; Lascu A.; Birdeanu M.; Savastru D.; Savu V.; Antohe S.; Velea A.; Fagadar-Cosma G.; Popescu M.; Simandan I.D. UV Sensing Effect In Langmuir-Blodgett Complex Films Containing A Novel Synthesized Fe(III) Porphyrin. *Dig. J. Nanomat. Bios*., **2014**, *9(2)*, 847-857
6. Baschir L. Metalloporphyrin with photo-electrical behavior based on Fe(III) porphyrin. *Optoelectron Adv Mat* – Rapid Commun., **2014**, *8(1-2)*, 23 – 25
7. Ju H.; Zhang X.; Wang J.; *Nanobiosensing, Principles, Development and Application*, Springer New York, ISSN:1618-7210, pp. 113-129
8. Fagadar-Cosma E.; Enache C.; Armeanu I.; Dascalu D.; Fagadar-Cosma G.; Vasile M.; Grozescu I. The influence of pH over topography and spectroscopic properties of silica hybrid materials embedding meso-tetratolylporphyrin. *Mat. Res. Bull.*, **2009**, *44*, 426–431
9. Kamitani K.; Uo M.; Inoue H.; Makishima A. Synthesis and spectroscopy of tpps-doped silica gels by the sol-gel process. *J.Sol–GelSci.Technol*. **1993**, *1,* 85–92.

NEW FRONT. CHEM. (**2014**)
Volume 23, Number 1, pp. 61-72
ISSN 2393-2171; ISSN-L 2393-2171

Former: Ann. West Univ. Timisoara – Series Chem.
ISSN: 1224-9513

Article

ADVANCED QSAR AND COMPUTATIONAL MUTAGENESIS APPLIED TO MITOTIC CHECKPOINT PROTEIN HMAD1 MUTANTS WITH IMPLICATION IN GENETIC DISORDERS

Speranta Avram[1,♣], Adina Milac[1,2], Catalin Buiu[3] and Livia-Cristina Borcan[4]

[1] University of Bucharest, Faculty of Biology, Department of Anatomy, Animal Physiology and Biophysics, 91-95th Independentei Str., Bucharest-076201, Romania
[2] Institute of Biochemistry of the Romanian Academy, Structural Biochemistry and Bioinformatics Department, 296th Independentei Str., Bucharest-060031, Romania
[3] Politehnica University of Bucharest, Faculty of Automatic Control and Computers, 113th Independentei Str., Bucharest-040042, Romania
[4] Municipal Clinical Emergency Hospital of Timisoara, Occupational Health Dept., 12th Revolutiei 1989 Bvld., Timisoara-300041, Romania

ABSTRACT

In normal cells, the accuracy of chromosome segregation namely euploidy is ensured by properly functioning error-checking spindle assembly checkpoint. Spindle assembly checkpoint component, human mitotic arrest-deficient protein Mad1 (hMad1) is critical to prevent cellular aneuploidy, and was recognized as an inductor of genetic diseases. Here, we analyzed the capacity of hMad1 mutants in their risk of inducing genetic disorders. Their critical molecular descriptors were calculated and compared by structure–activity relationships in order to elucidate the contribution of these molecular features to initiate genetic disorders. Our results suggest that in the hMad1 mutants descriptors could be deeply involved in aneuploidy.

Keywords: Mad1, cancer, bipolar syndrome, computational mutagenesis.

♣ Correspondent author: Tel: 0040740234158, Fax: 0040213181573, E-mails: speranta.avram@gmail.com

1. INTRODUCTION

During mitotic cell division, exact copies of cell chromosomes are obtained and pairs of sister chromatids are produced [1,2]. Furthermore, these are attached to microtubules originating from two opposite spindle poles by kinetochores (protein structure on chromatids) during a bi-orientation process [1,3,4]. A judicious bi-orientation mechanism leads to euploidy, but, sometimes, the premature separation of a single pair of sister chromatids may lead to aneuploidy [4]. Therefore, the cells develop a control system called the mitotic spindle assemble checkpoint (SAC), which delays the onset of anaphase until all sister chromatid pairs have performed the bi-orientation process [5-7].

The SAC complex is formed by many proteins including Bub1, BubR1, Bub3, Mps1, Mad1 and Mad2, which are recruited to unattached kinetochores to prevent aneuploidy [5]. The functional mechanism of SAC involves interactions among these proteins; Mad1-Mad2 core complex represents the key catalytic engine of the SAC [8]. It is important to mention that the Mad1-Mad2 core complex catalyses the conformational activation of the unusual two-state protein Mad2 [9-16].

Biochemically, the hMad1 amino acid sequence is 718 residues long and is highly conserved from yeast to human. Crystallographic studies [5,17,18] revealed that: (i) hMad1 is an elongated protein, which works as a dimer; (ii) residues 485-584 are critical for Mad1-Mad2 binding and stabilisation of the Mad1 dimer, therefore; (iii) mutations in this region destabilise the Mad1–Mad2 complex and the Mad1-Mad1 dimer. Structure-based mutagenesis and clinical studies [18-21] showed that mutations in the Mad1-Mad2 binding motif, 500-580 amino acids, critically affect SAC activity, and represent a major form of genomic instability in human cancers [19-21] or bipolar disorder (BD) [22]. A recent study by Cichon *et al.* [22] demonstrated a significant genome-wide association between hMad1 on 7p22.3 and an excess of T alleles in patients with BD. The same genetic variation of hMad1 on 7p22.3 was also found in patients with cancer [20,22], where the following hMad1 mutants were identified: R59C, T500M and R556C. Nomoto *et al.* [19] and Tsukasaki *et al.* [20] identified hMad1 mutations R59C, T299A, T500M, E511K, E516K, R556C, E569K and R572H as being involved in the pathogenesis of a variety of human cancers, including lymphomas, lung, prostate and breast cancers, and glioblastomas.

Despite numerous *in vivo* and *in vitro* studies connecting aneuploidy with hMad1 mutations, its complex structural and functional profile hindered a complete understanding of aneuploidy mechanisms. Encouraged by the large amount of clinical and experimental data, and also considering the reduced number of computational and crystallographic studies, we aimed to use structure–activity relationship (SAR) analysis to rationalise the capacity of established hMad1 mutants to induce aneuploidy and design new aneuploidy-inducing mutants by computational mutagenesis.

All SAR methods consider that macroscopic properties are induced by molecular structure, and every change in molecular structure leads to modification of these properties [23]. Considering that hMad1 is widely involved in many types of genetic diseases, the design and analysis of new hMad1 mutants appears to be a necessity in preclinical and clinical studies. However, prediction accuracy of protein function is dependent on the appropriate selection of physical and chemical properties of proteins. Usually, the selection of

effective molecular descriptors is problem-dependent and there is no universal rule to achieve this goal.

We previously developed SAR models [24,25] for viral proteins and antimicrobial activity of peptides, and proposed new, more effective analogues, which suggest that molecular descriptors, including hydrophobic features, steric (e.g., molecular surface area) or count of atom types, are critical for biological activity.

In the present study, we attempt to generate highly accurate SAR models of cellular proteins by using computational methods, and to explore new perspectives for understanding the mechanism of aneuploidy and its implication in genetic diseases. Thus, we establish variations in molecular descriptors, such as electronic fields and protein surface areas, which described hMad1 wild type (wt) and other mutant forms, and we calculate the values of these descriptors in cases of aneuploidy.

2. METHODS

2.1. Dataset for analysis: molecular modeling minimum energy calculation strategy of classical and *de novo* hMAD1 mutants

Based on experimental data demonstrating that hMad1 residues 493-584 are critical for Mad1-Mad2 interactions, we generated hMad1 mutants from a hMad1 wt template available from crystallographic structures (PDB: 1GO4) [5,18]. The database of hMad1 mutants was generated according to the following criteria: (i) the range of observed destabilisation of hMad1 function, and also the variability of cellular lines expressing these mutants [5,19,20]; and (ii) the variety of amino acids that were replaced in the hMad1 structure. In agreement with experimental data [20,21], we chose to analyse aneuploidy induced by eight hMad1 mutants that are deeply involved in promoting many types of cancers, and probably BD: T500M (numerous cancer types and possibly BD), E511K (lung cancer), E516K (numerous cancer types), R556C (prostate cancer and probably BD), R556H (lung cancer), R558H (numerous cancer types), E569K (breast cancer), and R572H (numerous cancer types). Furthermore, in our study, we included hMad1 C568D, L571D, L575D, P549A, M545A, and L543A mutants, which completely abolished or significantly reduced Mad1-Mad2 binding [18].

An important objective of the study was to determine the molecular features of *de novo* hMad1 mutants susceptible to induce aneuploidy. *De novo* hMad1 mutants were designed following several general rules: (i) the electrostatic contacts were changed by introducing positively charged amino acids: for example, R, K and H; (ii) the number of hydrophobic contacts was varied by introducing very hydrophobic amino acids F, I and W; (iii) we changed the hydrogen bond donor/acceptor character by introducing R and K; and (iv) the molecular surface areas were changed by substitutions with small amino acids, such as A or G, or the bulky amino acid W. The mutations were: T500/S/N/L/W; E511/R/D/N/Q; E516/T/M/F/L; R556/K/L/F/I; R558/A/W/M/G; E569/D/Q/P/W; and R572/K/L/F/I, and we aimed to analyses whether the replacements of these amino acids were able, or not, to induce

aneuploidy by changing the values of molecular descriptors in comparison with hMad1 mutants template.

Molecular modeling of all dimer hMad1 mutants was performed using Insight software package (Accelrys, Inc., San Diego, CA, USA) and the minimum potential energy was calculated using conjugate gradient method, Kollman force-field [26]. After energy minimisation, Kollman partial charges [27] of the compounds were loaded. During energy minimisation, free movement of only the amino acid side chains was allowed.

2.2. Descriptors Calculation

Molecular descriptors of hMad1 wt and mutants were calculated using a database from MOE software (Chemical Computing Group, Montreal, PQ, Canada). The following considerations were critical for our study: solvation energy [28-30], and surface areas represented by: (i) subdivided van der Waals surface induced by hydrophobic and polar atoms (vsa_hyd, vsa_pol) [31,32]; (ii) subdivided solvent accessible surface areas induced by hydrophobic and polar atoms (ASA_hyd, ASA_pol) [31,32]; and (iii) subdivided solvent accessible surface areas induced by atoms with positive and, respectively, negative partial charges (ASA_pos, ASA_neg) [31,32].

3. RESULTS AND DISCUSSIONS

3.1. Results

The initial stage of our study results was represented by the evaluation of molecular descriptors described as hMad1 mutants already recognised as aneuploidy risk factors. Table 1 illustrates the molecular descriptors, showing significant fluctuations among hMad1 wt and mutant forms in the domain of residues 493-579.

Table 1: Molecular descriptors of Mad1 wt, Mad1 mutants recognized as aneupoidy inductors and *de novo* Mad 1 mutants obtained by computational mutagenesis

	Mad1 mutants	**E_sol (kcal/mol)**	**ASA_hyd ($Å^2$)**	**ASA_pol ($Å^2$)**	**vsa_pol ($Å^2$)**	**vsa_hyd ($Å^2$)**
Literature-based Mad1 mutants	Mad1 wt	-3440.56	8038.16	8096.00	6407.53	9148.24
	T500M	-3425.01	8117.24	8127.62	6380.40	9241.98
	E511K	-3381.12	8016.23	8149.42	6388.75	9220.46
	E516K	-3772.79	8078.25	8127.11	6388.75	9220.46
	R556C	-3451.54	8130.51	7887.33	6306.41	9152.19
	R556H	-3447.66	8202.24	7874.16	6329.14	9202.24
	R558H	-3332.45	8113.44	8036.75	6347.93	9130.02
	E569K	-3339.45	8230.46	8028.22	6388.75	9220.46
	R572H	-3297.43	8117.45	7946.56	6347.93	9130.02

	C568D	-3666.90	7985.85	8154.24	6461.80	9144.29
	L571D	-3711.79	7984.28	8191.37	6461.80	9026.19
	L575D	-3638.83	7930.12	8201.30	6461.80	9026.19
	P549A	-3421.79	7981.65	8106.42	6418.90	9103.22
	M545A	-3440.23	7949.46	8028.85	6407.53	9037.58
	L543A	-3442.74	7984.72	8112.76	6407.53	9053.39
Mad1 mutants obtained by computational mutagenesis	T500S	-3445.56	8001.18	8131.80	6407.53	9116.62
	T500N	-3451.80	7936.60	8211.96	6443.02	9104.12
	T500L	-3422.44	8137.09	8051.45	6380.40	9226.17
	T500W	-3432.09	8179.84	8088.32	6391.76	9293.42
	E511R	-3463.14	8008.27	8137.66	6435.60	9188.84
	E511D	-3500.77	8010.21	8126.05	6407.53	9116.62
	E511N	-3333.94	8004.45	8129.04	6415.88	9116.62
	E511Q	-3332.58	8039.37	8112.29	6415.88	9148.24
	E516T	-3468.94	8078.86	8063.83	6380.40	9160.74
	E516M	-3436.26	8082.69	8047.83	6353.26	9254.48
	E516F	-3448.75	8160.88	7970.12	6353.26	9279.12
	E516L	-3457.11	8122.52	8012.13	6353.26	9238.67
	R556K	-3436.89	8140.18	7966.52	6360.68	9179.86
	R556L	-3419.87	8210.59	7823.62	6325.20	9198.07
	R556F	-3433.85	8291.84	7796.59	6325.20	9238.53
	R556I	-3421.07	8171.81	7827.23	6325.20	9198.07
	R558A	-3303.95	8093.54	7983.20	6325.20	9103.22
	R558W	-3311.90	8283.18	7957.10	6336.56	9265.32
	R558M	-3305.30	8164.38	8033.89	6325.20	9213.88
	R558G	-3303.43	8054.63	8003.68	6325.20	9071.61
	E569D	-3530.94	7983.52	8110.04	6407.53	9116.62
	E569Q	-3436.41	8013.90	8171.54	6415.88	9148.24
	E569P	-3422.37	8059.33	8009.68	6341.90	9188.84
	E569W	-3427.01	8193.79	7976.28	6364.63	9305.92
	R572K	-3481.57	8091.42	8051.23	6360.68	9179.86
	R572L	-3396.79	8151.87	7908.00	6325.20	9198.07
	R572F	-3400.69	8222.90	7871.26	6325.20	9238.53
	R572I	-3395.02	8140.85	7903.32	6325.20	9198.07

Different variations of molecular descriptors, such as subdivided van der Waals surface areas, were recorded in hMad1 wt and mutants in the domain of residues 493-579. To better emphasize the variation of different parameters for various mutants, and due to the fact that the absolute numeric values of descriptors are high, we plotted the difference between subdivided molecular surface area values calculated for hMad1 mutants and wt in Figure 1 and 2. Figure 1 demonstrates that the presence of hydrophobic residues induces a significant fluctuation of van der Waals surface areas (vsa_hyd) compared with a weak fluctuation of the van der Waals surface areas induced by polar (vsa_pol) amino acid residues. In addition,

Figure 2 shows that the presence of hydrophobic, polar and charged atoms induces fluctuation of solvent accessible surface area.

Figure 1: Dot-plot representation of the van der Waals area components given by hydrophobic and polar atoms (values are calculated as the difference between various mutants and wild type Mad1; black diamonds correspond to mutations: T500M, E511K, E516K, R556C, R556H, R558H, E569K, and R572H; grey diamonds correspond mutations: C568D, L571D, L575D, P549A, M545A, and L543A; open diamonds correspond to computationally induced mutations)

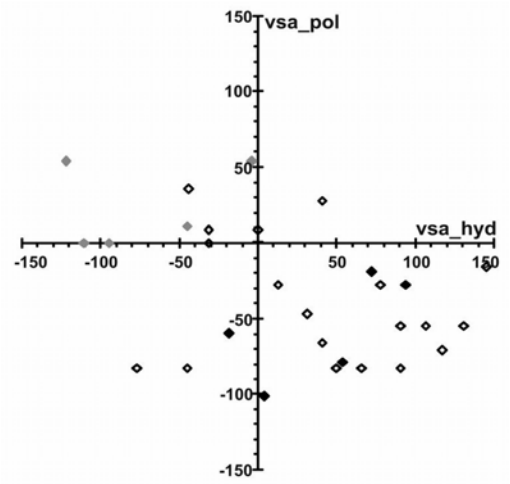

Figure 2: Dot-plot representation of the solvent accessible surface area components corresponding to the polar and hydrophobic atoms (values are calculated as the difference between various mutants and wild type Mad1; black diamonds correspond to mutations: T500M, E511K, E516K, R556C, R556H, R558H, E569K, and R572H; grey diamonds correspond to mutations: C568D, L571D, L575D, P549A, M545A, and L543A; open diamonds correspond to computationally induced mutations)

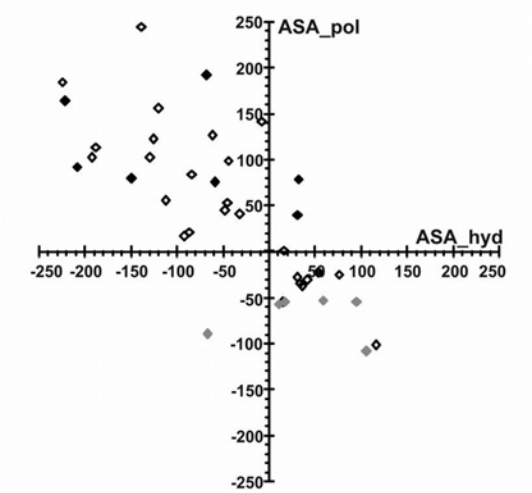

3.2. Discussion

Based on the SAR hypothesis, stating that molecular descriptors of proteins are able to suggest their function, we performed a study comparing molecular descriptors, identified as critical, in native and mutants hMad1 in the domain of residues 493-579, which is strongly involved in Mad1-Mad2 binding and already recognized as a cellular euploidy factor. Furthermore, to provide a new interpretation of aneuploidy mechanism, based on molecular descriptors evaluation, we induced, by computational mutagenesis, a number of hMad1 mutants and analyzed these mutants as possible aneuploidy inductors.

In our study, we classified and analyzed the molecular descriptors in a few clusters: (i) the potential energy cluster including solvation, van der Waals, electrostatic and torsion energies; (ii) the molecular surface cluster containing subdivided van der Waals and solvent accessible surface areas; and (iii) the structural cluster comprising molecular descriptors derived directly from protein sequence atoms (polar/hydrophobic/hydrogen bond donor–acceptor) and bond type (rigid and rotatable) counts.

Molecular descriptors of hMad1 mutants in the domain of residues 493-579, especially potential energy descriptors, undergo significant variation with solvation energy changing from -3772.79 kcal/mol (E516K) to -3297.43 kcal/mol (R572H), and torsion energy changing from 952.15 kcal/mol (T500L) to 972.96 kcal/mol (R558M).

Cluster analysis of solvation energy indicates that hMad1 wt and the hMad1 mutant M545A have almost identical values (-3440.56 kcal/mol vs. -3440.23 kcal/mol). Other very similar values of solvation energy were obtained for four *de novo* mutants: L543A (-3442.74 kcal/mol), R556K (-3436.89 kcal/mol), E569Q (-3436.41 kcal/mol) and E516M (-3436.26 kcal/mol; Table 1). We may presume that, in this respect, these hMad1 mutants, induced by computational mutagenesis, have a small risk to induce cellular aneuploidy.

A similar interpretation may be given to the substitution of smaller-sized positively charged amino acid R572 with non-polar amino acids L, F and I, and the bulky positive amino acid K. A comparison between the values of solvation energy of hMad1 wt and these hMad1 mutants (see Table 1), suggests that these mutants have a low chance of inducing various types of cancer. This observation is supported by: (i) experimental data [19,20] showing that hMad1 R572H induces many types of cancer; and (ii) findings that the solvation energy values for mutants R572/L/F/I/K are closer to hMad1 wt than to the pathological hMad1 R572H mutant (Table 1). On the other hand, the solvation energy value of hMad1 wt is significantly different from that of the naturally occurring hMad1 R572H mutant (-3297.43 kcal/mol) and those of *de novo* mutants: R558G (-3303.43 kcal/mol), R558M (-3305.30 kcal/mol) and R558A (-3303.95 kcal/mol). Based on the experimental data mentioned above and on our computational results, it can be stated that, energetically, the above-mentioned *de novo* hMad1 mutants may induce the same cancer types as the R572H mutant.

In Figure 3, we represent the solvation energy variation of mutants at several positions (indicated on the bottom line) towards the value for the wt hMad1. The position of these residues on the protein structure is illustrated in the top panel.

Figure 3: Variation of the solvation energy between various Mad1 mutants and the wild type protein (different mutations at the same position in the wild type protein (shown on the bottom line) are indicated by the same background shade; the specific target mutation is indicated by letters near each column; the top image indicates the position of each mutated residue in the Mad1 structure (PDB: 1GO4); for simplicity, only those mutants whose descriptors demonstrated variations above 4% are shown)

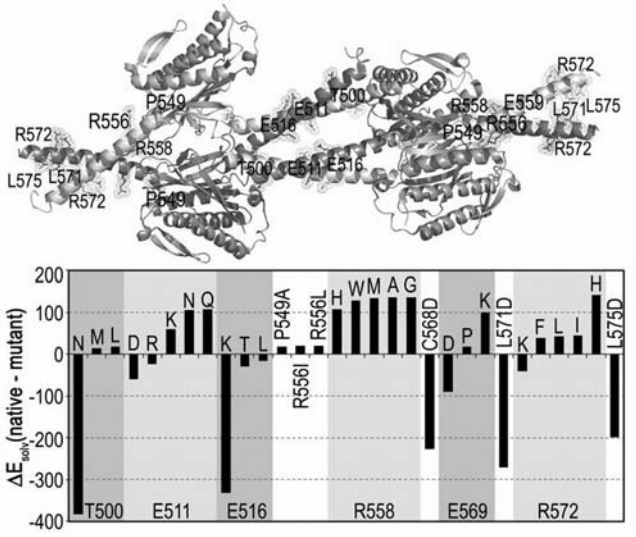

For hMad1 mutants, the analysis of subdivided van der Waals descriptors cluster (Figure 4) indicates that: (i) a vsa_hyd varies significantly in the range between 9026.19 $Å^2$ (L575D) and 9305.92 $Å^2$ (E569W); and (ii) a relatively small variation was found for vsa_pol (from 6306.41 $Å^2$ (R556C) to 6461.80 $Å^2$ (C568D)).

In Figure 4, we presented the difference between values of vsa_hyd area for the hMad1 wt and its various mutants. Mutations inducing large variations of descriptor values have a higher probability of inducing pathologies such as cancer or BD.

Figure 4: Variation of the hydrophobic component of the van der Waals surface area between various Mad1 mutants and the wild type protein (different mutations at the same position in the wild type protein (shown on the bottom line) are indicated by the same background shade)

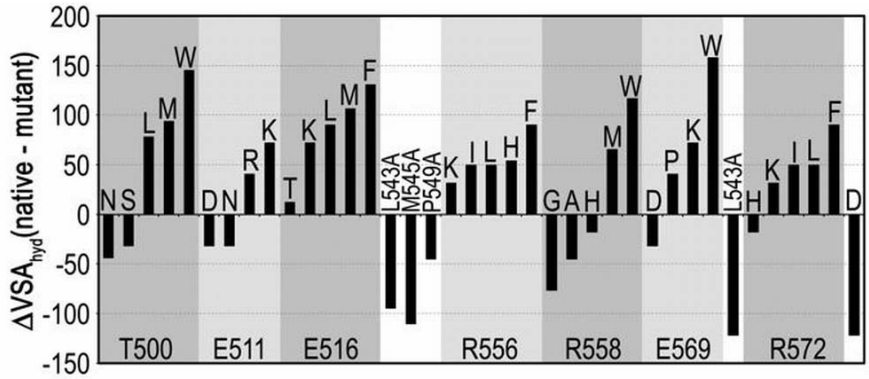

The specific target mutation is indicated by letters near each column. For simplicity, only those mutants whose descriptors demonstrated variations above 4% are shown.

In our study, the value of vsa_hyd area for hMad1 wt was 9148.24 $Å^2$ and the value of vsa_pol area for hMad1 wt was 6407.13 $Å^2$. Our results suggest that, sterically, *de novo* hMad1 mutants E511Q (9148.24 $Å^2$) and E569Q (9148.24 $Å^2$) are less likely to induce aneuploidy. Within the same series of Mad1 mutants, when arginine, threonine and glutamic acid were replaced with bulky hydrophobic tryptophan, phenylalanine or methionine, vsa_hyd values varied within the range of 9250-9300 $Å^2$: E516M (9254.48 $Å^2$), R558W (9265.32 $Å^2$), E516F (9279.12 $Å^2$), T500W (9293.42 $Å^2$), and E569W (9305.92 $Å^2$). We suggest that these *de novo* mutants may induce various types of cancer or BD, given the similarity between their vsa_hyd area values with those of the hMad1 T500M mutant (9241.98 $Å^2$) and the clinical data proving that the hMad1 T500M mutant induces various types of cancer or BD (20, 21, 24, 25).

Analysis of the subdivided solvent accessible surface area variations showed the following fluctuations: ASA_pol maximum and minimum values of 8211.96 $Å^2$ (T500N) and 7796.59 $Å^2$ (R556F), respectively, and ASA_hyd maximum and minimum values of 8291.84 $Å^2$ (R556F) and 7930.12 $Å^2$, respectively. Cluster analysis of solvent accessible surface areas demonstrated very similar ASA_pol values between hMad1 wt (8096.00 $Å^2$) and the *de novo* mutant T500W (8088.32 $Å^2$), suggesting that this mutation is sterically less likely to induce aneuploidy. On the contrary, other *de novo* mutants, such as R556L (7823.62 $Å^2$) and R556I (7827.23 $Å^2$), have very similar ASA_pol values with R556H (7874.16 $Å^2$) and R556C (7887.33 $Å^2$). In conjunction with experimental data showing that hMad1 R556C and R556H induced prostate and lung cancer, and probably psychiatric disorders [19,20], our computational data support the hypothesis that hMad1 R556L and R556I mutants induce the same pathologies.

When subdivided solvent accessible surface area are considered as an aneuploidy factor, we presume that various *de novo* hMad1 mutants may fail to induce different types of cancer when they have the following molecular features: (i) ASA_hyd around values of hMad1 wt (8038.16 $Å^2$, e.g., E511Q (8039.37 $Å^2$)); (ii) ASA_pol around values of hMad1 wt (8096.00 $Å^2$, e.g., T500W (8088.32 $Å^2$)); or (iii) solvent accessible surface areas induced by atoms with a positive partial charge around values of hMad1 wt (11367.97 $Å^2$, e.g., R556K (11365.23 $Å^2$); Table 1 and Figure 1, 2 and 4).

We have to mention that the lack of experimental data regarding *de novo* hMad1 mutants imposes significant limitations on the impact of our study. Even though the biological processes in which hMad1 are involved are very complex and difficult to replicate *in vivo*, the extension of our study by *in vivo* analyses of these *de novo* mutants is crucial.

4. CONCLUSIONS

Molecular simulation techniques such as rational design of protein mutants and structural – enzymatic activity relations will continue to reveal important information about protein function or implication of proteins in many cellular processes such as correct chromosome segregation (euploidy), but it is important to understand the limitations and problems of these

techniques. In our study a number of Mad1 mutants (already known to induce aneuploidy and proposed by us by computational mutagenesis), at distinct domain: 493-579 (strongly involved into Mad1-Mad2 binding already recognized to affect cellular euploidy) were considered.

These mutants were analyzed relatively to structural descriptors in correlation with destabilization of SAC activity and also inducing genetic diseases like cancer and BD. Among various structural descriptors considered in our study, the steric (van der Waals area and solvent accessible area and their subdivided) and also energetic solvation energy descriptor are more relevant for our ability to predict genetic pathologies and their mechanism of action, for the development of effective methods for early diagnosis and for possible treatment strategies. We concluded that the evaluation of solvation energy of the Mad1 amino acids and also, in equal manner the van der Waals and the solvent accessible surface areas over all hydrophobic/polar and positively charged atoms may be important for predicting by molecular simulation techniques the aneuploidy inductor role of Mad1 mutants. We suggested that the Mad1 wild-type and mutants molecular descriptors evaluated here represent important resources for future computational studies focused on aneuploidy, provided kinetic data about Mad1-Mad2 and/or Mad1-Bub3 are available.

ACKNOWLEDGEMENT

Funding: Speranta Avram acknowledges support from the Romanian National Authority for Scientific Research grant CNMP PNII 89/2012, grant PNII-PCCA-16/2012 and PC7 ERA-NET HIVERA.

REFERENCES

1. Yu, H. Structural activation of Mad2 in the mitotic spindle checkpoint: the two-state Mad2 model versus the Mad2 template model. *J Cell Biol* **2006**, *173*, 153–157.
2. Koshland, D.E.; Guacci, V. Sister chromatid cohesion: the beginning of a long and beautiful relationship. *Curr Opin Cell Biol* **2000**, *12*, 297–301.
3. Cleveland, D.W.; Mao, Y.; Sullivan, K.F. Centromeres and kinetochores: from epigenetics to mitotic checkpoint signaling. *Cell* **2003**, *112*, 407–421.
4. Tanaka, K.; Mukae, N.; Dewar, H.; van Breugel, M.; James, E.K.; Prescott, A.R.; Antony, C.; Tanaka, T.U. Molecular mechanisms of kinetochore capture by spindle microtubules. *Nature* **2005**, *434*, 987–994.
5. Kim, S.; Sun, H.; Tomchick, D.R.; Yu, H.; Luo, X. Structure of human Mad1 C-terminal domain reveals its involvement in kinetochore targeting. *Proc Natl Acad Sci USA* **2012**, *109*, 6549–6554.
6. Musacchio, A.; Salmon, E.D. The spindle-assembly checkpoint in space and time. *Nat Rev Mol Cell Biol* **2007**, *8*, 379–393.
7. Musacchio, A.; Ciliberto, A. The spindle-assembly checkpoint and the beauty of self-destruction. *Nat Struct Mol Biol* **2012**, *19*, 1059–1061.
8. Schuyler, S.C.; Wu, Y.F.; Kuan, V.J. The Mad1-Mad2 balancing act – a damaged spindle checkpoint in chromosome instability and cancer. *J Cell Sci* **2012**, *125*, 4197–4206.

9. Luo, X.; Tang, Z.; Xia, G.; Wassmann, K.; Matsumoto, T.; Rizo, J.; Yu, H. The Mad2 spindle checkpoint protein has two distinct natively folded states. *Nat Struct Mol Biol* **2004**, *4*, 338–345.
10. Mapelli, M.; Massimiliano, L.; Santaguida, S.; Musacchio, A. The Mad2 conformational dimer: structure and implications for the spindle assembly checkpoint. *Cell* **2007**, *4*, 730–743.
11. Mapelli, M.; Filipp, F.V.; Rancati, G.; Massimiliano, L.; Nezi, L.; Stier, G.; Hagan, R.S.; Confalonieri, S.; Piatti, S.; Sattler, M.; Musacchio, A. Determinants of conformational dimerization of Mad2 and its inhibition by p31com. *EMBO J* **2006**, *6*, 1273–1284.
12. Izawa, D.; Pines, J. Mad2 and the APC/C compete for the same site on Cdc20 to ensure proper chromosome segregation. *J Cell Biol* **2012**, *1*, 27–37.
13. Kulukian, A.; Han, J.S.; Cleveland, D.W. Unattached kinetochores catalyze production of an anaphase inhibitor that requires a Mad2 template to prime Cdc20 for BubR1 binding. *Dev Cell* **2009**, *1*, 105–117.
14. Tischer, T.; Hörmanseder, E.; Mayer, T.U. The APC/C inhibitor XErp1/Emi2 is essential for *Xenopus* early embryonic divisions. *Science* **2012**, *6106*, 520–524.
15. Jia, L.; Li, B.; Warrington, R.T.; Hao, X.; Wang, S.; Yu, H. Defining pathways of spindle checkpoint silencing: functional redundancy between Cdc20 ubiquitination and p31(comet). *Mol Biol Cell* **2011**, *22*, 4227–4235.
16. Kim, S.; Yu, H. Mutual regulation between the spindle checkpoint and APC/C. *Semin Cell Dev Biol* **2011**, *6*, 551–558.
17. De Antoni, A.; Pearson, C.G.; Cimini, D.; Canman, J.C.; Sala, V.; Nezi, L.; Mapelli, M.; Sironi, L.; Faretta, M.; Salmon, E.D.; Musacchio, A. The Mad1/Mad2 complex as a template for Mad2 activation in the spindle assembly checkpoint. *Curr Biol* **2005**, *3*, 214–225.
18. Sironi, L., Mapelli, M., Knapp, S., De Antoni, A., Jeang, K.T., Musacchio, A. Crystal structure of the tetrameric Mad1–Mad2 core complex: implications of a 'safety belt' binding mechanism for the spindle checkpoint. *EMBO J* **2002**, *10*, 2496–2506.
19. Nomoto, S.; Haruki, N.; Takahashi, T.; Masuda, A.; Koshikawa, T.; Takahashi, T.; Fujii, Y.; Osada, H.; Takahashi, T. Search for *in vivo* somatic mutations in the mitotic checkpoint gene, *hMAD1*, in human lung cancers. *Oncogene* **1999**, *50*, 7180–7183.
20. Tsukasaki, K.; Miller, C.W.; Greenspun, E.; Eshaghian, S.; Kawabata, H.; Fujimoto, T.; Tomonaga, M.; Sawyers, C.; Said, J.W.; Koeffler, H.P. Mutations in the mitotic check point gene, *MAD1L1*, in human cancers. *Oncogene* **2001**, *25*, 3301–3305.
21. Cahill, D.P., da Costa, L.T.; Carson-Walter, E.B.; Kinzler, K.W.; Vogelstein, B.; Lengauer, C. Characterization of *MAD2B* and other mitotic spindle checkpoint genes. *Genomics* **1999**, *2*, 181–187.
22. Cichon, S.; Mühleisen, T.W.; Degenhardt, F.A.; Mattheisen, M.; Miró, X.; Strohmaier, J.; Steffens, M.; Meesters, C.; Herms, S.; Weingarten, M.; Priebe, L.; Haenisch, B.; Alexander, M.; Vollmer, J.; Breuer, R.; Schmäl, C.; Tessmann, P.; Moebus, S.; Wichmann, H.E.; Schreiber, S.; Müller-Myhsok, B.; Lucae, S.; Jamain, S.; Leboyer, M.; Bellivier, F.; Etain, B.; Henry, C.; Kahn, J.P.; Heath, S.; Bipolar Disorder Genome Study (BiGS) Consortium; Hamshere, M.; O'Donovan, M.C.; Owen, M.J.; Craddock, N.; Schwarz, M.; Vedder, H.; Kammerer-Ciernioch, J.; Reif, A.; Sasse, J.; Bauer, M.; Hautzinger, M.; Wright, A.; Mitchell, P.B.; Schofield, P.R.; Montgomery, G.W.; Medland, S.E.; Gordon, S.D.; Martin, N.G.; Gustafsson, O.; Andreassen, O.; Djurovic, S.; Sigurdsson, E.; Steinberg, S.; Stefansson, H.;

Stefansson, K.; Kapur-Pojskic, L.; Oruc, L.; Rivas, F.; Mayoral, F.; Chuchalin, A.; Babadjanova, G.; Tiganov, A.S.; Pantelejeva, G.; Abramova, L.I.; Grigoroiu-Serbanescu, M.; Diaconu, C.C.; Czerski, P.M.; Hauser, J.; Zimmer, A.; Lathrop, M.; Schulze, T.G.; Wienker, T.F.; Schumacher, J.; Maier, W.; Propping, P.; Rietschel, M.; Nöthen, M.M. Genome-wide association study identifies genetic variation in neurocan as a susceptibility factor for bipolar disorder, *Am. J. Hum. Genet.* **2011**, *3*, 372–381.

23. Akamatsu, M. Current state and perspectives of 3D-QSAR. *Curr Top Med Chem* **2002**, *12*, 1381–1394.
24. Avram, S.; Duda-Seiman, D.; Borcan, F.; Radu, B.; Duda-Seiman, C.; Mihailescu, D. Evaluation of antimicrobial activity of new mastoparan derivatives using QSAR and computational mutagenesis. *Int J Pept Res Ther* **2011**, *17*, 7–17.
25. Avram, S.; Mihailescu, D.F.; Borcan, F.; Milac, A.L. Prediction of improved antimicrobial mastoparan derivatives by 3D-QSARCoMSIA/CoMFA and computational mutagenesis. *Monatsh Chem* **2012**, *143*, 535–543.
26. Gellért, A.; Salánki, K.; Náray-Szabó, G.; Balázs, E. Homology modelling and protein structure based functional analysis of five cucumovirus coat proteins. *J Mol Graph Model* **2006**, *5*, 319–327.
27. Henriques, J.; Costa, P.J.; Calhorda, M.J.; Machuqueiro, M. Charge parametrization of the DvH-c3 heme group: validation using constant-(pH,E) molecular dynamics simulations. *J Phys Chem B* **2013**, *1*, 70–82.
28. Talavera, D.; Robertson, D.L.; Lovell, S.C. Characterization of protein–protein interaction interfaces from a single species, *PLoS One* **2011**, *6*, e21053.
29. Eisenberg, D.; McLachlan, A.D. Solvation energy in protein folding and binding. *Nature* **1986**, *319*, 199–203.
30. Pei, J.; Wang, Q.; Zhou, J.; Lai, L. Estimating protein–ligand binding free energy: atomic solvation parameters for partition coefficient and solvation free energy calculation. *Proteins* **2004**, *4*, 651–664.
31. Li, A.J.; Nussinov, R. A set of van der Waals and coulombic radii of protein atoms for molecular and solvent-accessible surface calculation, packing evaluation, and docking. *Proteins* **1998**, *1*, 111–127.
32. Bhat, S.; Purisima, E.O. Molecular surface generation using a variable-radius solvent probe. *Proteins* **2006**, *1*, 244–261.

NEW FRONT. CHEM. (**2014**)
Volume 23, Number 1, pp. 73-77
ISSN 2393-2171; ISSN-L 2393-2171

Former: Ann. West Univ. Timisoara – Series Chem.
ISSN: 1224-9513

Article

TWO TYPES OF CONNECTIVITY INDICES OF THE LINEAR PARALLELOGRAM BENZENOID

Mohammad Reza Farahani ♣
Department of Applied Mathematics, Iran University of Science and Technology (IUST)
Narmak, Tehran, Iran

ABSTRACT

A molecular graph is constructed by representing each atom of a molecule by a vertex and bonds between atoms by edges. The degree of each vertex equals the valence of the corresponding atom. In this paper, we focus on the structure of an infinite family of the linear parallelogram benzenoid P(n,m) ($\forall m,n\in\mathbb{N}-\{1\}$) and compute two types of Connectivity indices of it.

Keywords: Molecular graph, Benzenoid graph, Randic Connectivity Index, Sum-Connectivity Index

1. INTRODUCTION

Let *G=(V;E)* be a simple connected molecular graph with vertex set *V=V(G)* and edge set *E=E(G)*. A molecular graph is constructed by representing each atom of a molecule by a vertex and bonds between atoms by edges. The degree of each vertex equals the valence of the corresponding atom. A general reference for the notation in graph theory is [1].

In graph theory, we have many different topological index of arbitrary graph *G*. A topological index is a numeric quantity from the structural graph of a molecule. Usage of topological indices in chemistry began in 1947 when chemist *Harold Wiener* developed the most widely known topological descriptor, the Wiener index, and used it to determine physical properties of types of alkanes known as paraffin [2-7].

$$W(G)=\sum_{e=uv\in E(G)} d(u,v)$$

♣ Correspondent author: E-mails: Mr_Farahani@Mathdep.iust.ac.ir & MrFarahani88@gmail.com

The distance *d(u,v)* between the vertices *u* and *v* of the graph G is equal to the length of (number of edges in) the shortest path that connects *u* and *v*.

The first connectivity index introduced in 1975 by *M. Randic* [8-12] has shown this index to reflect molecular branching. The Randić connectivity index (Randić branching index) $\chi(G)$ is defined as

$$\chi(G)=\sum_{e=uv\in E(G)}\frac{1}{\sqrt{d_u d_v}}$$

where for any edge in the summation term, d_u and d_v stand for degrees of adjacent vertices joined by that edge.

In 2008, a closely related variant of Randić connectivity index called the Sum-connectivity index was introduced by *Zhou* and *Trinajstić* [13-14]. The Sum-connectivity index $X(G)$ is defined as

$$X(G)=\sum_{e=uv\in E(G)}\frac{1}{\sqrt{d_u+d_v}}$$

where d_u and d_v are the degrees of the vertices *u* and *v*, respectively.

In recent years, some researchers are interested to topological indices of benzenoid molecular graph. Throughout this paper *P(n,m)* denotes of an infinite class of the linear parallelogram *P(n,m)* of benzenoid graph in terms of the number of hexagons (benzene C_6) in the first row *n* and the number of hexagons in the first column *m*, see [15-21] and Figure 1 for details.

2. MAIN RESULTS

In this section, we focus on the structure of an infinite family of the linear parallelogram benzenoid graph P(n,m) ($\forall m,n\in\mathbb{N}-\{1\}$) , Figure 1 and compute its connectivity indices.

Theorem 1. $\forall m,n\in\mathbb{N}-\{1\}$, consider the linear parallelogram benzenoid graph P(n,m). Then the Randic Connectivity index $\chi(P(n,m))$ and the Sum-Connectivity index X(P(n,m)) are equal to

$$\chi(P(n,m))=mn+\frac{2}{3}(\sqrt{6}-1)(m+n)+3$$

and

$$X(P(n,m))=\frac{1}{2}\sqrt{6}\,mn+\left(\frac{12\sqrt{5}-5\sqrt{6}}{15}\right)(m+n)+\frac{5\sqrt{6}-16\sqrt{5}}{10}+2$$

To achieve our aims we need to the following definition.

Definition 1. Let G be the molecular graph and d_v is degree of vertex $v\in V(G)$. We divide edge set *E(G)* and vertex set *V(G)* of graph G to several partitions, as follow:

$\forall k: \delta\le k\le\Delta,\ V_k=\{v\in V(G)|\ d_v=k\}$
$\forall i: 2\delta\le j\le 2\Delta,\ E_i=\{e=uv\in E(G)|d_u+d_v=i\}$
$\forall j: \delta^2\le j\le\Delta^2,\ E_j^*=\{uv\in E(G)|d_u\times d_v=j\}$.

where δ and Δ are the minimum and maximum, respectively, of d_v for all $v \in V(G)$, obviously $1 \le \delta \le d_v \le \Delta \le n-1$.

Figure 1: A 2-D graph of of linear polycene parallelogram benzenoid graph $P(a,b)$ [18]

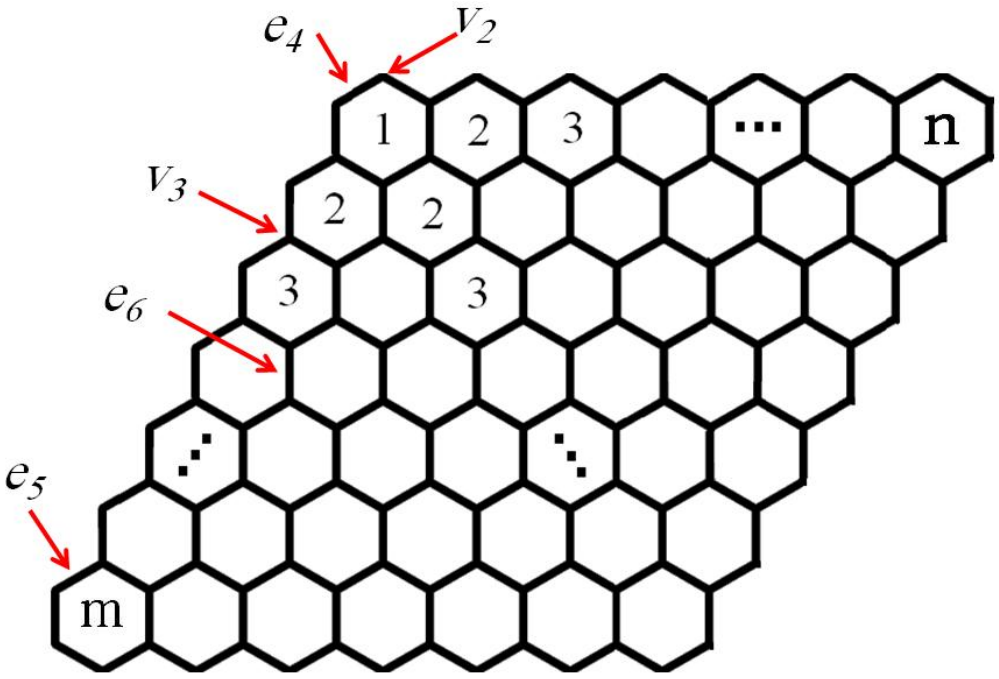

Proof. Let G be the linear parallelogram P(n,m), with |V(P(n,m))|=2mn+2m+2n vertices and |E(P(n,m))|=3mn+2n+2m-1 edges ($\forall m,n \in \mathbb{N}-\{1\}$) depicted in Figure 1 and references [15-21].

From the structure of the linear parallelogram benzenoid graph $P(n,m)$, one can see that there are two partitions V_2 and V_3 with their size as follow:

$V_2=\{v \in V(P(n,m))|\ d_v=2\} \rightarrow |V_2|=2(m+n+1)$

$V_3=\{v \in V(P(n,m))|\ d_v=3\} \rightarrow |V_3|=2mn-2$

By according to Definition 1,

$E_4=\{e=uv \in E(P(n,m))|\ d_u=d_v=2\} \rightarrow |E_4|=|E_4^*|=4$

$E_5=\{e=uv \in E(P(n,m))|\ d_u=3\ \&d_v=2\} \rightarrow |E_5|=|E_6^*|=2|E_4|=4(m+n-2)$

$E_6=\{e=uv \in E(P(n,m))|\ d_u=d_v=3\} \rightarrow |E_6|=|E_9^*|=3mn-2n-2m+3$

Thus, we have following computations for the Randic Connectivity and Sum-Connectivity indices of the linear parallelogram benzenoid graph $P(n,m)$ as follows:

$$\chi(P(n,m)) = \sum_{uv \in E(P(n,m))} (d_v d_v)^{(-1/2)}$$

$$= \sum_{uv \in E_9^*} \frac{1}{\sqrt{d_v d_v}} + \sum_{uv \in E_6^*} \frac{1}{\sqrt{d_v d_v}} + \sum_{uv \in E_4^*} \frac{1}{\sqrt{d_v d_v}}$$

$$= \frac{|E_9^*|}{\sqrt{9}} + \frac{|E_6^*|}{\sqrt{6}} + \frac{|E_4^*|}{\sqrt{4}}$$
$$= \frac{1}{3} \times (3mn - 2n - 2m + 3) + \frac{\sqrt{6}}{6} \times 4(m + n - 2) + \frac{1}{2} \times 4$$
$$= mn + \frac{2}{3}(\sqrt{6} - 1)(m + n) + 3$$

and

$$X(P(n,m)) = \sum_{uv \in E(P(n,m))} (d_v + d_v)^{(-1/2)}$$
$$= \sum_{uv \in E_4} \frac{1}{\sqrt{d_v + d_v}} + \sum_{uv \in E_5} \frac{1}{\sqrt{d_v + d_v}} + \sum_{uv \in E_6} \frac{1}{\sqrt{d_v + d_v}}$$
$$= \frac{|E_4|}{\sqrt{4}} + \frac{|E_5|}{\sqrt{5}} + \frac{|E_6|}{\sqrt{6}}$$
$$= \frac{1}{2} \times 4 + \frac{\sqrt{5}}{5} \times 4(m + n - 2) + \frac{\sqrt{6}}{6} \times (3mn - 2n - 2m + 3)$$
$$= \frac{1}{2}\sqrt{6}\, mn + \left(\frac{12\sqrt{5} - 5\sqrt{6}}{15}\right)(m + n) + \frac{5\sqrt{6} - 16\sqrt{5}}{10} + 2$$

Here, we complete the proof of the Theorem 1.

4. CONCLUSION

The main goal of chemistry and technology of benzenoid graph is synthesis of molecules having defined properties. The use of topological and connectivity indices as structural descriptors is important in molecular graph and Nano-structure. In this paper, we compute two types of Connectivity indices of an infinite family of the linear parallelogram benzenoid.

REFERENCES

1. West, D.B. *An Introduction to Graph Theory*. Prentice-Hall, 1996.
2. Wiener, H. Structural Determination of Paraffin Boiling Points. *J. Am. Chem. Soc.* **1947**, *69*, 17.
3. Needham, D.E.; Wei, I.C.; P.G. Seybold. Molecular modeling of the physical properties of alkanes. *J. Am. Chem. Soc.* **1988**, *110*, 4186.
4. Rucker, G.; Rucker, C. On topological indices, boiling points, and cycloalkanes. *J. Chem. Inf. Comput. Sci.* **1999**, *39*, 788.
5. Todeschini, R.; Consonni, V. *Handbook of Molecular Descriptors*; Wiley, Weinheim, 2000.
6. Dobrynin, A.A.; Entringer, R.; Gutman, I. Wiener index of trees: Theory and applications. *Acta Appl. Math*. **2001**, *66*, 211–249.

7. Zhou, B.; Gutman, I. Relations between Wiener, Hyper-Wiener and Zagreb Indices. *Chemical Physics Letters.* **2004**, *394*, 93-95.
8. Randic, M. On the characterization of molecular branching. *J. Amer. Chem. Soc.* **1975**, *97*, 6609-6615.
9. Klarner, D.A. Polyominoes. In *Handbook of Discrete and Computational Geometry;* J. E. Goodman, J. O'Rourke, (eds.); CRC Press, Boca Raton., 1997, Chapter 12, 225-242.
10. Trinajstić, N. *Chemical Graph Theory*; CRC Press, Bo ca Raton, FL, 1992.
11. Yu, P. An upper bound on the Randic of tree, *Journal of Mathematical. Study (Chinese).* **1998**, *31*, 225.
12. Ghorbani, M.; Ghazi, M. Computing Some Topological Indices of Triangular Benzenoid. *Digest J. Nanomater. Bios.* **2010**, *5(4)*, 1107-1111.
13. Zhou, B.; N. Trinajstić, On a novel connectivity index. *J. Math. Chem.* **2009**, *46*, 1252-1270.
14. Zhou, B.; Trinajstić, N. On general sum-connectivity index. *J. Math. Chem.* **2010**, *47*, 210-218.
15. Khadikar, P.V. Padmakar-Ivan Index in Nanotechnology. *Iranian Journal of Mathematical Chemistry* **2010***, 1(1),* 7−42.
16. Alaeiyan, M.; Mojarad, R.; Asadpour, J. A new method for computing eccentric connectivity polynomial of an infinite family of linear polycene parallelogram benzenod. *Optoelectron. Adv. Mater.-Rapid Commun.* **2011**, *5(7),* 761-763.
17. Alaeiyan, M.; Asadpour, J. Computing the MEC polynomial of an infinite family of the linear parallelogram *P(n,n). Optoelectron. Adv. Mater.-Rapid Commun.* **2012**, *6(1-2),* 191–193.
18. Farahani, M.R. Computing a Counting polynomial of an infinite family of linear polycene parallelogram benzenoid graph *P(a,b). Journal of Advances in Physics* **2013**, *3(1)*, 186-190.
19. Farahani, M.R. On Sadhana polynomial of the linear parallelogram *P(n,m)* of benzenoid graph. *Journal of Chemica Acta* **2013**, *2(2)*, 95-97.
20. Farahani, M.R. Computing the Omega polynomial of an infinite family of the linear parallelogram *P(n,m). Journal of Advances in Chemistry* **2013**, *1*, 106-109.
21. Farahani, M.R. Connective Eccentric Index of Linear Parallelogram *P(n,m). Int. Letters of Chemistry, Physics and Astronomy* **2014**, *18*, 57-62.